GEDIZ UNIVERSITY ★ GRADUATE SCHOOL OF SCIENCE ENGINEERING AND TECHNOLOGY

CHARACTERIZATION AND ANTIMICROBIAL PROPERTIES OF MULTIPLE LAYER SILK FIBROIN/HYALURONIC ACID FILM ON CoCrMo ALLOY

M.Sc. THESIS

Pınar ARPAÇAY

Institute of Science

Nanotechnology Graduate Program

Thesis Advisor: Assist. Prof. Dr. Uğur TÜRKAN

OCTOBER 2013

GEDIZ UNIVERSITY ★ GRADUATE SCHOOL OF SCIENCE ENGINEERING AND TECHNOLOGY

CHARACTERIZATION AND ANTIMICROBIAL PROPERTIES OF MULTIPLE LAYER SILK FIBROIN/HYALURONIC ACID FILM ON CoCrMo ALLOY

M.Sc. THESIS

Pınar ARPAÇAY
(60071106)

Institute of Science

Nanotechnology Graduate Program

Thesis Advisor: Assist. Prof. Dr. Uğur TÜRKAN

OCTOBER 2013

GEDİZ ÜNİVERSİTESİ ★ FEN BİLİMLERİ ENSTİTÜSÜ

CoCrMo ALAŞIMINDA ÇOKLU TABAKALI İPEK FİBROİN/HYALURONİK ASİT FİLMİNİN KARAKTERİZASYONU VE ANTİMİKROBİYAL ÖZELLİKLERİ

YÜKSEK LİSANS TEZİ

Pınar ARPAÇAY
(60071106)

Fen Bilimleri Enstitüsü

Nanoteknoloji Yüksek Lisans Programı

Tez Danışmanı: Yrd. Doç. Dr. Uğur TÜRKAN

EKİM 2013

Pınar ARPAÇAY, a **M.Sc** student of GU **Institute of Science** student ID 60071106, successfully defended the **thesis** entitled "**CHARACTERIZATION AND ANTIMICROBIAL PROPERTIES OF MULTIPLE LAYER SILK FIBROIN/HYALURONIC ACID FILM ON CoCrMo ALLOY**", which she prepared after fulfilling the requirements specified in the associated legislations, before the jury whose signatures are below.

Thesis Advisor : **Assist. Prof. Dr. Uğur TÜRKAN** ....
Gediz University

Co-advisor : **Prof. Dr. Oğuz BAYRAKTAR** ....
İzmir Institute of Technology

Jury Members : **Assist. Prof. Dr. Uğur TÜRKAN** ....
Gediz University

Prof. Dr. Oğuz BAYRAKTAR ....
İzmir Institute of Technology

Prof. Dr. Mehmet E. Ş. ÖZSÖZ ....
Gediz University

Assist. Prof. Dr. Aylin Ş. ÜRKMEZ ....
Ege University

Assist. Prof. Dr. Ömer DEMİR ....
Şifa University

Date of Submission : 11 November 2013
Date of Defense : 09 October 2013

FOREWORD

First and foremost, I would like to express my sincere thanks to my supervisor, Assist. Prof. Dr. Uğur TÜRKAN for his guidance, invaluable support, and encouragement for the successful completion of my thesis.

I also would like to thank to my co-supervisor, Prof. Dr. Oğuz BAYRAKTAR for allowing me to research in his laboratory at İzmir Institute of Technology and for his scientific support and help.

I would like to express my special appreciation to Dean of Faculty of Engineering and Architecture, Prof. Dr. Turan BATAR for his support and contribution during my research period. This thesis would not exist without his help.

I gratefully thank Res. Asst. İpek ERDOĞAN for spending her time for helping me at each stages of the thesis work. Her friendship and support was very valuable for me. I also thank Res. Asst. Mehmet Emin USLU for his help.

I am deeply grateful to Dr. John L. Reno and Assoc. Prof. Dr. Selim SOLMAZ for their contribution to my academic career.

I would like to thank my lab-mates, Sümeyra KARAKAYA GÖKALP and Gülşah MALGIR for their friendship and help during my master's years. I also would like to thank Hasan AYDIN for taking AFM images and his help.

I would like to give my undying thanks to my dear friend, Selmin EREN for lending me an ear when needed, and offering her precious opinions and advice all the time. I also would like to thank Baran YILDIRIM for their friendship and support. I thank Emine Tuğba KOCABIYIK for her moral support.

Last, but definitely not least, I dearly thank my parents, Tomris ARPAÇAY and Hüseyin ARPAÇAY and my sister, Selin ARPAÇAY KUDUĞ. I would not be here without their endless love and constant support.

October 2013 Pınar ARPAÇAY

TABLE OF CONTENTS

Page

ABBREVIATIONS

AFM : Atomic Force Microscopy
Ala : Alanine
ATR-FTIR : Attenuated Total Reflectance Fourier Transform Infrared
B. mori : Bombyx Mori
CG : Gelatin
CHI : Chitosan
CoCrMo : Cobalt-Chrome-Molybdenum
C_p : Total Biopolymer Concentration
fcc : Face Centered Cubic
GAGs : Glycosaminoglycans
Gly : Glycine
HA : Hyaluronic Acid
HAp : Hydroxyapatite
hcp : Hexagonal Close Packed
IEP : Isoelectric Point
IR : Infrared
LBL : Layer-by-Layer
μ**e** : Electrophoretic Mobility
PEMs : Polyelectrolyte Multilayers
R : Weight Ratio
Ra : Average Surface Roughness
Rq : Root Mean Square
S. aureus : *Staphylococcus aureus*
SD : Sulfadiazine Sodium
SEM : Scanning Electron Microscopy
Ser : Serine
SF : Silk Fibroin
XRD : X-Ray Diffraction

LIST OF TABLES

LIST OF FIGURES

CHARACTERIZATION AND ANTIMICROBIAL PROPERTIES OF MULTIPLE LAYER SILK FIBROIN/HYALURONIC ACID FILM ON CoCrMo ALLOY

SUMMARY

This research aimed to characterize the pH-induced complexation of multiple layer silk fibroin (SF) and hyaluronic acid (HA) films on CoCrMo alloys and investigate the antimicrobial properties of these films.

In the present study, consisted of six, ten and fourteen layers of three type films which are called SF, SF/HA complex and SF/HA layer-by-layer (LBL) were coated on CoCrMo alloys. In the literature, it was known that SF and HA complexes were occurred within the pH-range of 2.5-3.5, disregarding of the biopolymer ratio, mixing order and total biopolymer concentration. To investigate the effect of pH on the morphology/properties of the films on CoCrMo alloys, three different pH values were chosen: 3.0, 3.5 and 5.5. Surface structures of films were investigated by Attenuated Total Reflectance Fourier Transform Infrared Spectroscopy (ATR-FTIR) and X-Ray Diffraction (XRD) and morphology of films were searched by Scanning Electron Microscopy (SEM) and Atomic Force Microscopy (AFM). All samples were treated with methanol, a conformation transition was aimed to stimulate from silk I to silk II to make the films insoluble and to increase the mechanical characteristics. Characteristic IR absorption peaks for silk I and silk II structures were observed by ATR-FTIR spectroscopy for all samples at pH 3.0, 3.5 and 5.5. The XRD spectra of fourteen layer of SF/HA complex and SF/HA layer-by-layer films on CoCrMo alloys at pH 3.5 showed that the films are amorphous structure due to the inorganic phase. SEM images showed that at pH 3.0 and 3.5, as the working pH values close to the isoelectric point of fibroin (IEP=3.9), SF molecules tend to more aggregate. However, at pH 5.5, the fibres of SF are moved everywhere of the surface due to the working pH which is far away to the IEP of fibroin. As is seen for SEM images, at pH 3.5, colloidal particles are observed for all multilayer SF/HA complex and SF/HA layer-by-layer films on CoCrMo alloys due to the working solution pH close to IEP of fibroin in AFM images. AFM images also clearly indicated that the film thickness and surface roughness of LBL coated specimens is almost higher than those of complex coated films on the investigated specimens.

Antibiotic called levofloxacin was loaded into the fourteen layer of SF/HA complex and SF/HA layer-by-layer films to enhance the film properties. These antibiotic loaded films on CoCrMo alloys at pH 3.5 were investigated by ATR-FTIR spectroscopy and SEM. Characteristic IR absorptions bands were observed by ATR-FTIR spectroscopy. Compared to the without antibiotic loaded films, the surface of the levofloxacin loaded samples showed smoother and more uniform structure in SEM images.

Antimicrobial properties of the fourteen layer of SF/HA complex and SF/HA layer-by-layer films on CoCrMo alloys at pH 3.5 were investigated by colony counting method. Antibiotic loaded samples showed lower bacterial attachment as compared to the other samples. In conclusion, antibiotic loading is an efficient way to reduce the bacterial attachment and this will probably reduce the infection risks.

CoCrMo ALAŞIMINDA ÇOKLU TABAKALI İPEK FİBROİN/HYALURONİK ASİT FİLMİNİN KARAKTERİZASYONU VE ANTİMİKROBİYAL ÖZELLİKLERİ

ÖZET

Bu çalışma, CoCrMo alaşımları üzerinde çoklu tabakalı ipek fibroin (SF) ve hyaluronik asit (HA) filmlerinin pH’a bağlı olarak kompleks oluşturmasının karakterize edilmesini ve bu filmlerin antimikrobiyal özelliklerinin incelenmesini amaçlamıştır.

Mevcut çalışmada, CoCrMo alaşımları üzerinde altı, on ve on dört tabakadan oluşan SF, SF/HA kompleks ve SF/HA tabaka-tabaka (LBL) olarak adlandırılan üç çeşit film kaplanmıştır. Literatürde, toplam biyopolimer konsantrasyonu, karışım sırası ve biyopolimer oranı dikkate alınmaksızın, SF ve HA kompleksinin pH 2.5-3.5 aralığında oluştuğu bilinmektedir. CoCrMo alaşımları üzerindeki filmlerin morfolojisine/özelliklerine pH’ın etkisini incelemek için, üç farklı pH değerleri seçilmiştir: 3.0, 3.5 ve 5.5. Filmlerin yüzey yapıları Fourier Dönüşümlü Toplam Yansıması Azaltılmış İnfrared Spektroskopisi (ATR-FTIR) ve X-Işınları Kırınımı (XRD) ile incelenmiş ve filmlerin morfolojileri Taramalı Elektron Mikroskopu (SEM) ve Atomik Kuvvet Mikroskopu (AFM) ile araştırılmıştır. Bütün örnekler methanol ile muamele edilmiştir, mekanik özellikleri arttırmak ve filmleri çözünmez hale getirmek için konformasyon dönüşümününün ipek I’den ipek II’ye uyarılması amaçlanmıştır. pH 3.0, 3.5 ve 5.5’te bütün örnekler için, ipek I ve ipek II yapılarının karakteristik IR absorpsiyon pikleri ATR-FTIR spektroskopisi ile gözlenmiştir. pH 3.5’te CoCrMo alaşımı üzerindeki on dört tabakalı SF/HA kompleks ve SF/HA tabaka-tabaka filmlerinin XRD spektraları, inorganik faz nedeniyle filmlerin amorf yapıda olduklarını göstermiştir. SEM görüntüleri, pH 3.0 ve 3.5’te, çalışma pH’ının fibroinin izoelektrik noktasına (IEP=3.9) yaklaştıkça, SF molekülerinin daha çok bir arada toparlanma eğiliminde olduklarını göstermiştir. Ancak pH 5.5’te, SF fiberleri, çalışılan pH’ın fibroinin izolektrik noktasından uzak olması nedeniyle yüzeyin her yerine ilerlemiştir. SEM görüntülerinde görüldüğü gibi, AFM görüntülerinde de pH 3.5’te, kolloidal parçacıklar çözelti çalışma pH’ının fibroinin izoelektrik noktasına yakın olması nedeniyle gözlenmiştir. Aynı zamanda AFM görüntüleri, LBL kaplı örneklerin film kalınlığının ve yüzey pürüzlülüğünün incelenen kompleks kaplı film örneklerinden hemen hemen daha yüksek olduğunu göstermiştir.

Levofloksasin olarak adlandırılan antibiyotik, film özelliklerini arttırmak için on dört kaplı SF/HA kompleks ve SF/HA tabaka-tabaka filmlere yüklenmiştir. pH 3.5’te CoCrMo alaşımları üzerindeki bu antibiyotik yüklü filmler, ATR-FTIR spektroskopisi ve SEM ile incelenmiştir. Karakteristik IR absorbsiyon bandları ATR-FTIR spektroskopisi ile gözlenmiştir. Antibiotik yüklü olmayan filmler ile kıyaslandığında, SEM görüntülerinde levofloksasin yüklü örneklerin yüzeyi daha düz ve daha eşdağılımlı yapı göstermiştir.

pH 3.5’te, CoCrMo alaşımı üzerindeki on dört tabakalı SF/HA kompleks ve SF/HA tabaka-tabaka filmlerinin antimikrobiyal özellikleri koloni sayma methodu ile incelenmiştir. Antibiyotik yüklü örnekler, diğer örnekler ile kıyaslandığında daha az bakteri tutunumu göstermişlerdir. Sonuç olarak, antibiotik yükleme bakteri tutunumunu azaltmak için etkili bir yoldur ve bu yöntem enfeksiyon risklerinini indirgeyecektir.

1. INTRODUCTION

1.1 Purpose of Thesis

The main goal of this study is to carry out the multiple layer silk fibroin/hyaluronic acid films on CrCrMo alloy. Silk fibroin and hyaluronic acid can be successfully used to generate the complex films. A specific antibiotic called levofloxacin will be loaded to the films to enhance the film properties and to reduce the inflammation risk due to bacteria/microbe. In particular, the pH-induced multiple layer silk fibroin/hyaluronic acid films will be characterized and antimicrobial properties of the films will be investigated, respectively.

Attentuated Total Reflectance Fourier Transform Infrared Spectroscopy *(*ATR-FTIR), X-Ray Diffraction (XRD), Scanning Electron Microscopy (SEM) and Atomic Force Microscopy (AFM) will be used to characterize the films and antimicrobial activities of the films will be investigated by colony counting method. Staphylococcus aureus is a candidate bacteria in this research.

The results of this research should lead to an understanding of the behavior of silk fibroin/hyaluronic acid films on CoCrMo alloys. This research is one of the first attempts conducted for the prevention of infections on CoCrMo using biodegradable polymers. This will also motivate us to develop a new aspect for biomaterials.

1.2 CoCrMo Alloys

CoCrMo alloys are metallic biomaterials and are broadly utilized as orthopedic implant materials. They are very stable materials and have been used since 1930. For clinical applications, these casting alloys have been employed in the femur constituent of artificial knee joints. On the other hand, wrought alloys can be utilized as artificial components such as knee stems, hip heads, metal-on-metal hip joint bearings, and hip stems (Okazaki 2008).

A total hip joint prosthesis is principally made up of two components: an acetabular cup located in the pelvis and a stem transferred into the femur or thigh bone. Figure

1.1 represents the diagram of a hip replacement. The femoral stem places down into femur. The ball over the femoral stem is termed the femoral head fits into the hip and joint in the pelvis. An ultra-high molecular weight polyethylene (UHMWPE) liner places inside the acetabular cup and enables the articulating surface for the femoral head (Long and Rack 1998, Duisabeau, Combrade et al. 2004, Katti 2004). The two components of the hip implant have been produced utilizing a several of substances e.g. polymers, composites, metals and ceramics.

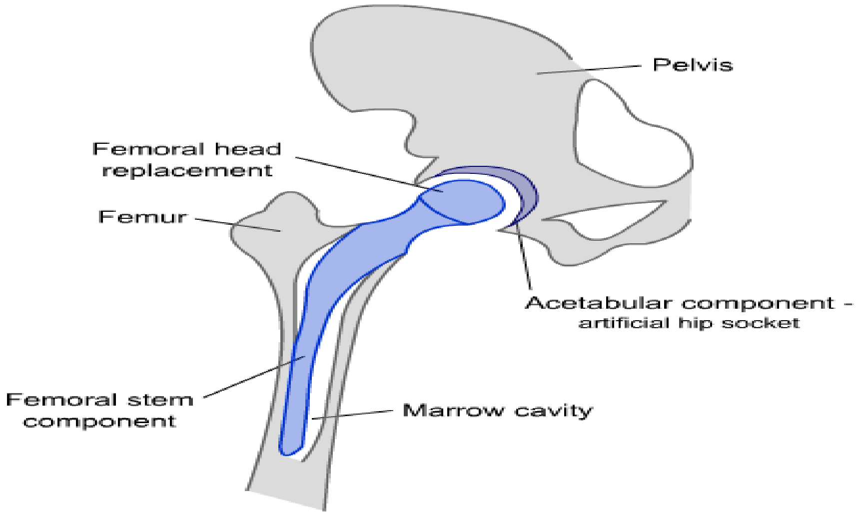

Figure 1.1 : The diagram of a hip replacement, adapted from (DoITPoMS).

Lately, metal-on-metal (MoM) hip replacements ground on CoCrMo alloys have progressively get the adopted option for younger and/or more active patients owing to their longer service duration, reduced inflammatory osteolysis and superior wear resistance arising from such tools (Schmalzried 2004, Schmalzried 2005, Yan, Neville et al. 2007). CoCrMo femur stems has with achievement also been operated as cemented stems, due to elastic modulus proximate to bone-cement (Schweizer, Riede et al. 2003, Schweizer, Luem et al. 2005).

CoCrMo alloys are formed 62-67 % cobalt and 27-30 % chrome, besides that comprise 5-7 % molybdenum and all together below 1 % of manganese, iron, nickel, and silicon. Carbon is included to further increase durability (Nevelos, Shelton et al. 2004).

CoCrMo alloys are preferred for many reasons for orthopedic applications. Compared to austenitic stainless steels, they are high corrosion resistance. As against titanium and its alloys, these alloys are high wear resistance. However they have less plastic processability compared to titanium, titanium alloys and stainless steels. On the other hand, most heads of artificial joints are formed CoCrMo alloys due to high corrosion resistant compared to stainless steel and high wear resistance in comparison with titanium alloys (Hanawa, Nakazawa et al. 2005).

CoCrMo alloys utilized as biomaterials due to involving osteocompatibility, surface compatibility and mechanical compatibility for orthopedic applications.

Surface compatibility of these alloys are based on fundamental compatible chemical features of the materials within the human body such as, not causes to carcinogenic and mutagenic influence, not leading to allergic inflammatory, toxic effects and immunological reaction.

Mechanical compatibility of CoCrMo alloy is in regard to its characteristics of having corrosion-resistant, non-magnetic and wear-resistant. Perfect corrosion resistance of the CoCrMo alloy results from the existence of highly thin passive oxide film that occurs on the material surface. Excellent corrosion resistance of the material arises from the presence of an extremely thin passive oxide layer that spontaneously forms on the alloy surface. When CoCrMo alloy exposed to air, thin passive oxide film occurred on the material. X-Ray photoelectron spectroscopy (XPS) results demonstrate that its structure is especially Cr_2O_3 oxide with small addition from Mo and Co oxide. The thickness of the oxide layer is 1.8 nanometers (Milosev and Strehblow 2003). Thin oxide layers also occurs on the other implant surfaces such as stainless steels, titanium and its alloys and help as a block to corrosion processes in alloy structures. In the lack of thin oxide layers, the driving force for corrosion of metallic implants are so high (Türkan 2004).

CoCrMo alloy is also known as osteocompatible material. It refers that bone generating cells (osteoblasts) can colonize on the material surface and create new bone tissue (Sato and Webster 2004, Çağlar 2007).

1.3 Silk Fibroin

Silk Fibroin (SF) is a natural polymer biosynthesized by several of spiders and insects. The most defined silks are produced by the domestic silkworm *Bombyx mori,* which has been utilized in textile manufacture, clinical sutures and lately as a scaffold for tissue regeneration due to its noticeable mechanical properties (Bunning, Jiang et al. 1993, Kaplan, Mello et al. 1997, Holmes 2002, Zhang, Yan et al. 2009, Wenk, Merkle et al. 2011). The mechanical features of several types of silk are showed in Table 1.1. *Bombyx mori* silk is made up of two types of protein, sericin and fibroin. Sericin is the water-soluble glue-like protein that encircles and links the fibroin fibers, fibroin is the constructional fibrous protein and forms 70% of the whole silk (Magoshi, Magoshi et al. 1996). Sericin can be quickly seperated from the silk fiber by a traditional degumming procedure (process of silk fibers with an alkali salt solution at 100 °C).

Table 1.1 : The mechanical features of several types of silk, adapted from (Altman, Diaz et al. 2003).

Material	Ultimate Tensile Strength (MPa)	Modulus of Elasticity (GPa)	% Strain at Break
***Bombyx mori* silk with sericin**	500	5-12	19
***Bombxy mori* silk without sericin**	610-690	15-17	4-16
Spider Silk	875-972	11-13	17-18

SF is described by recurrent hydrophobic and hydrophilic peptide series (Hofmann, Foo et al. 2006) and is formed heavy and light chain polypeptides of ~390 kDa and ~26 kDa, respectively, connected with a disulfide bond at the C-terminus of the two subunits. The principal construction of *Bombyx mori* SF biopolymer is defined by the existence of three amino acids in an approximately 3:2:1 ratio: glycine (45%), alanine (30%), and serine (12%); and the series is prevailed by [Gly-Ala-Gly-Ala-Gly-Ser]*n*. Besides that, SF chains cover amino acids with bulky and polar side chains, especially valine, acidic amino acids and tyrosine (Mondal, Trivedy et al. 2007). The chemical structure of SF is represented in Figure 1.2.

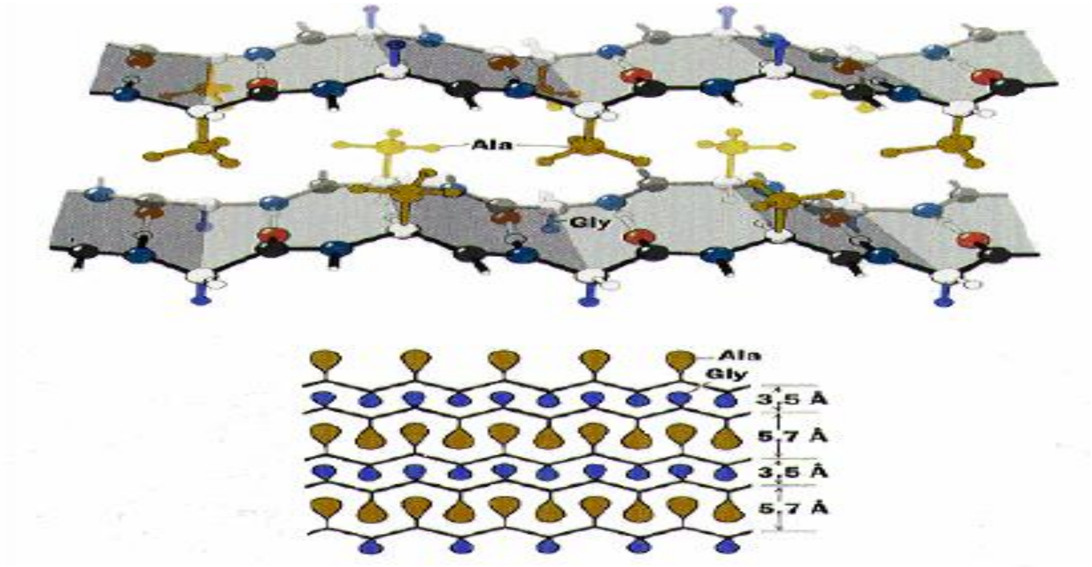

Figure 1. 2 : Chemical structure of silk fibroin, adapted from (Serianni).

Two different conformations, silk I (α-helix, random coil) and silk II (β-sheet) are defined as the major secondary structures of SF. Silk I is the water-soluble conformation of fibroin that simulates its liquid texture in the silkworm glands. On the other hand, silk II is the well-aligned anti-parallel β-sheet structure of the water-insoluble spun fibers. In β-sheet structure, the polypeptide chains are oriented and neighboring chains are linked with hydrogen bonds (>C=O···HN<) (Yamada, Tsuboi et al. 2003). The widespread way to dominate SF in β-sheet conformation and hence activate water insolubility is a treatment with methanol (Marsh, Corey et al. 1955, Asakura, Kuzuhara et al. 1985, Ishida, Asakura et al. 1990, Monti, Freddi et al. 1998). In addition to, high temperatures (Motta, Fambri et al. 2002), a pH near the isoelectric point of SF (around 3.9), the use of salts (Dicko, Kenney et al. 2004, Kim, Park et al. 2004, Zong, Zhou et al. 2004, Wang, Wenk et al. 2007) and shear-force (Jin and Kaplan 2003, Xie, Zhang et al. 2006) were demonstrated to enhance its β-sheet content. Subject to water vapor has been represented to be an option to activate water insolubility (Min, Jeong et al. 2006, Wenk, Wandrey et al. 2008). Furthermore slow freezing rates helps to enhance the β-sheet based crystallinity (Li, Lu et al. 2001, Nam and Park 2001). Crystallinity is the base for the excellent mechanical strength of SF. However, an extreme raise in crystallinity decreases its flexibility and occur more brittle materials. Annealing in water or water vapor treatments were represented to lead to less β-sheet conformation and keep better elasticity as against to methanol treatments (Asakura, Kuzuhara et al. 1985, Jin, Park et al. 2005).

Recently published silk III structure of fibroin indicates its surfactant behaviour and constructs at the water-air interface in thin films (Valluzzi, Gido et al. 1999).

In the recent times, the utilization of SF as a biomaterial has enlarged for researches in vitro and in vivo owing to the unique integration of structural, biocompatible and mechanical characteristics indicated by this biopolymer (Sakabe, Ito et al. 1989, Santin, Motta et al. 1999, Park, Ha et al. 2001). Schematic representation of features of fibroin is shown in Figure 1.3.

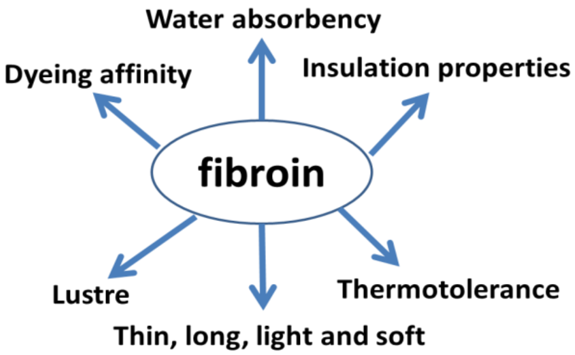

Figure 1.3 : Schematic representation of features of fibroin, adapted from (Mondal, Trivedy et al. 2007).

SF is known to possess a biological response parallel to such other substances as polystyrene, and is nowadays a common option for biomaterial applications such as tissue-engineering scaffolds (Sofia, McCarthy et al. 2001). SF also has been utilized as a scaffold for hepatic tissue, cartilage, anterior cruciate ligaments, reticular connective tissue and bone formation (Sofia, McCarthy et al. 2001, Altman, Horan et al. 2002, Dal Pra, Freddi et al. 2005, Hu, Lv et al. 2006, Silva, Motta et al. 2008). The other applications for SF as a biomaterial cover wound dressings, drug delivery systems and contact lenses.

SF represents great biodegradability, low inflammatory response, and good antithrombogenic features. These characteristics are necessary for biocompatible materials, and it is supposed that SF will be a powerful polymer for many biocompatible studies (Bailey 2013).

Layer-by-layer (LBL) assembly of materials is the potential method to change surface features (Decher 1997). LBL deposition can be used to make SF-based biomaterials. In the literature, anisotropic chitosan (CHI) and SF multilayer films on a solid substrate were assembled using LBL technique (Nogueira, Swiston et al.

2010). CHI/SF fiber coating can simultaneously increase biocompatibility and stimulate the administrable growth (via film surface chemistry and morphology) of inorganic crystals in a well-defined direction. In another research, a fully aqueous stepwise coating process of SF on a solid substrate is reported (Wang, Kim et al. 2005). The distinction with this process from conventional polyelectrolyte layer-by-layer method is that an interposing drying treatment was utilized to check the stability and structure of the self-assembled SF. The multilayer films were stable under physiological situations and promoted human bone marrow stem cell adhesion, differentiation and growth. In another application, Kozlovskaya et al. investigated that the ability of SF to LBL assemble with such synthetic (poly-(methacrylic acid) (PMAA) and poly(N-vinylcaprolactam) (PVCL)) and natural polyphenol, tannic acid (TA)) molecules, at low and neutral pH values (Kozlovskaya, Baggett et al. 2012). They explored that linking SF with biocompatible materials via hydrogen bonding holds a remarkable prospect for constructing new biomimetic materials with controlled features and enhanced biological compatibility. In another study, Wang et. al. prepared SF through the LBL deposition process and used as carriers to incorporate model drugs such as Rhodamine B, Even Blue and Azoalbumin (Wang, Hu et al. 2007). These new coatings supplied an ideal choice to regulate morphology, structure and hence release kinetics. Kino et al. fabricated multilayered films comprising of SF and hydroxyapatite (HAp) by consecutive lamination utilizing untreated SF and HAp-deposited SF films (Kino, Ikorna et al. 2007). The conclusions demonstrated that HAp-deposited SF films and SF films display equal degrees of cell adhesion and alkaline phosphatase activities. Recently, Li et al. created multilayered SF films incorporating sulfadiazine sodium (SD) using different concentrations of SD (Li, Tang et al. 2013). They found that the SF incorporating SD has great characteristics and it has the facility to be utilized as artificial skin for burned patients. In another examination Mandal et al. researched that LBL films based on SF and gelatin in aqueous solution for controlled drug release utilizing three different molecular weight model compounds (Mandal, Mann et al. 2009). The release profile of model compounds displayed relevant on multilayer film degradation for sustained release. The release kinetics was assessed as a function of gelatin multilayers proposing their potential act in limiting initial burst causing continuous compound release. Lately, Shchepelina et al. used a one component silk-on silk LBL method to create such biodegradable and biocompatible microcapsules

(Shchepelina, Drachuk et al. 2011). The silk microcapsules displayed great stability and superior permeability which was easily controlled by the thickness of the shells. In another study, Chi et al. fabricated multilayered films comprising of SF and chitosan (CHI) on titanium thin film surfaces utilizing LBL method (Cai, Hu et al. 2007). In vitro studies represented that CHI/SF multilayers increased cell biocompatibility of titanium. Recently, Vidal et al. indicated that SF functionalized with titanium binding peptide (TiBP) and fibronectin-derived arginine–glycine–aspartic acid (RGD) showed an encouraging attempt to alter cell-biomaterial interfaces, starting novel aspects for implantable medical materials (Vidal, Blanchi et al. 2013).

1.4 Hyaluronic Acid

Hyaluronic acid (HA) is a natural and unbranched polymer consisted of disaccharide repeats of D-glucuronic acid (GlcUA) and N-acetylglucosamine (GlcNAc) connected alternately by β-1, 3 and β-1, 4 glycosidic bonds with a molecular weight up to 10^7 Daltons (Da) (Long Liu 2011). The chemical structure of HA is represented in Figure 1.4.

Karl Meyer and John Palmer isolated a new material from the vitreous body of cows' eyes in 1934. They discovered that the matter comprised of an uronic acid and an aminosugar, and called the polysaccharide "hyaluronic acid" from hyaloid (vitreous) + uronic acid (Meyer and Palmer 1934).

HA is a member of the glycosaminoglycans (GAGs), being structurally the most basic among GAGs. It is also the only one not covalently linked to a core protein, not synthesized in Golgi apparatus, and the only non-sulfated GAGs (Grigorij Kogan 2007).

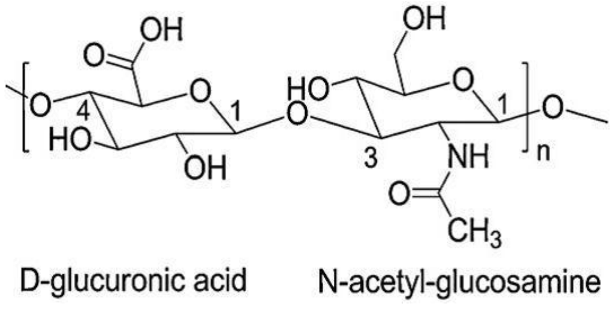

Figure 1.4 : Chemical structure of hyaluronic acid, adapted from (Carole E. Schanté 2011).

HA is almost everywhere in the human organism and in other vertebrates. The large amounts of HA are observed in the extracellular matrix (ECM) and soft connective tissues (Laurent 1998).

HA is also found in the capsules of some bacteria (e.g., strains of Streptococci), but is not present in fungi, insects and plants. The highest amount by far of HA is present in rooster combs. Recently, a detailed study of the sources from which HA can be separated has been researched (Aviva Shiedlin 2004). A short tabulation of the existence of HA in several animal tissues and its concentration is showed in Table 1.2 (Grigorij Kogan 2007).

Table 1.2 : Existence of HA in several animal tissues and its concentration, adapted from (Grigorij Kogan 2007).

Tissue or Body Fluid	**Concentration (µg/ml)**
Rooster comb	7500
Human umbilical cord	4100
Human joint (synovial) fluid	1400-3600
Bovine nasal cartilage	1200
Human vitreous body	140-340
Human dermis	200-500
Human epidermis	100
Rabbit brain	65
Rabbit heart	27
Human thoracic lymph	0.2–50
Human urine	0.1–0.3
Human serum	0.01–0.1

HA is frequently used in biomedical industry such as applications of orthopedic, antiadhesion, cardiovascular, dermatology and wound-healing. On the other side HA is very effective for ophthalmologic surgery and viscosupplementation (Necas, Bartosikova et al. 2008). HA has crucial importance in skin. It can change compressibility and dermal volume due to immobilizing water in tissue. It can effect differentiation, tissue repair and cell proliferation. The changes in HA observed with wound healing, ageing and degenerative diseases further evidence its significance (Juhlin 1997).

HA exists in cartilage in low content but it functions as a serious structural material of the matrix. It generates an aggregation center for aggregan, a large chondrotin sulfate proteoglycan that keeps its macromolecular assembly in the matrix because of particular HA-protein interplay (Prehm 2000).

The high concentration of high molar mass of HA supports essential lubrication for the joint in synovial fluid. It plays an important role as shock absorber, decreasing friction of the moving bones and minimizing wear of the joint (Soltes, Mendichi et al. 2006). HA is also commonly preferred in medicine due to non-inflammatory properties. It is known as an inert biomaterial.

In physiological situations, HA is known as a polyanion and its p*K*a value is predicted to be 2.9 (Soltes and Mendichi 2003). Another study in the literature represented that the p*K*a value of HA is 2.5 (Malay, Bayraktar et al. 2007). Even at dilute concentrations e.g. 0.1 wt%, HA is an extremely viscous solution. The models of hyaluronic acid behaviour in solution is represented in Figure 1.5 (Hardingham 2004). Light scattering and intrinsic viscosity studies submitted that HA chains adopts an expanded 'somewhat-stiff' random coil conformation in solution (Laurent and Gergely 1955, Lapcik, Lapcik et al. 1998). It is known that at pH 2.5 HA solutions were presented a 'paste-like' structure on gentle shaking and more elastic (Gibbs, Merrille et al. 1968), which was based to emphasised stiffening of HA chains. It was evaluated to come about in consequence of a critical balance between the attractive and repulsive interactions functioning among the molecular chain structures (Malay 2005). On the other hand, it was published that HA has a more compact, flexible random coil form at alkaline pH (Ghosh, Kobal et al. 1993).

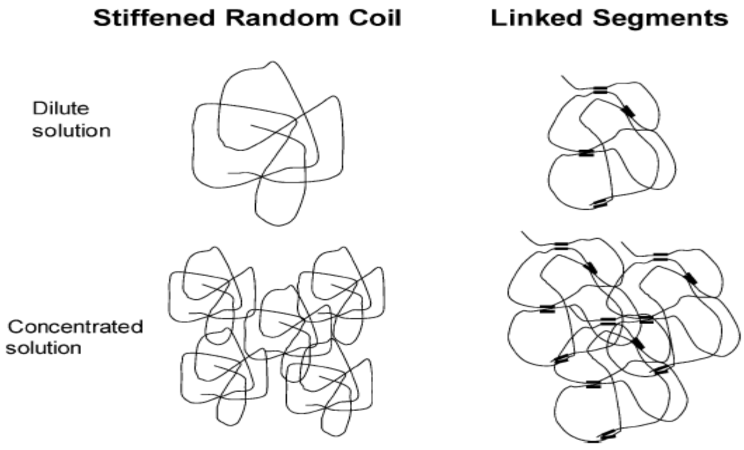

Figure 1.5 : Models of HA structure in solution, adapted from (Hardingham 2004).

Layer-by-layer (LBL) assembly of materials is the potential method to change surface features (Decher 1997). LBL deposition can be used to make HA-based biomaterials. In recent times, LBL deposition of HA and chitosan has been published as a technique of reconstruction for damaged blood vessels (Thierry, Winnik et al. 2003). In another research, nonbiofouling HA micropatterns were utilized to immobilize cells and proteins to glass surfaces. Following ionic deposition of poly-l-lysine (PLL) to HA patterns was applied to change the HA surfaces from cell repulsive to adherent by this way helping the adhesion of a second cell type. The benefit of this application to pattern co-cultures of hepatocytes or embryonic stem cells with fibroblasts was represented (Khademhosseini, Suh et al. 2004). Chua et al. fabricated on titanium via polyelectrolyte multilayers (PEMs) of HA and chitosan (CHI) incorporated with surface-immobilized cell-adhesive arginine-glycine-aspartic acid (RGD) peptide (Chua, Neoh et al. 2008). This multilayer film enhanced biocompatibility and displayed durable antibacterial characteristics on titanium surfaces. Recently, Li et al. researched that collagen (COL)/HA PEMs coating on titanium surface (Li, Luo et al. 2012). In vitro studies represented that multilayer coating on titanium could speed up the proliferation and differentiation of preosteoblasts cells. Another group modified polyethylene terephthalate (PET) artificial ligament grafts with LBL self-assembled coatings of (HA) and cationized gelatin (CG) (Li, Chen et al. 2012). Attributed the conclusions they represented that PET grafts deposited with HA/CG have remarkable importance as substitutes for ligament reconstruction. Schneider et al. deposited cationic modified hyaluronan (HA^+) and hyaluronan (HA) of controlled thicknesses with LBL technique

(Schneider, Picart et al. 2007). They demonstrated that NIH3T3 fibroblasts were excellently viable on multilayer films with but preference for HA ending films.

1.5 Complex Coacervation of Silk Fibroin and Hyaluronic Acid

The research on interplay between protein and polysaccharide has been broadly subjected to many scientists in connection with its various applications in biomedical and biotechnological studies (Malay, Bayraktar et al. 2007).

Two kinetic processes occur when protein and polysaccharide are mixed. They are called as complex coacervation or phase separation. A thermodynamic phase separation occurs if the polysaccharide and protein are incompatible. In this system, protein and polysaccharide repel each other. In other respects, the biopolymers blend excluding the solvent from their environment, if the protein and polysaccharide attract each other thanks to electrostatic interactions. It brings about to the formation of protein-polysaccharide complexes (Tolstoguzov 2003, Turgeon, Beaulieu et al. 2003). The phase separation of a liquid polymer rich-phase from a macromolecular solution is defined as complex coacervation. This system presents the separation of two immiscible liquid phases in a colloidal system. Coacervate is the more concentrated phase in colloidal component and equilibrium solution is the other phase (de Kruif, Weinbreck et al. 2004).

Protein-polysaccharide coacervates are especially significant in, protein purification (Wang, Gao et al. 1996), enzyme immobilization (Jiang and Huang 2004), antigen delivery (Burgess and Ponsart 1998), design and production of biomaterials for cell micropatterning (Magnin, Dumitriu et al. 2003) and stabilization of food products (Jones, Lesmes et al. 2010).

In the literature, electrophoretic mobilities (μe) of silk fibroin/hyaluronic acid were researched to determine the most suitable area for the formation of the electrostatic complexes (Malay, Bayraktar et al. 2007). At pH 3.90, a zero value was determined. This value demonstrated that pH 3.90 is the isoelectric point (IEP) of silk fibroin. Electrophoretic mobility analysis represented that SF is positively charged under the pH 3.90, whereas over the pH 2.50 HA is negatively charged. Therefore, complex coacervation of SF/HA was thought between pH 2.50-3.90. Electrophoretic mobility of 0.1 wt% biopolymer dispersions at 20 ◦C is showed in Figure 1.6.

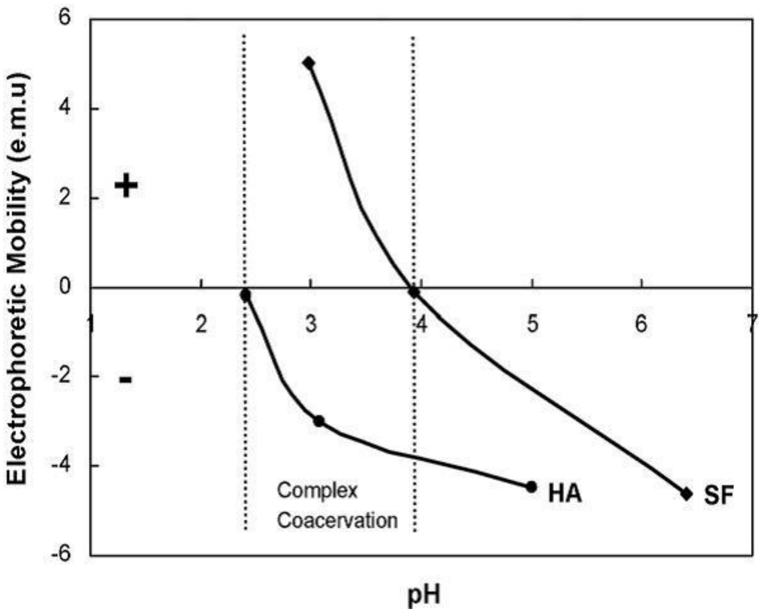

Figure 1.6 : Electrophoretic mobility of 0.1 wt% biopolymer dispersions at 20 °C, adapted from (Malay, Bayraktar et al. 2007).

In the literature, turbidimetric titration method under acidification was also applied to get qualitative data about the complexation of SF/HA (Malay, Bayraktar et al. 2007). This data showed that complexation between SF/HA was pH 2.50-3.50. The titration graph of SF/HA mixtures for the total biopolymer concentration (C_p) 0.5% at SF:HA weight ratio (R) of 32:1 is represented in Figure 1.7. At pH above the IEP of SF, both HA and SF are negatively charged and therefore repulsive coulombic forces inhibited the complexation. In this zone, SF/HA mixtures were soluble and turbidity was stable. At pH under the IEP of SF gave rise to increase in turbidity. And also as displayed in Figure 1.7, at stable C_p, as SF:HA ratio was diminished, maximum turbidity value decreased, which represented that silk fibroin was the limiting polymer for the coacervation.

For the biopolymer mixtures, two-step increase and symmetrical decrease was showed in Figure 1.7. It was thought as the evidence of pH-induced complex coacervation between polymers. Eq. **(1.1)** represents electrostatic interaction between the SF and HA (Malay, Bayraktar et al. 2007).

$$[\text{HA-COO}^-]+[\text{SF-NH}_3^+] \rightleftharpoons [\text{HA-COO}^-][\text{ NH}_3^+\text{-SF}] \quad \textbf{(1.1)}$$

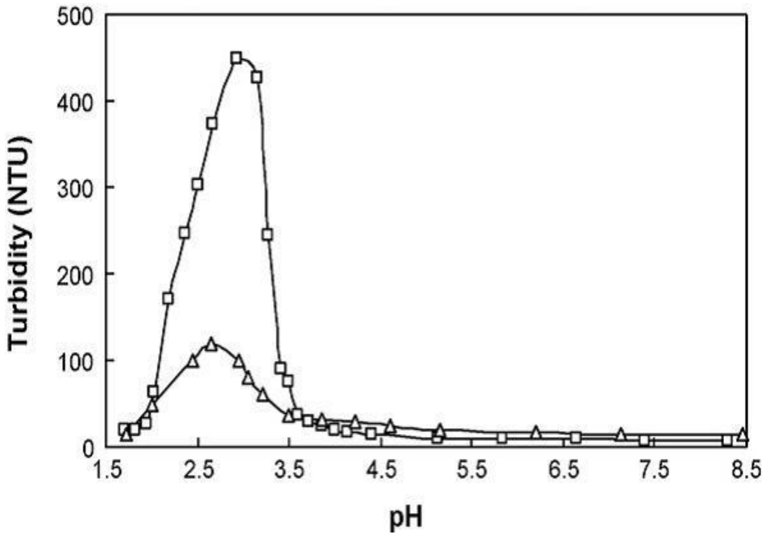

Figure 1.7 : Turbidity of SF-HA system as a function of pH for SF:HA ratio of 32:1 (□) and 16:1 (Δ) for C_p=0.5%, adapted from (Malay, Bayraktar et al. 2007).

1.6 Layer-by-Layer Deposition

Layer-by-layer (LBL) or electrostatic self-assembly (ESA) is a general method to fabricate multilayer films. This technique pioneered by Iler (Iler 1966) further idealized by Decher et al. (Decher, Hong et al. 1992, Decher 1997) is attributed to the serial deposition of oppositely charged polyelectrolytes, forming interpenetrating layers of polymeric complexes as shown in Figure 1.8. This method is a common and versatile way for the controlled production of multimaterial surface coatings on a wide range of surfaces (Decher 1997, Decher 2003).

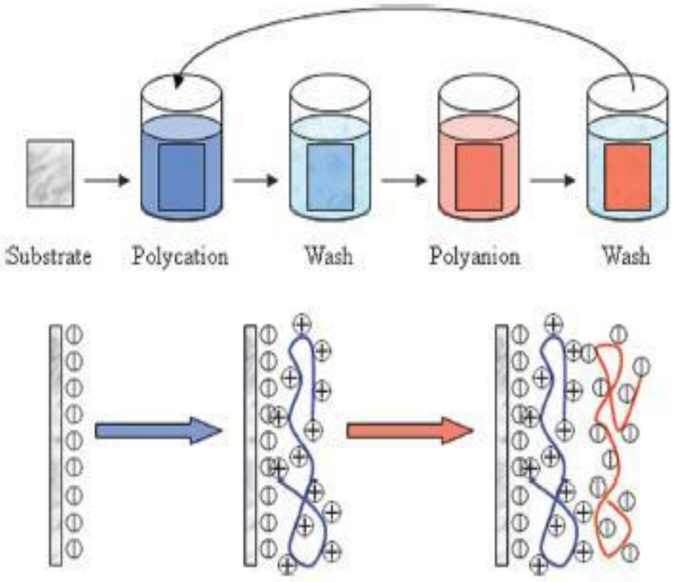

Figure 1.8 : Diagrammatic of LBL self-assembly of a multilayer coating by consecutive adsorption of oppositely charged polyelectrolytes, adapted from (Xiang, Lu et al. 2012).

Self-assembled multilayer structures can be constructed utilizing different materials such as synthetic or natural polyelectrolytes, clay platelets or colloidal particles, a wide variety of proteins and inorganic complexes and clusters (Leguen, Chassepot et al. 2007).

These multilayer structures have been investigated for utilize in a number of technologies, covering biological, (Lee, Cohen et al. 2005, Swiston, Cheng et al. 2008) wetting, (Zhai, Berg et al. 2006, Su, Li et al. 2009) optical, (Wu, Lee et al. 2007) and antifogging (Cebeci, Wu et al. 2006) applications.

Electrostatic interaction is the primarily driving force for layer-by-layer assembly, but the technique can also contain hydrogen bonding, charge-transfer interactions, short-range hydrophobic interactions and van der Waals interactions (Kotov 1999, Lojou and Bianco 2004).

LBL technique presents potential benefits, containing ease of preparation, versatility, ability of combining high loading several kinds of biomolecules within the films, good control over materials texture, and stability under physiological and ambient conditions (Wang, Kim et al. 2005, Johnston, Cortez et al. 2006).

2. EXPERIMENTAL SECTION

2.1 Materials

Cobalt-chromium-molybdenum (CoCrMo) alloy, specified in ISO 5832-3 which has nominal composition of 1 % Ni, 0.75 % Fe, 1.0 % Mn, 1.0 % Si, 0.35 % C, 0.25 % N, 5 % Mo, 26 % Cr and balance Co (all in wt %), used in this study. The specimen geometry was designed as a disk, having 10 mm diameter and 2 mm thickness. Before the coating process all the specimens were polished to mirror like quality. CoCrMo alloy was supplied from TIPSAN TIBBİ ALETLER SAN. ve TİC. A.Ş. (İzmir/Turkey). Silk Fibroin (SF) was supplied in reeled form from Bursa Institute for Silkworm Research (Bursa/Turkey). Hyaluronic acid (HA) sodium salt (MW: 1,600,000 Da, form *Streptococcus equi*) was purchased by Fluka-BioChemica (Buchs, Switzerland) in powder form. Ethanol (absolute GR for analysis) and methanol was supplied from Merck (Darmstadt, Germany). Sodium carbonate (99.5+%) was taken from Aldrich-Chemie (Steinheim, Germany). Calcium chloride-2-hydrate was purchased from Riedel-de Haën (Seelze, Germany). Dialysis tubing (MW Cut-off: 12,000-14,000) was supplied from Sigma (St. Louis, MO, USA). Deionized water was used during all experiments.

For antimicrobial study, methicillin susceptible *Staphylococcus aureus* (*S. aureus*) American Type Culture Collection (ATCC) 29213 was kindly gifted from IZTECH Biochemical Engineering Research Laboratory. Levofloxacin (trade name Tavanic) was purchased in solution form. Nutrient broth was taken from Merck (Darmstadt, Germany).

2.2 Methods

Experimental methods were separated to three parts. The first part contained the preparation of SF and HA stock solutions. Second part clarified the fabrication of multilayer films on CoCrMo alloys. This part divided into four parts in itself: 1) multilayer silk fibroin films on CoCrMo alloys, 2) multilayer SF/HA complex films on CoCrMo alloys, 3) multilayer SF/HA layer-by-layer (LBL) films on CoCrMo alloys, 4) levofloxacin loaded multilayer SF/HA complex and LBL films on CoCrMo alloys. Third and final part consisted of the determination of antimicrobial activities of SF/HA complex and LBL films on CoCrMo alloys.

2.2.1 Preparation of SF and HA stock solutions

Silk fibroin (SF) solution was prepared by following procedure of degumming and dissolution as shown in Figure 2.1. To remove sericin, along the degumming process, raw silk was kept in 50 times (v/w) of boiling aqueous 0.05% Na_2CO_3 for 30 minutes and this operation was done three times. After each process, it was washed with deionized water and the degummed silk was left drying at room temperature. To get aqueous SF solution, 1.2 g degummed silk was put into 20 times (v/w) of Ajisawa's solution ($CaCl_2$/ethanol/water, 111/92/144 in weight) in a Schott bottle. To create a clear solution, the mixture was stirred at 78 °C for 2 hours in a water bath. After two hours, SF solution was dialyzed against deionized water for at least 3 days at 4 °C to remove the neutral salts using a cellulose tubing. Dialysis water was changed frequently. At the end of the 3 days, the dialyzed fibroin solution was filtered with a Filtrak 389 filter paper (Barenstein, Germany) by means of vacuum pump to achieve pure aqueous solution. After the filtration process, final fibroin solution concentration was about 1-2% (w/v). Step-by-step preparation of aqueous silk fibroin solution from raw silk was shown in Figure 2.1.

Hyaluronic acid (HA) was purchased in powder form and it was soluble in water. Along the dissolution process, it is known that HA particles can easily coagulate. For this reason, HA solution was stirred overnight to make solubilization.

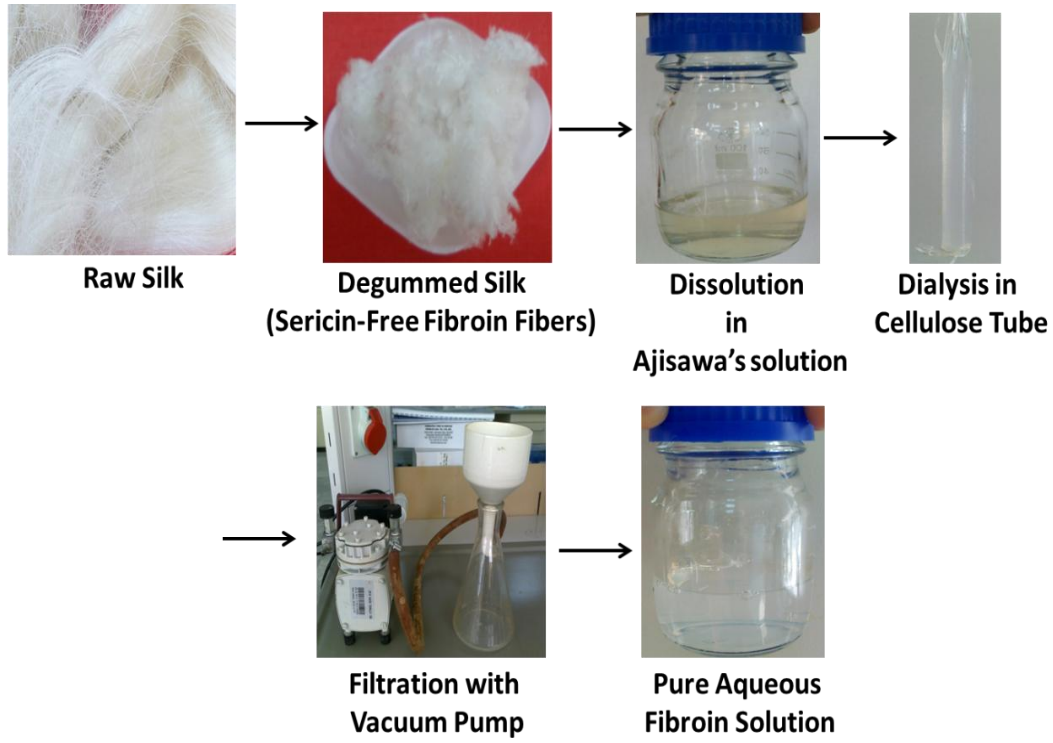

Figure 2.1 : Step-by-step preparation of aqueous silk fibroin solution from raw silk.

2.2.2 Fabrication of multilayer films on CoCrMo alloys

This part divided into four parts in itself. It was planned to investigate the effect of solution pH of different multilayer coatings on CoCrMo alloys. Therefore three different pH values were chosen: 3.0, 3.5 and 5.5, In the literature, the isoelectric point (IEP) of SF was given at pH 3.9 (Malay, Bayraktar et al. 2007). Electrophoretic mobility experiments demonstrated that SF was in the protonated form, positively charged, below pH 3.9, whereas HA was in the deprotonated form above the pH 2.5, and therefore negatively charged. SF/HA complexes were occurred within the pH range of 2.5-3.5, disregarding of the biopolymer ratio, mixing order and total biopolymer concentration (Malay 2005). It was observed that SF was positively charged at pH 3.0 and 3.5 whereas SF was negatively charged at pH 5.5. HA was negatively charged at pH 3.0, 3.5 and 5.5.

During the all experiments, dip coating machine (NIMA Technology Ltd./UK) was utilized for the coatings on CoCrMo alloy. Figure 2.2 represents typical dip coating machine used in all experiments.

Figure 2.2 : Typical dip coating machine used in all experiments.

2.2.2.1 Multilayer SF films on CoCrMo alloys

CoCrMo alloy discs cleaned in ethanol for 15 minutes, then in deionized water for 15 minutes, and dried with N_2 gas. Stock SF solution was dissolved in deionized water with a concentration of 5 mg/mL. SF was positively charged at pH 3.0 and 3.5, whereas it was negatively charged at pH 5.5. Silk fibroin solution was coated on CoCrMo alloy by following the same procedure in each pH value. CoCrMo alloy discs were immersed in SF solution for 10 minutes. After SF adsorption, CoCrMo alloy discs were washed with methanol:water mixture (volume ratio 70:30) for two minutes. Then, CoCrMo alloy discs dried with N_2 gas. The process of coating, washing and drying were repeated according to the required number of layers fabricated. At the end of the experiments, six, ten and fourteen layers of silk fibroin films, coded as $(SF)_6$, $(SF)_{10}$, $(SF)_{14,}$ were obtained on CoCrMo alloys in each pH values, 3.0, 3.5 and 5.5, respectively.

2.2.2.2 Multilayer SF/HA complex films on CoCrMo alloys

The same cleaning procedure was applied to the CoCrMo alloys before complexation process. Stock SF solution was dissolved in deionized water with a concentration of

5 mg/mL. HA aqueous solution was prepared with a concentration of 5 mg/mL. It was known that complex coacervation of SF/HA is within the range of pH 2.5-3.5 (Malay, Bayraktar et al. 2007). SF and HA mixtures for the *C*p's (total biopolymer concentration) of 0.5 wt% at constant SF:HA weight ratio (*R*) of 32:1 were coated on the CoCrMo alloys. After the coating process, CoCrMo alloy discs were washed with methanol:water mixture (volume ratio 70:30) for two minutes. After that, CoCrMo alloy discs dried with N_2 gas. The process of coating, washing and drying were repeated according to the required number of layers fabricated. At pH 3.0 and 3.5, SF and HA mix solution was in the complex coacervation range. SF/HA complex solution was expected to carry both negatively charged at pH 5.5. After all the experiments, six, ten and fourteen layers of SF/HA complex films on CoCrMo alloys obtained at pH 3.0, 3.5 and 5.5 and these films were coded as $(\text{SF/HA complex})_6$, $(\text{SF/HA complex})_{10}$, $(\text{SF/HA complex})_{14}$, respectively.

2.2.2.3 Multilayer SF/HA LBL films on CoCrMo alloys

The same cleaning procedure was applied to the CoCrMo alloys before the coating process. Stock SF solution was dissolved in deionized water with a concentration of 5 mg/mL. HA aqueous solution was prepared with a concentration of 5 mg/mL. At pH 3.0 and 3.5, CoCrMo alloy was immersed in positively charged SF solution for 10 minutes. After SF adsorption, CoCrMo alloy discs were washed with methanol:water mixture (volume ratio 70:30) for two minutes. Then, CoCrMo alloy discs dried with N_2 gas. Following the process at pH 3.0 and 3.5, CoCrMo alloy was immersed in negatively charged HA solution for 10 minutes. Then, these discs were washed with methanol:water mixture (volume ratio 70:30) for two minutes. Thereafter, CoCrMo alloy discs dried with N_2 gas. The process of coating, washing and drying were repeated according to the required number of layers fabricated. The same procedure was repeated at pH 5.5. In this pH, SF and HA were both negatively charged. At the end of the experiments, six, ten and fourteen layers of SF/HA layer-by layer films on CoCrMo alloys obtained at pH 3.0, 3.5 and 5.5 and they were coded as $(\text{SF/HA LBL})_3$, $(\text{SF/HA LBL})_5$, $(\text{SF/HA LBL})_7$, respectively.

2.2.2.4 Levofloxacin loaded multilayer SF/HA complex and LBL films on CoCrMo alloys

The same cleaning procedure was applied to the CoCrMo alloys before the coating process. LBL and complex coating processes on CoCrMo alloys were described in the previous parts. A specific antibiotic called levofloxacin was loaded into the SF/HA complex and LBL films. Antibiotic loading films were coded as (SF/HA complex + Levofloxacin) and (SF/HA LBL + Levofloxacin) on CoCrMo alloys. The working solution pH for levofloxacin loaded complex and LBL coatings was 3.5. Levofloxacin was loaded for only fourteen layers films on CoCrMo alloys. The minimum inhibitory concentration (MIC) value of levofloxacin for *Staphylococcus aureus* (*S. aureus*) strain ATCC 29213 was 0.25 mg/L (Smith, Baltch et al. 2000). And for these coatings, levofloxacin loading concentration was 3×MIC. For (SF/HA complex + Levofloxacin)$_{14}$ on CoCrMo alloy at pH 3.5, levofloxacin was loaded to complex at each layers of film. On the other hand, for (SF/HA LBL + Levofloxacin)$_7$ on CoCrMo alloy at pH 3.5, levofloxacin was loaded to SF only at 1., 7. and 13. layers into the film.

2.2.3 Determination of antimicrobial activites of SF/HA complex and LBL films on CoCrMo alloys

S. aureus was resuscitated on nutrient agar. Absorbance values of overnight grown culture was measured and adjusted to 0.5 McFarland unit. Initial concentration of microbial culture was 10^6 colonies. Control group, as received CoCrMo alloy and (SF/HA complex)$_{14}$, (SF/HA LBL)$_7$, (SF/HA complex + Levofloxacin)$_{14}$, (SF/HA LBL + Levofloxacin)$_7$ films on CoCrMo alloys at pH 3.5 were immersed in nutrient broth and *S. aureus* was inoculated. After 24 hour incubation at 37°C and 70 rpm, microbial suspension was diluted serially and plated on nutrient agar to count colony forming units. Colonies formed was counted by naked eye observation.

2.3 Characterization Techniques

2.3.1 ATR-FTIR analysis

Attenuated Total Reflectance–Fourier Transform Infrared (ATR-FTIR) spectroscopy was utilized to obtain knowledge about functional groups present in a material. The range of the wavenumber used in this research was between 3600 and 800 cm^{-1}. Infrared spectra of the as received CoCrMo alloy and prepared films on CoCrMo alloys were obtained by using a Digilab Excalibur Series FTIR spectrometer.

2.3.2 XRD analysis

Phase structures and crystalline forms of the films were investigated by X-ray diffraction (XRD) analysis. Philips X'Pert Pro diffractometer was used in this study. The operating conditions were 45 kV and 40 mA. Cu K_{α}, radiation, λ= 0.154 nm. Samples were scanned for diffraction angles $2\theta^{\circ} = 20\text{-}120^{\circ}$.

2.3.3 SEM analysis

Scanning Electron Microscopy (SEM) images were taken by Philips SFEG 30S and FEI Qanta 250 FEG instruments. SEM was used for defining the morphology of the materials before and after adsorption.

2.3.4 AFM analysis

Atomic Force Microscopy (AFM) surface characterization was operated in tapping mode using commercial Scanning Probe Microscopy instrument (Solver Pro 7 from MNT-MDT, Russia).

3. RESULTS AND DISCUSSION

3.1 ATR-FTIR Results

ATR-FTIR spectroscopy was used to identify the features of six, ten and fourteen layer films on CoCrMo alloys and as received CoCrMo alloy. IR (Infrared) spectra in the 1800-800 cm^{-1} region of control can be a dactylogram of multilayer films. In this range, IR spectrum includes different bands associated with various structural and chemical properties of the films. On the other hand, to observe the hydrogen bonds in the multilayer films, second graph was drawn in the 3600-1800 cm^{-1} range for fourteen layers films on CoCrMo alloy. This section is mainly divided into five parts: ATR-FTIR results of 1) as received CoCrMo alloy, 2) silk fibroin films on CoCrMo alloys, 3) (SF/HA complex) films on CoCrMo alloys, 4) (SF/HA LBL) films on CoCrMo alloys and 5) levofloxacin loaded SF/HA complex and LBL films on CoCrMo alloys.

Silkworm SF from *B. mori* is formed mainly Gly and Ala repetitions that dominate the construction. SF chain occurs two main polypeptide sequences, crystalline and less ordered blocks that consecutive regularly. The main sequence of the crystalline section is of –(Ala-Gly)$_n$- that accepts a β-sheet structure (silk II conformation), but the less ordered sections include additional amino acids, especially valine, acidic and tyrosine and also basic amino acids (Bini, Knight et al. 2004, Wang, Kim et al. 2005). The primary distinctions locate in the position of absorption bands of amide I, amide II and amide III projecting the various ratio among intra- and inter-molecular hydrogen bonds (Cilurzo, Gennari et al. 2011). In the literature, amide I (-CO- and –CN- stretching) appeared to be in the area of 1655-1660 cm^{-1}, amide II (-NH- bending) in the area of 1531-1542 cm^{-1} and amide III (-CN- stretching) at 1230 cm^{-1} are based to silk I (random coil) structure. In other respects, amide I appeared to be in the area of 1620-1630 cm^{-1}, amide II in the area of 1515-1530 cm^{-1} and amide III at 1231-1260 cm^{-1} are based to silk II (β-sheet structure) (Wang, Li et al. 1998, Freddi, Tsukada et al. 1999, Ayutsede, Gandhi et al. 2005).

Table 3.1 below also showed characteristic IR absorptions for silk I and silk II conformations. Silk II is an antiparallel β-sheet in which protein chains are aligned and neighboring series are linked with H-bonds between carbonyl and amine functional groups (Wang, Kim et al. 2005). It is known that silk II conformation (β-sheet conformation) occured even without methanol treatment. As SF-based matters are generally treated with methanol, a conformation transition is stimulated from silk I to silk II to make them insoluble and to increase mechanical characteristics (Chen, Shao et al. 2001, Chen, Shao et al. 2007, Chen, Knight et al. 2009, Ling, Qi et al. 2011). On the contrary, treating the aqueous multilayer films without methanol represented in partial desorption of the SF molecules, causing in the lesser deposition rates. The occurrence of the silk II conformation may be owing to the N_2 (gas) drying operation which may have dehydrated the structure, causing the silk II formation (Wang, Kim et al. 2005). In the literature, it was known that HA does not stimulate folding of SF into a silk II structure but HA can improve or activate this system when treated with methanol (Garcia-Fuentes, Giger et al. 2008). The improvement of silk II conformation examined for SF/HA matrices related with increased mechanical features: mixed matrices had better compressive moduli and better breaking strengths than pure SF matrices.

Table 3.1 : Characteristic IR absorptions for silk I and silk II conformations.

Conformation of Silk	**Amide I** (-CO- and –CN-stretching)	**Amide II** (-NH-bending)	**Amide III** (-CN-stretching)
Silk I (random coil)	1655-1660 cm^{-1}	1531-1542 cm^{-1}	1230 cm^{-1}
Silk II (β-sheet)	1620-1630 cm^{-1}	1515-1530 cm^{-1}	1231-1260 cm^{-1}

Table 3.2 below represented shortly principal IR absorptions for certain functional groups in multilayer films on CoCrMo alloys. It shows characteristic absorption bands in the regions of 1900-1500 cm^{-1} (carbonyl groups; C=O stretch), 1760-1690 cm^{-1} (carboxylic acids; C=O stretch), 1550-1475 cm^{-1} (nitro groups; N-O asymmetric stretch), 1470-1415 cm^{-1} (alkanes; C-H bend), 1400-1300 cm^{-1} (nitro groups; N=O bend), 1370-1350 cm^{-1} (alkanes; C-H rock), 1320-1000 cm^{-1} (alcohols, carboxylic acids, esters and ethers; C-O stretch), 1000-650 cm^{-1} (alkenes; =C-H bend), 950-910 cm^{-1} (carboxylic acids; O-H bend) and 910-665 (1°, 2° amines; N-H wag).

Second graphs were drawn for all fourteen layer films on CoCrMo alloys in the range of 3600-1800 cm^{-1}. Table 3.2 also shows characteristic absorption bands in the regions of 3500-3200 cm^{-1} (alcohols, phenols; O-H stretch, H-bonded), 3400-3250 cm^{-1} (1°, 2° amines, amides; N-H stretch) and 3300-2500 cm^{-1} (carboxylic acids; O-H stretch).

Table 3.2 : IR absorptions for certain functional groups in multilayer films on CoCrMo alloys, adapted from (Boulder).

Absorption Ranges (cm^{-1})	Type of Vibration	Functional Group Names
3500-3200	O-H stretch, H-bonded	alcohols, phenols
3400-3250	N-H stretch	1°, 2° amines, amides
3300-2500	O-H stretch	carboxylic acids
1900-1500	C=O stretch	carbonyl group
1760-1690	C=O stretch	carboxylic acids
1550-1475	N-O asymmetric stretch	nitro groups
1470-1415	C-H bend	alkanes
1400-1300	N=O bend	nitro groups
1370-1350	C-H rock	alkanes
1320-1000	C-O stretch	alcohols, carboxylic acids, esters and ethers
1000-650	=C-H bend	alkenes
950-910	O-H bend	carboxylic acids
910-665	N-H wag	1°, 2° amines

3.1.1 ATR-FTIR results of as received CoCrMo alloy

ATR-FTIR graph of as received CoCrMo alloy was shown in Figure 3.1. Before the ATR-FTIR analysis, as received CoCrMo alloy was washed with ethanol. For this reason, carboxylic acids and nitro compounds peaks were dominant on the surface of as received CoCrMo alloy.

The band at 1700 cm^{-1} in as received CoCrMo alloy spectra was attributed to the carboxylic acids (C=O stretch). Nitro compounds (N-O asymmetric stretch) peak was observed at 1505 cm^{-1}. Besides that, the as received CoCrMo alloys showed characteristic peaks at 1300 cm^{-1}, 1215 cm^{-1} and 1045 cm^{-1} which were based to the C-O stretch.

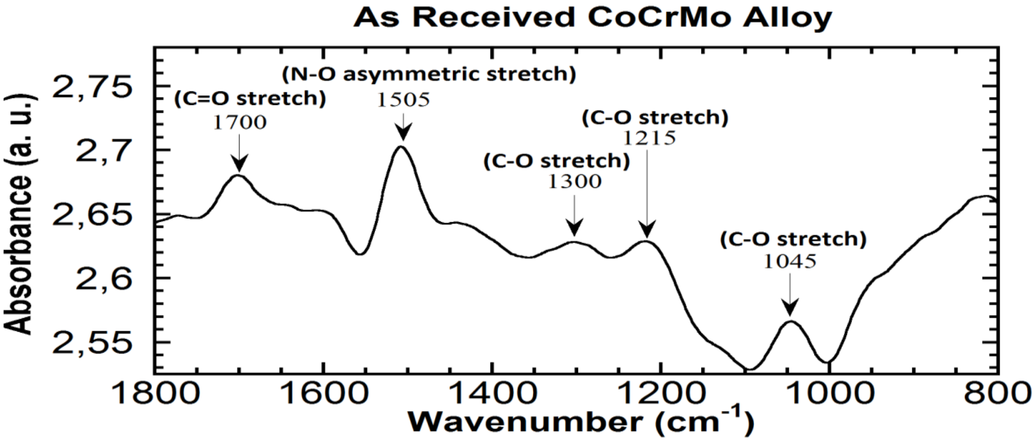

Figure 3.1 : ATR-FTIR spectra of as received CoCrMo alloy.

3.1.2 ATR-FTIR results of silk fibroin films on CoCrMo alloys

3.1.2.1 ATR-FTIR results of SF films at pH 3.0

ATR-FTIR graphs for six, ten and fourteen layers of positively charged SF films on CoCrMo alloys at pH 3.0 were showed in Figures of 3.2, 3.3, 3.4 and 3.5, respectively. Included in the Figure 3.5 is the result of 1800-3600 cm^{-1} which was plotted to reveal the hydrogen bonding structures.

ATR-FTIR graphs for SF_6 and SF_{10} films on CoCrMo alloys were showed in Figures of 3.2 and 3.3, respectively. These films were presented absorption bands in the region of 1620-1630 cm^{-1} (amide I; -CO- and –CN- stretching), at 1530 cm^{-1} (amide II; -NH- bending) and at 1240 cm^{-1} (amide III; -CN- stretching), corresponding to the silk II conformation (β-sheet). In these coatings, dominant β-sheet conformation occurred thanks to methanol treatment for each washing steps. Besides that, C-O stretch and N-H wag were observed in Figures of 3.2 and 3.3.

ATR-FTIR graph for SF_{14} film on CoCrMo alloy was showed in Figure 3.4. Absorption bands were presented in this graph at 1630 cm^{-1} (amide I; -CO- and –CN- stretching) and 1240 cm^{-1} (amide III; -CN- stretching), corresponding to the silk II conformation. Other absorption band was seen at 1542 cm^{-1} (amide II; -NH- bending), which were characteristic of the silk I structure. It was shown that silk I and silk II conformations were seen simultaneously in SF_{14} film on CoCrMo alloy at pH 3.0. Besides that, C-O stretch was seen for two different absorption peaks at 1125 cm^{-1} and 1010 cm^{-1}.

Second ATR-FTIR graph for SF_{14} film on CoCrMo alloy was also showed in region of 3600 cm^{-1} to 1800 cm^{-1} in Figure 3.5. The absorption bands at 3400 cm^{-1} and 2585 cm^{-1} were related to O-H stretch and the band at 3285 cm^{-1} was related to N-H stretch. Thus, these spectral varieties were generally attributed to intra- or intermolecular H-bonding (Park, Lee et al. 1999, Dai, Li et al. 2002).

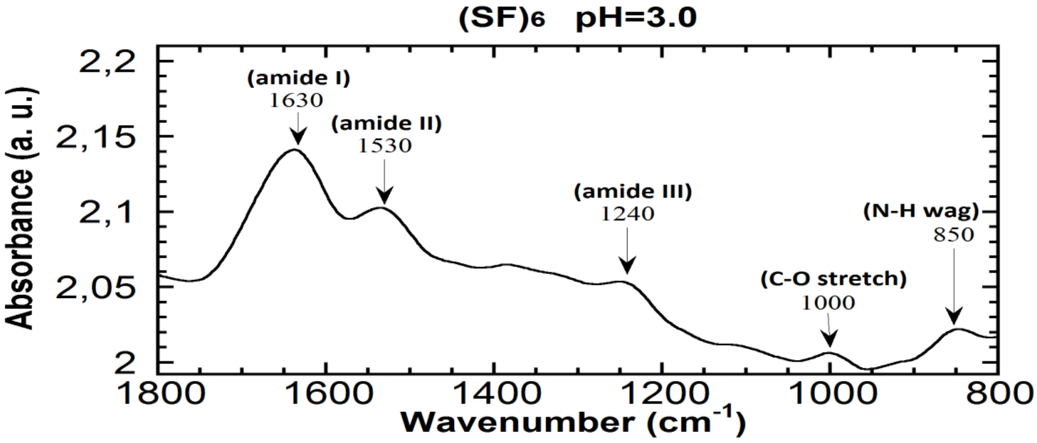

Figure 3.2 : ATR-FTIR spectra of $(SF)_6$ on CoCrMo alloy at pH 3.0.

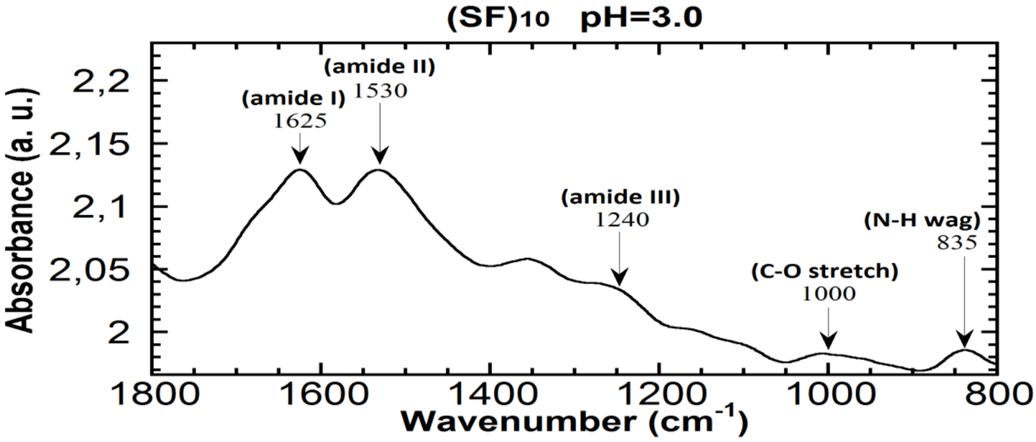

Figure 3.3 : ATR-FTIR spectra of $(SF)_{10}$ on CoCrMo alloy at pH 3.0.

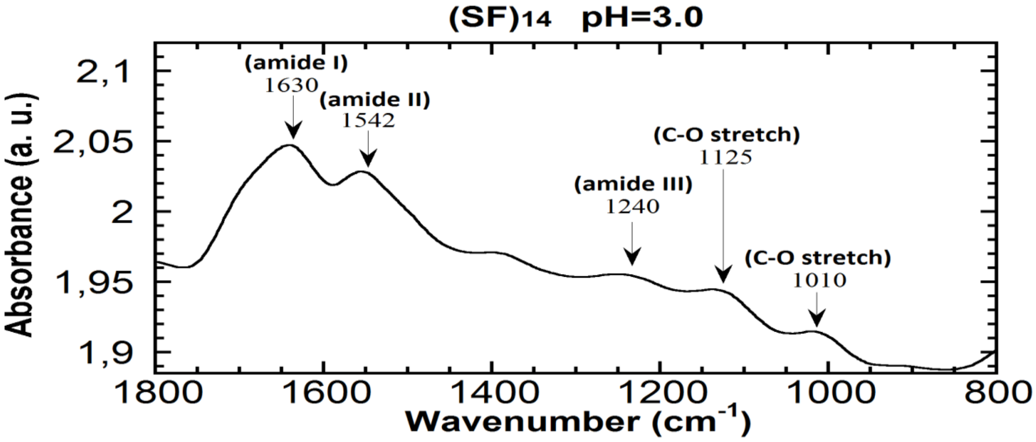

Figure 3.4 : ATR-FTIR spectra of $(SF)_{14}$ on CoCrMo alloy at pH 3.0.

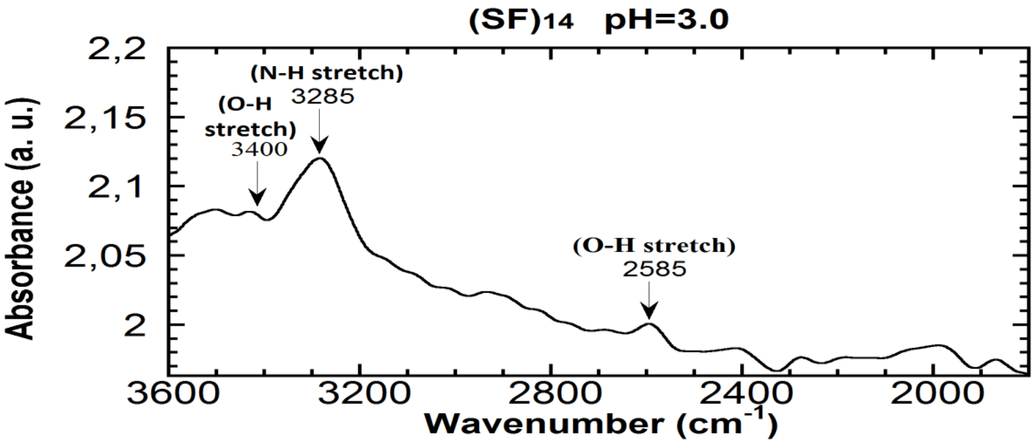

Figure 3.5 : Second ATR-FTIR spectra of $(SF)_{14}$ on CoCrMo alloy at pH 3.0.

3.1.2.2 ATR-FTIR results of SF films at pH 3.5

Six, ten and fourteen layers of positively charged SF films on CoCrMo alloys were analyzed at pH 3.5 by ATR-FTIR spectroscopy in Figures of 3.6, 3.7, 3.8 and 3.9, respectively. Absorption values of amide I (-CO- and –CN- stretching), amide II (-NH- bending) and amide III (-CN- stretching) were attributed to both silk I and silk II conformations for SF_6, SF_{10}, SF_{14} films on CoCrMo alloys in Figures of 3.6, 3.7 and 3.8. Besides that, O-H stretch and N-H stretch were viewed distinctly on the second graph of SF_{14} film in region of 3600 cm^{-1} to 1800 cm^{-1} in Figure 3.9. These spectral varieties were generally attributed to intra- or intermolecular H-bonding.

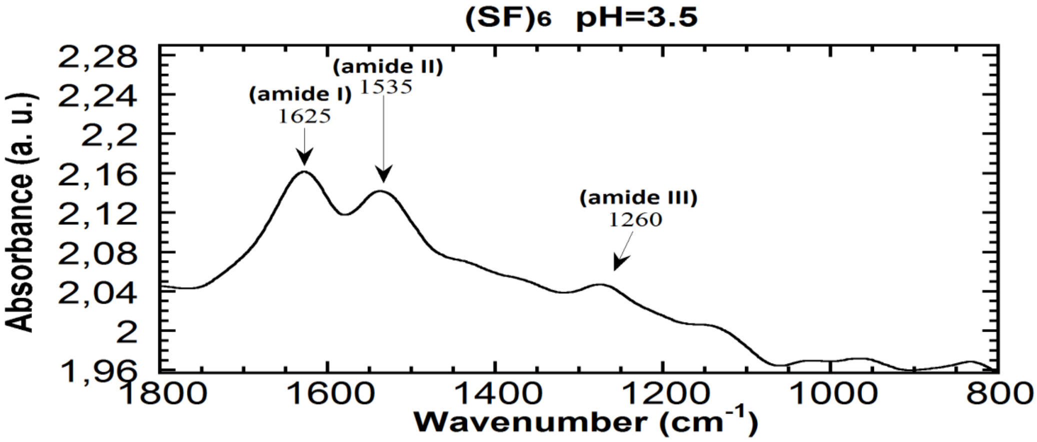

Figure 3.6 : ATR-FTIR spectra of $(SF)_6$ on CoCrMo alloy at pH 3.5.

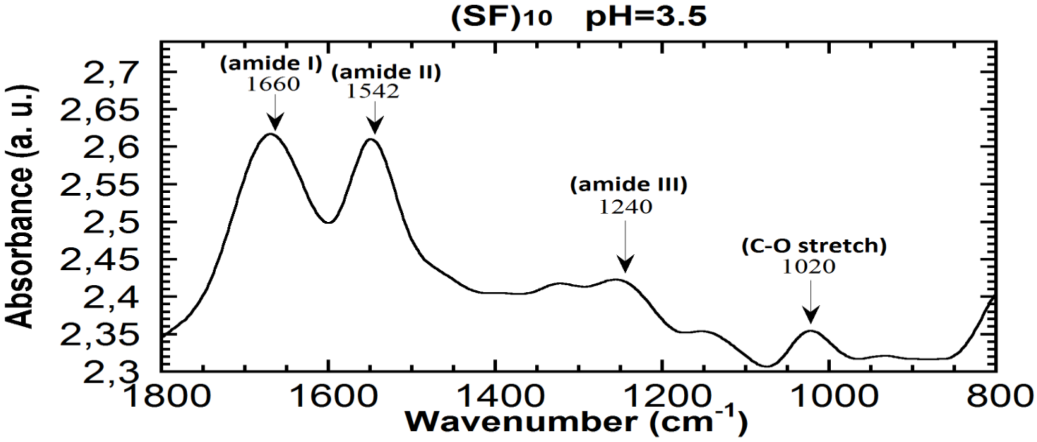

Figure 3.7 : ATR-FTIR spectra of $(SF)_{10}$ on CoCrMo alloy at pH 3.5.

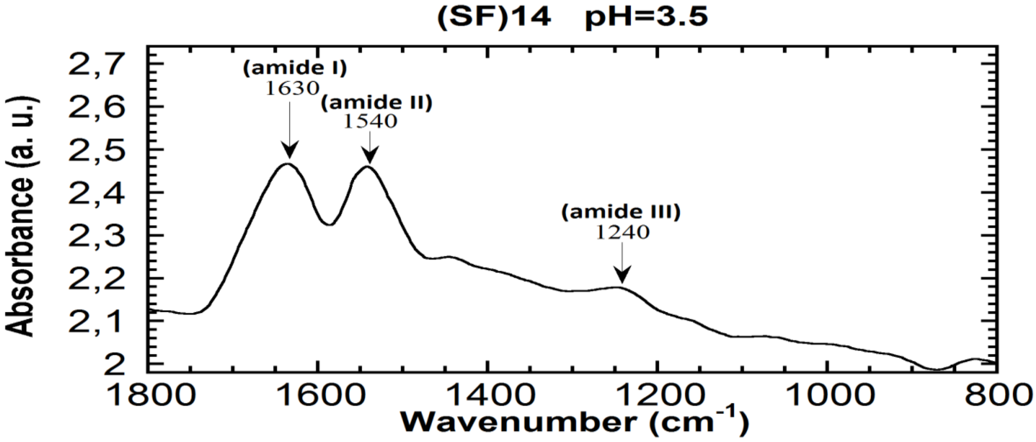

Figure 3.8 : ATR-FTIR spectra of $(SF)_{14}$ on CoCrMo alloy at pH 3.5.

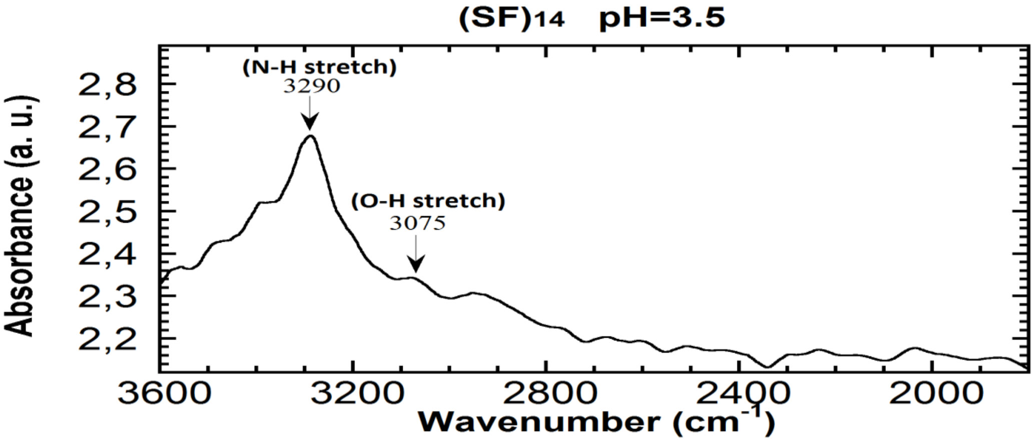

Figure 3.9 : Second ATR-FTIR spectra of $(SF)_{14}$ on CoCrMo alloy at pH 3.5.

3.1.2.3 ATR-FTIR results of SF films at pH 5.5

Six, ten and fourteen layers of negatively charged SF films on CoCrMo alloys were characterized at pH 5.5 with ATR-FTIR spectroscopy in Figures of 3.10, 3.11, 3.12 and 3.13, respectively. Absorption values of amide II (-NH- bending) and amide III (-CN- stretching) were attributed to both silk I and silk II conformations for SF_6 film on CoCrMo alloy in Figure 3.10. But amide I (-CO- and –CN- stretching) region was not observed for this multilayer film. Besides that, C-H bend, N=O bend, C-O stretch, O-H bend and N-H wag were observed for SF_6 film on CoCrMo alloy.

Absorption values of amide I (-CO- and –CN- stretching) and amide II (-NH- bending) were attributed to silk I conformation for SF_{10} film on CoCrMo alloy in Figure 3.11. But amide III (-CN- stretching) region was not seen. In addition to, C-H bend, N=O bend, C-O stretch, O-H bend and N-H wag were determined in Figure 3.11.

The band position for SF_{14} film on CoCrMo alloy in the amide I region at 1630 cm^{-1} represented a silk II structure because C=O groups in β-sheets were included in more in Figure 3.12. A parallel investigation can be related in the amide II region at 1530 cm^{-1} on account of the silk I conformation was shifted for the silk II structure of SF_{14} film. The band in the amide III region at 1240 cm^{-1} was attributed to the crystalline phase (silk II conformation) for SF_{14} film on CoCrMo alloy. In addition to, C-O stretch and N-H wag were identified in Figure 3.12.

Second second graph was drawn for SF_{14} film on CoCrMo alloy in region of 3600 cm^{-1} to 1800 cm^{-1} in Figure 3.13. O-H stretch and N-H stretch were seen clearly.

These spectral varieties were generally attributed to intra- or intermolecular H-bonding.

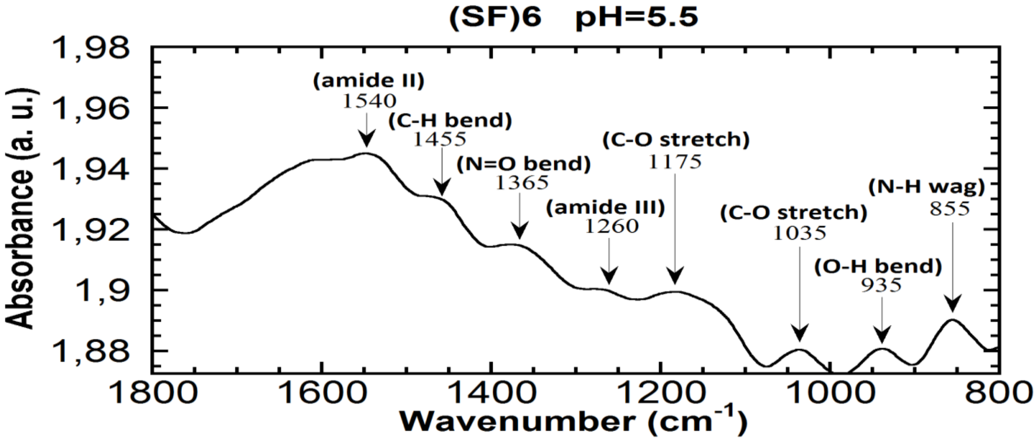

Figure 3.10 : ATR-FTIR spectra of $(SF)_6$ on CoCrMo alloy at pH 5.5.

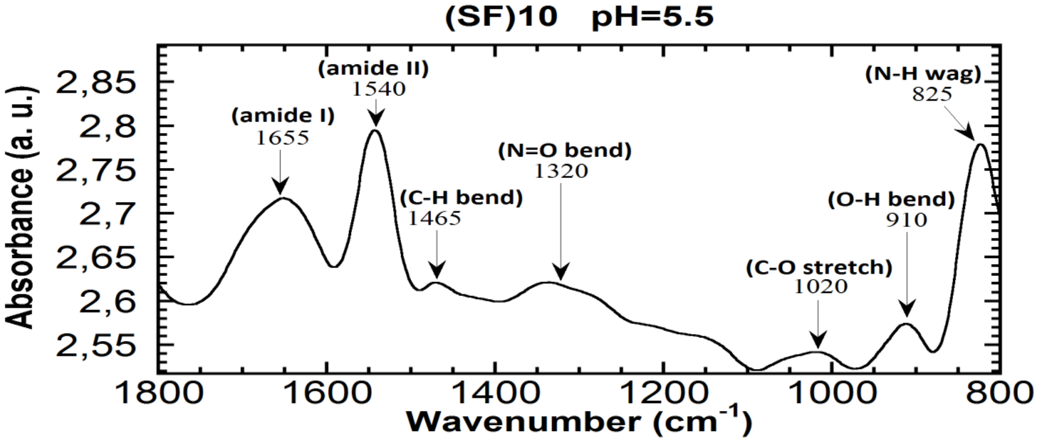

Figure 3.11 : ATR-FTIR spectra of $(SF)_{10}$ on CoCrMo alloy at pH 5.5.

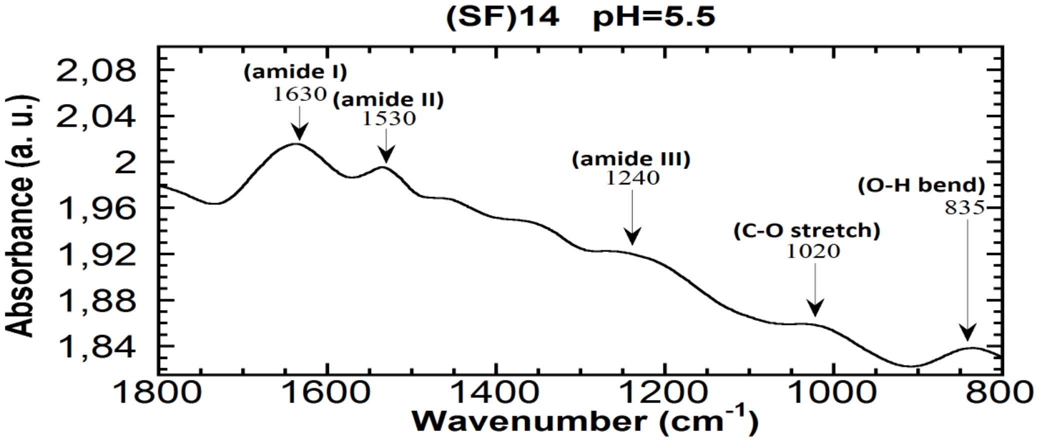

Figure 3.12 : ATR-FTIR spectra of $(SF)_{14}$ on CoCrMo alloy at pH 5.5.

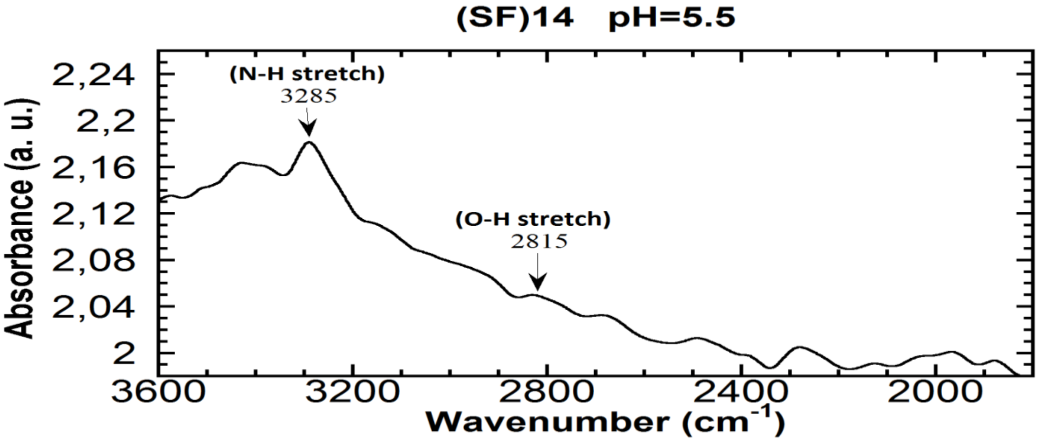

Figure 3.13 : Second ATR-FTIR spectra of $(SF)_{14}$ on CoCrMo alloy at pH 5.5.

3.1.3 ATR-FTIR results of (SF/HA complex) films on CoCrMo alloys

3.1.3.1 ATR-FTIR results of (SF/HA complex) films at pH 3.0

Six, ten and fourteen layers of (SF/HA complex) films on CoCrMo alloys were analyzed at pH 3.0 by means of ATR-FTIR spectroscopy in Figures of 3.14, 3.15, 3.16 and 3.17, respectively.

The IR spectrum of the $(SF/HA\ complex)_6$ film on CoCrMo alloy in Figure 3.14 represented more defined absorption bands of amide I and III, attributed to the β-sheet structure. However, there was no absorption band in the region of amide II. A peak around 1450 cm^{-1} indicated the existence of C-H bend. In addition to, C-O stretch and O-H bend were observed for $(SF/HA\ complex)_6$ film on CoCrMo alloy in Figure 3.14.

As observed for $(SF/HA\ complex)_6$ film, amide I and amide III regions were attributed to silk II conformation for $(SF/HA\ complex)_{10}$ film on CoCrMo alloy in Figure 3.15. Amide II region was not seen. Besides that, C-H bend, C-O stretch and N-H wag were observed in Figure 3.15.

ATR-FTIR graph for $(SF/HA\ complex)_{14}$ film on CoCrMo alloy was shown in Figure 3.16. This multilayer film presented absorption bands at 1655 cm^{-1} (amide I) and 1540 cm^{-1} (amide II), corresponding to the silk I conformation. Another absorption band was seen at 1255 cm^{-1} (amide III), which were characteristic of the silk II structure. It was demonstrated that random coil and β-sheet structures were presented simultaneously in $(SF/HA\ complex)_{14}$ film on CoCrMo alloy. C-O stretch was also observed in Figure 3.16.

Second graph was shown for (SF/HA complex)$_{14}$ film on CoCrMo alloy in region of 3600 cm^{-1} to 1800 cm^{-1} in Figure 3.17. O-H stretch and N-H stretch were seen clearly. These spectral varieties were generally attributed to intra- or intermolecular H-bonding.

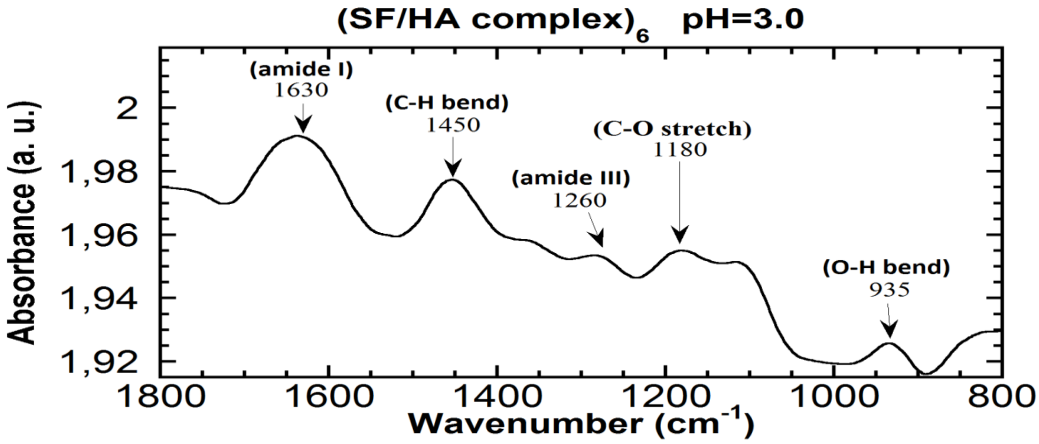

Figure 3.14 : ATR-FTIR spectra of (SF/HA complex)$_6$ on CoCrMo alloy at pH 3.0.

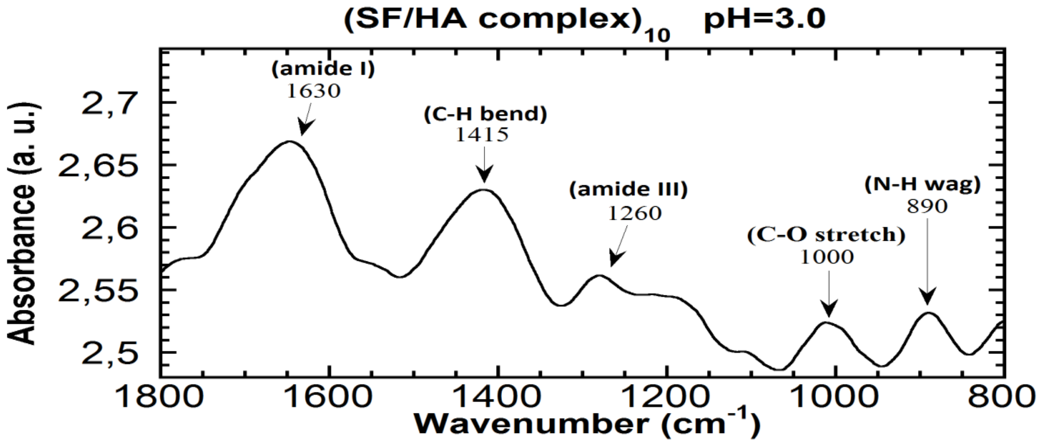

Figure 3.15 : ATR-FTIR spectra of (SF/HA complex)$_{10}$ on CoCrMo alloy at pH 3.0.

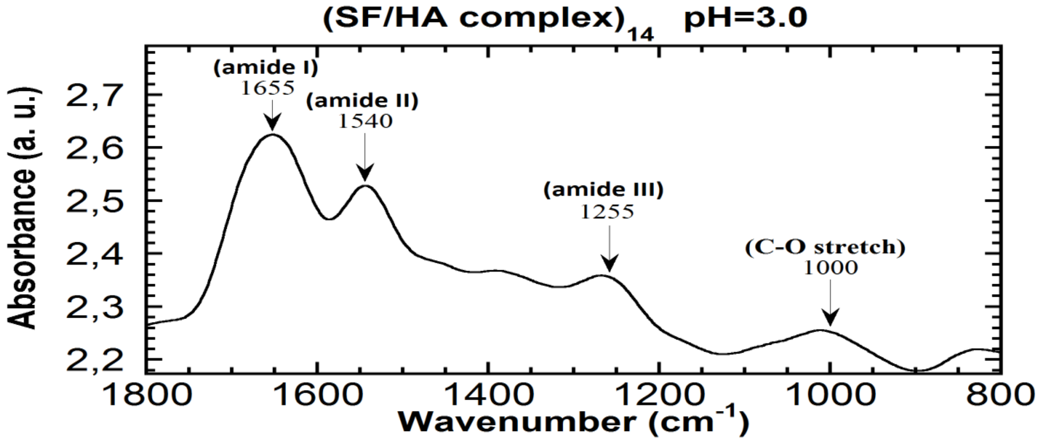

Figure 3.16 : ATR-FTIR spectra of (SF/HA complex)$_{14}$ on CoCrMo alloy at pH 3.0.

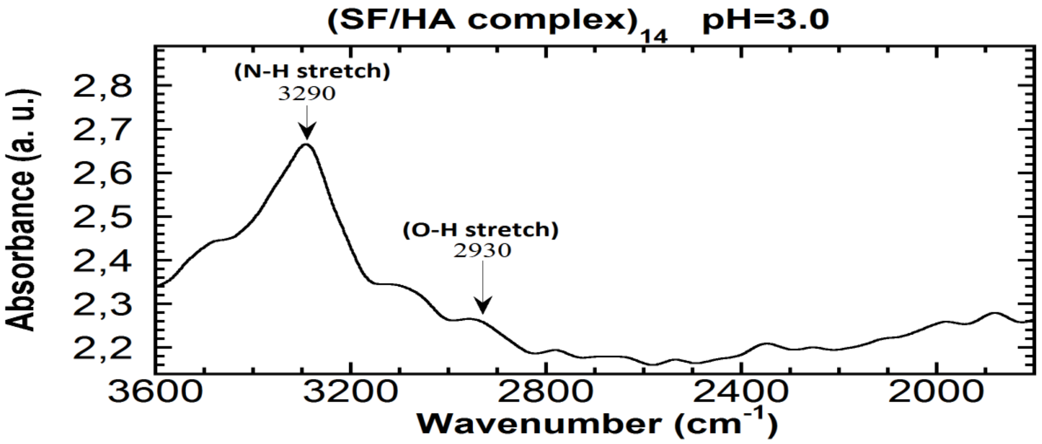

Figure 3.17 : Second ATR-FTIR spectra of (SF/HA complex)$_{14}$ on CoCrMo alloy at pH 3.0.

3.1.3.2 ATR-FTIR results of (SF/HA complex) films at pH 3.5

Six, ten and fourteen layers of (SF/HA complex) films on CoCrMo alloys were analyzed at pH 3.5 by means of ATR-FTIR spectroscopy in Figures of 3.18, 3.19, 3.20 and 3.21, respectively. SF was positively charged at pH 3.5 whereas HA was negatively charged at this pH. All samples were treated with methanol. Amide I, II and III were attributed to -CO- and –CN- stretching, -NH- bending and -CN- stretching, respectively. ATR-FTIR analysis of (SF/HA complex)$_6$ film on CoCrMo alloy in Figure 3.18 clearly showed two peaks at 1630 (amide I) cm^{-1} and 1240 cm^{-1} (amide III). Therefore, the amide I and amide III were assigned primarily to the silk II structure for this complex film. The amide II region of this multilayer film had a strong absorption at 1540 cm^{-1}, demonstrating that SF was in random coil conformation. It was indicated that random coil and β-sheet structures were presented simultaneously in (SF/HA complex)$_6$ film on CoCrMo alloy. Besides that, this multilayer film showed characteristic peaks at 1415 cm^{-1} (C-H bend), 1335 cm^{-1} (N=O bend), 1165 cm^{-1} (C-O stretch), 920 cm^{-1} (O-H bend) and 825 cm^{-1} (N-H wag) in Figure 3.18.

ATR-FTIR graph for (SF/HA complex)$_{10}$ film on CoCrMo alloy was shown in Figure 3.19. This multilayer film presented absorption bands at 1660 cm^{-1} (amide I) and 1542 cm^{-1} (amide II), corresponding to the silk I conformation. Other absorption band was seen at 1240 cm^{-1} (amide III), which was characteristic of the silk II structure. It was demonstrated that silk I and silk II conformations were indicated simultaneously in (SF/HA complex)$_{10}$ film on CoCrMo alloy. In addition to, this multilayer film showed characteristic peaks at 1400 cm^{-1} (N=O bend), 1125 cm^{-1} and 1010 cm^{-1} (C-O stretch), 840 cm^{-1} (N-H wag) in Figure 3.19.

ATR-FTIR spectra of (SF/HA complex)$_{14}$ film on CoCrMo alloy was shown in Figure 3.20. This multilayer film showed absorption bands at 1530 cm^{-1} (amide II) and 1260 cm^{-1} (amide III), assigned to the silk II structure. However, amide I region was not clear. Besides that, this multilayer film showed characteristic peaks at 1690 cm^{-1} (C=O stretch), 1460 cm^{-1} (C-H bend), 1350 cm^{-1} (N=O bend), 1180 cm^{-}1, 1055 cm^{-1} (C-O stretch), 945 cm^{-1} (O-H bend) and 845 cm^{-1} (N-H wag).

Second graph was drawn for (SF/HA complex)$_{14}$ film on CoCrMo alloy in region of 3600 cm^{-1} to 1800 cm^{-1} in Figure 3.21. C=O stretch was observed at 1900 cm^{-1}. Besides that, O-H stretch and N-H stretch were seen clearly. These spectral varieties were generally attributed to intra- or intermolecular H-bonding. Strong peak was seen at 2355 cm^{-1}. CO_2 was supposed to create a peak at this region due to O=C=O of CO_2 present in air.

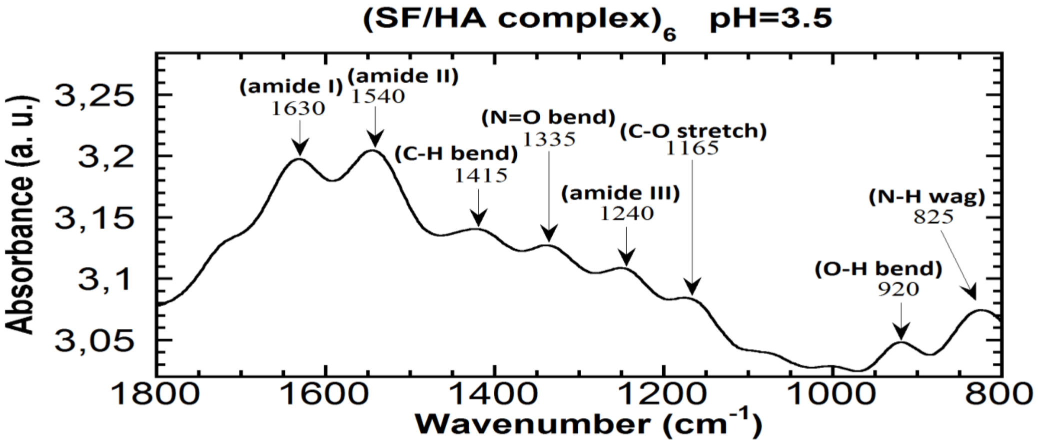

Figure 3.18 : ATR-FTIR spectra of (SF/HA complex)$_6$ on CoCrMo alloy at pH 3.5.

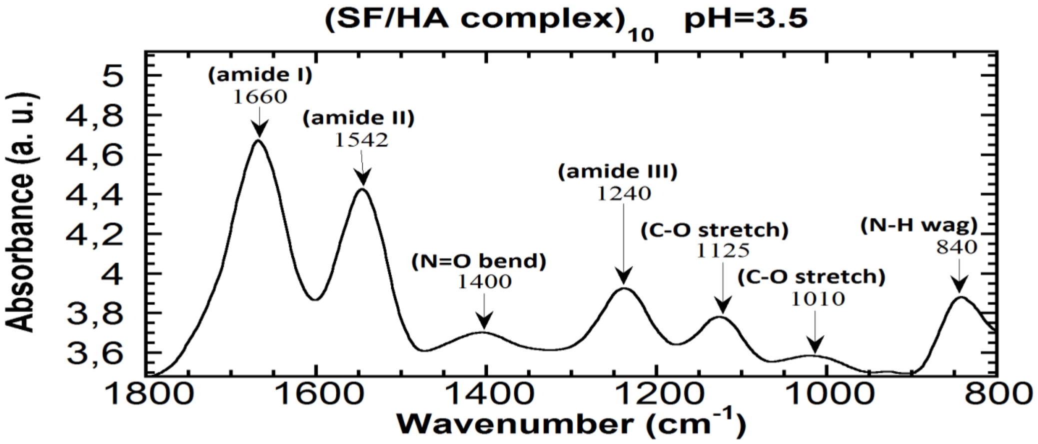

Figure 3.19 : ATR-FTIR spectra of (SF/HA complex)$_{10}$ on CoCrMo alloy at pH 3.5.

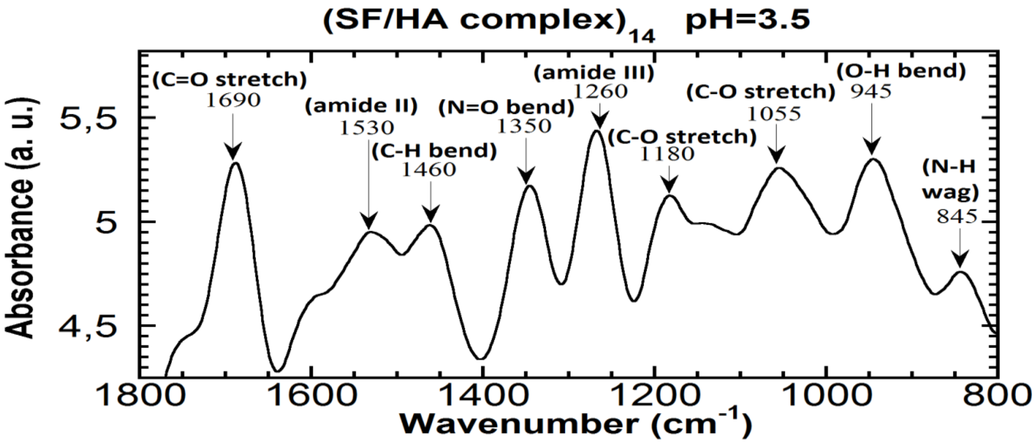

Figure 3.20 : ATR-FTIR spectra of (SF/HA complex)$_{14}$ on CoCrMo alloy at pH 3.5.

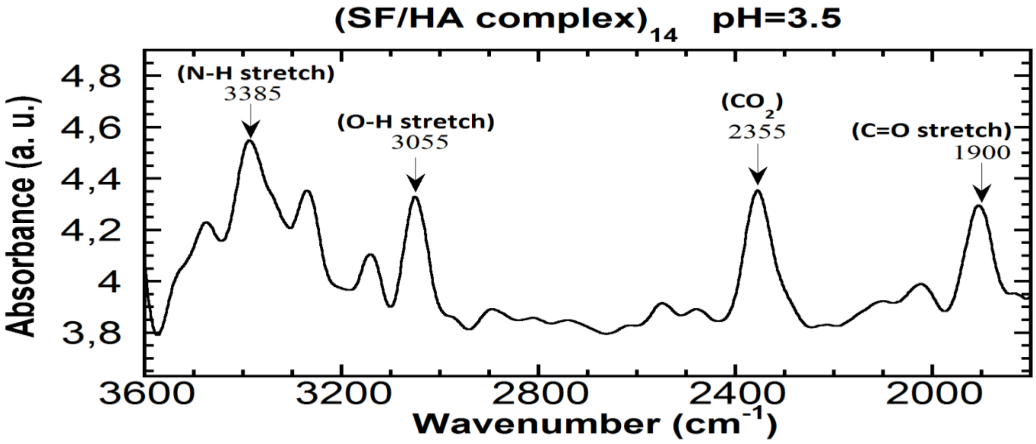

Figure 3.21 : Second ATR-FTIR spectra of (SF/HA complex)$_{14}$ on CoCrMo alloy at pH 3.5.

3.1.3.3 ATR-FTIR results of (SF/HA complex) films at pH 5.5

Six, ten and fourteen layers of (SF/HA complex) films on CoCrMo alloys were characterized at pH 5.5 by ATR-FTIR spectroscopy in Figures of 3.22, 3.23, 3.24 and 3.25, respectively. SF and HA molecules both were negatively charged at this pH. All samples were treated with methanol.

ATR-FTIR spectrum of the (SF/HA complex)$_6$ film on CoCrMo alloy was shown in Figure 3.22. Absorption values of amide II and amide III were attributed to silk I conformation for this multilayer complex film. But amide I region was not clear. In addition to C=O stretch, N=O bend, C-O stretch, =C-H bend and N-H wag were observed respectively in Figure 3.22.

The band in the amide III region at 1260 cm^{-1} was attributed to the crystalline phase (silk II conformation) for (SF/HA complex)$_{10}$ film on CoCrMo alloy in Figure 3.23.

However, amide I and amide II regions were not clear. Besides that, C=O stretch, N=O bend, C-O stretch and O-H bend were identified respectively in Figure 3.23.

The band position for (SF/HA complex)$_{14}$ film on CoCrMo alloy in the amide I region at 1660 cm^{1} and in the amide II region at 1542 cm^{-1} represented a silk I structure in Figure 3.24. But amide III region was not observed. In addition to, C-H bend, N=O bend, C-O stretch and O-H bend were seen, respectively.

Second graph was drawn for (SF/HA complex)$_{14}$ film on CoCrMo alloy in region of 3600 cm^{-1} to 1800 cm^{-1} in Figure 3.25. O-H stretch and N-H stretch were seen clearly. These spectral varieties were generally attributed to intra- or intermolecular H-bonding.

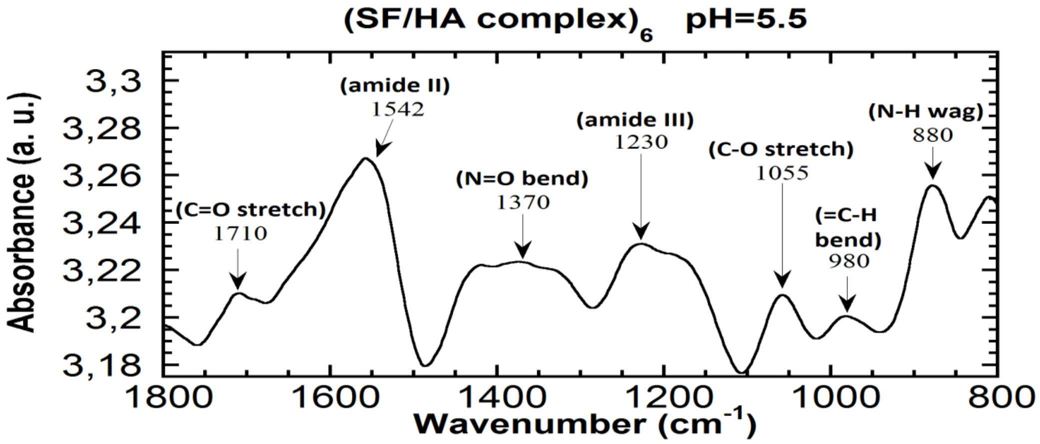

Figure 3.22 : ATR-FTIR spectra of (SF/HA complex)$_6$ on CoCrMo alloy at pH 5.5.

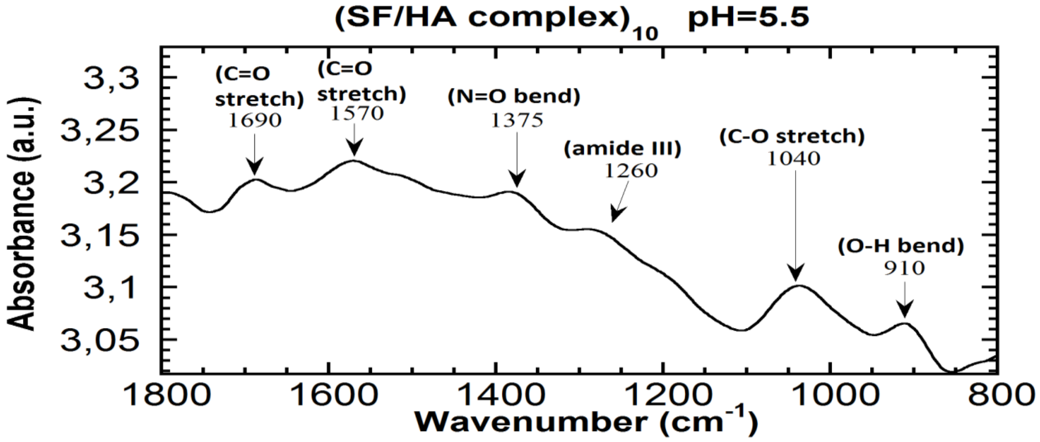

Figure 3.23 : ATR-FTIR spectra of (SF/HA complex)$_{10}$ on CoCrMo alloy at pH 5.5.

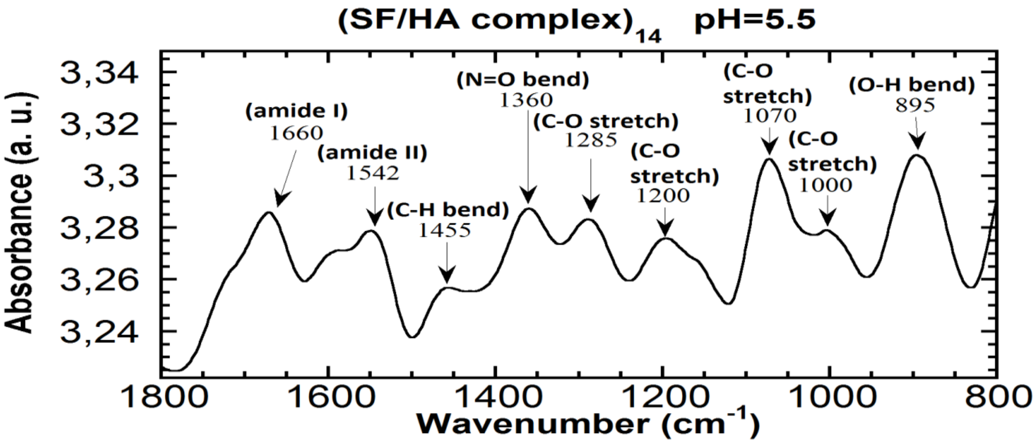

Figure 3.24 : ATR-FTIR spectra of (SF/HA complex)$_{14}$ on CoCrMo alloy at pH 5.5.

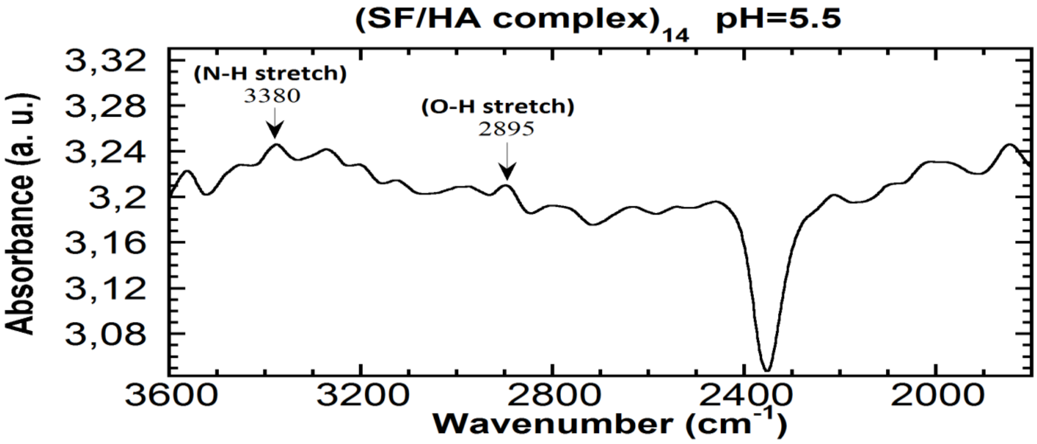

Figure 3.25 : Second ATR-FTIR spectra of (SF/HA complex)$_{14}$ on CoCrMo alloy at pH 5.5.

3.1.4 ATR-FTIR results of (SF/HA LBL) films on CoCrMo alloys

3.1.4.1 ATR-FTIR results of (SF/HA LBL) films at pH 3.0

Six, ten and fourteen layers of (SF/HA LBL) films on CoCrMo alloys were analyzed at pH 3.0 by ATR-FTIR spectroscopy in Figures of 3.26, 3.27, 3.28 and 3.29, respectively. SF was positively charged at p 3.0 whereas HA was negatively charged at this pH. All samples were treated with methanol.

The band position for (SF/HA LBL)$_3$ film on CoCrMo alloy in the amide I region at 1620 cm^{-1} represented a silk II structure because C=O groups in β-sheets were included in more in Figure 3.26. A parallel investigation can be related in the amide II region at 1520 cm^{-1} on account of the silk I conformation was shifted for the silk II structure of (SF/HA LBL)$_3$ film on CoCrMo alloy. The band in the amide III region at 1240 cm^{-1} was attributed to the crystalline phase (silk II conformation) for this multilayer film. Besides that, C=O stretch, C-H bend, C-O stretch, =C-H bend and N-H wag were observed respectively in Figure 3.26.

ATR-FTIR spectrum of the (SF/HA LBL)$_5$ film on CoCrMo alloy in Figure 3.27 represented more defined absorption band of amide I attributed to the silk I structure. Another absorption band was seen at 1240 cm^{-1} (amide III), which were characteristic of the silk II structure. However, amide II region was not seen. It was demonstrated that random coil and β-sheet structures were presented simultaneously in (SF/HA LBL)$_5$ film on CoCrMo alloy. In addition to, C-H bend, C-O stretch, =C-H bend and N-H wag were observed respectively.

ATR-FTIR graph for (SF/HA LBL)$_7$ film on CoCrMo alloy was showed in Figure 3.28. It presented absorption bands at 1542 cm^{-1} (amide II), corresponding to the silk I conformation. Other absorption band was seen at 1240 cm^{-1} (amide III), which were characteristic of the silk II structure. But amide I region was not clear. It was demonstrated that random coil and β-sheet structures were presented simultaneously in (SF/HA LBL)$_7$ film on CoCrMo alloy. Besides that, C=O stretch, N-O asymmetric stretch, N=O bend, C-O stretch, O-H bend and N-H wag were observed respectively.

Second ATR-FTIR graph for (SF/HA LBL)$_7$ film on CoCrMo alloy in region of 3600 cm^{-1} to 1800 cm^{-1} was also showed in Figure 3.29. The absorption band at 3455 cm^{-1} was related to the O-H stretch, H-bonded, the band at 3290 cm^{-1} was related to the N-H stretch and the other band at 2775 was related to the O-H stretch. Thus, these spectral varieties were generally attributed to intra- or intermolecular H-bonding. Strong peak was seen at 2335 cm^{-1}. CO_2 was supposed to create a peak at this region due to O=C=O of CO_2 present in air.

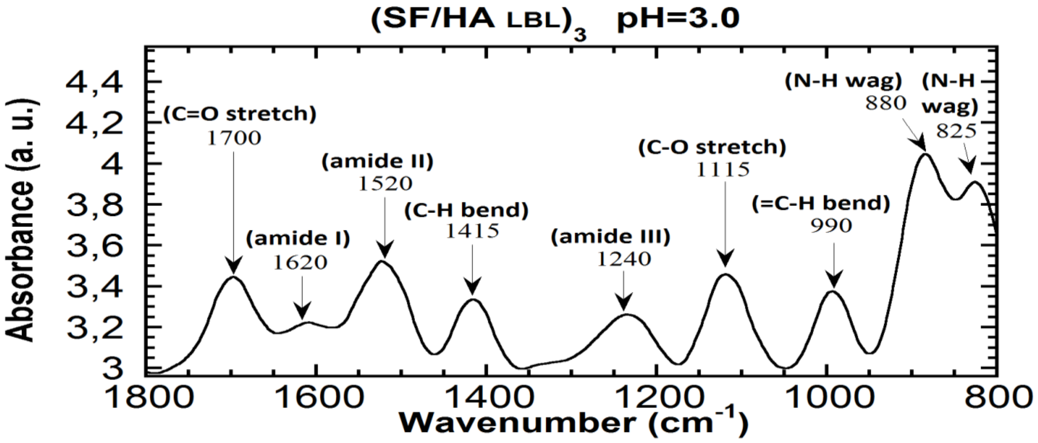

Figure 3.26 : ATR-FTIR spectra of (SF/HA LBL)$_3$ on CoCrMo alloy at pH 3.0.

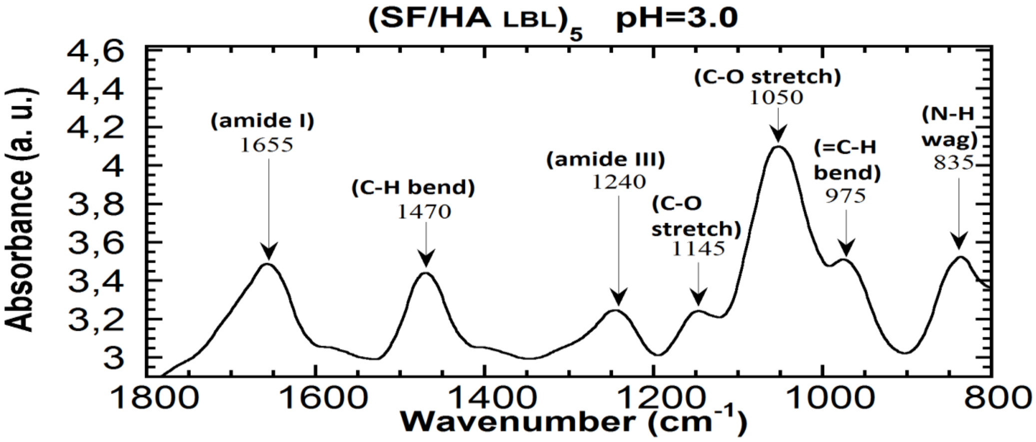

Figure 3.27 : ATR-FTIR spectra of (SF/HA LBL)$_5$ on CoCrMo alloy at pH 3.0.

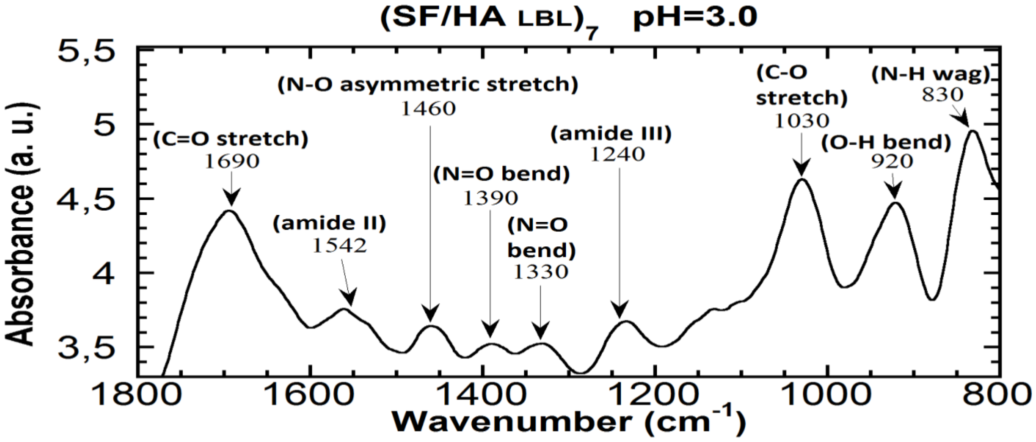

Figure 3.28 : ATR-FTIR spectra of (SF/HA LBL)$_7$ on CoCrMo alloy at pH 3.0.

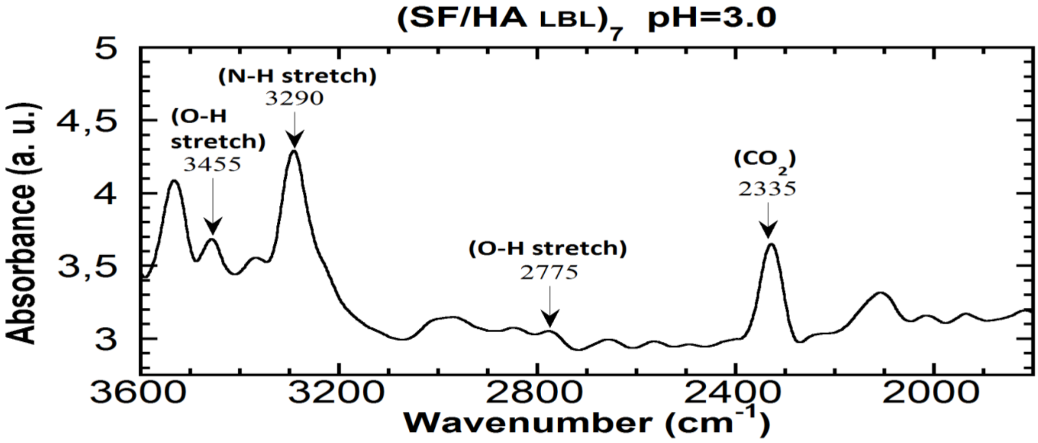

Figure 3.29 : Second ATR-FTIR spectra of (SF/HA LBL)$_7$ on CoCrMo alloy at pH 3.0.

3.1.4.2 ATR-FTIR results of (SF/HA LBL) films at pH 3.5

Six, ten and fourteen layers of (SF/HA LBL) films on CoCrMo alloys were characterized at pH 3.5 by ATR-FTIR spectroscopy in Figures of 3.30, 3.31, 3.32

and 3.33. SF molecule was positively charged at pH 3.5 whereas HA molecule was negatively charged at this pH. All samples were treated with methanol.

The band position for $(SF/HA\ LBL)_3$ film on CoCrMo alloy in the amide I region at 1630 cm^{-1} represented a silk II structure because C=O groups in β-sheets were included in more in Figure 3.30. A parallel investigation can be related in the amide II region at 1530 cm^{-1} on account of the silk I conformation was shifted for the silk II structure of $(SF/HA\ LBL)_3$ film. The band in the amide III region at 1260 cm^{-1} was attributed to the crystalline phase (silk II conformation) for this multilayer film on CoCrMo alloy. On the other hand, C-H bend, N=O bend, C-O stretch, O-H bend and N-H wag were also observed in Figure 3.30.

Absorption values of amide I and amide II were attributed to both silk I conformation for $(SF/HA\ LBL)_5$ film on CoCrMo alloy in Figure 3.31. The band in the amide III region at 1255 cm^{-1} was attributed to the crystalline phase (silk II conformation) for this multilayer film on CoCrMo alloy. It demonstrated that silk I and silk II conformations were indicated simultaneously in $(SF/HA\ LBL)_5$ film on CoCrMo alloy. In addition to, N=O bend, C-O stretch were determined in Figure 3.31.

ATR-FTIR spectra of $(SF/HA\ LBL)_7$ film on CoCrMo alloy was shown in Figure 3.32. This multilayer film showed absorption bands at 1630 cm^{-1} (amide I) and 1530 cm^{-1} (amide II), assigned to the silk II structure. The band in the amide III region at 1230 cm^{-1} was attributed to the silk I conformation for $(SF/HA\ LBL)_7$ film on CoCrMo alloy. It was demonstrated that random coil and β-sheet structures were presented simultaneously in this multilayer film. Besides that, C-H bend, C-O stretch and N-H wag were identified in Figure 3.32.

Second ATR-FTIR graph for $(SF/HA\ LBL)_7$ film on CoCrMo alloy was also showed in region of 3600 cm^{-1} to 1800 cm^{-1} in Figure 3.33. The absorption band at 3465 cm^{-1} was related to the O-H stretch, H-bonded, the band at 3315 cm^{-1} was related to the N-H stretch and the other band at 2930 was related to the O-H stretch. Thus, these spectral varieties were generally attributed to intra- or intermolecular H-bonding.

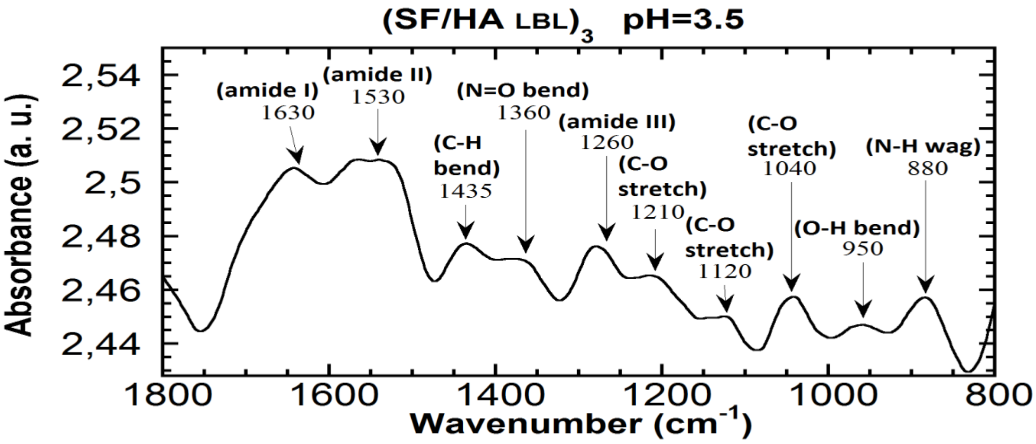

Figure 3.30 : ATR-FTIR spectra of (SF/HA LBL)$_3$ on CoCrMo alloy at pH 3.5.

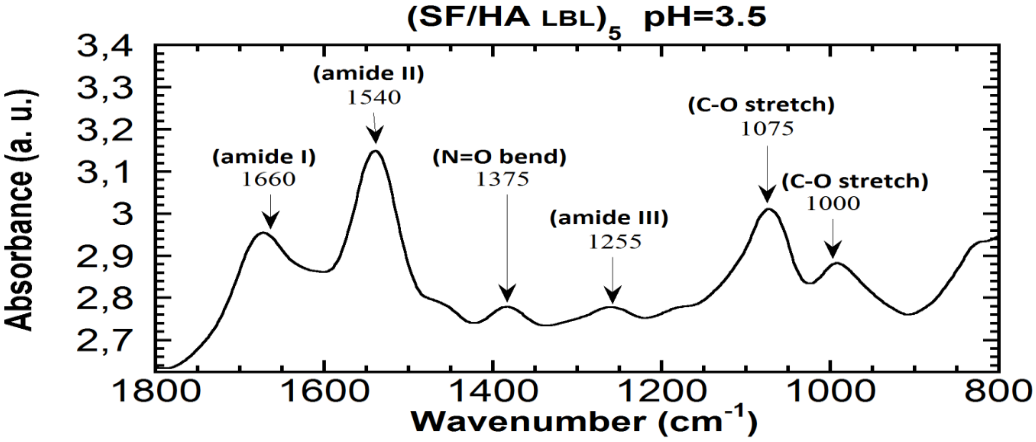

Figure 3.31 : ATR-FTIR spectra of (SF/HA LBL)$_5$ on CoCrMo alloy at pH 3.5.

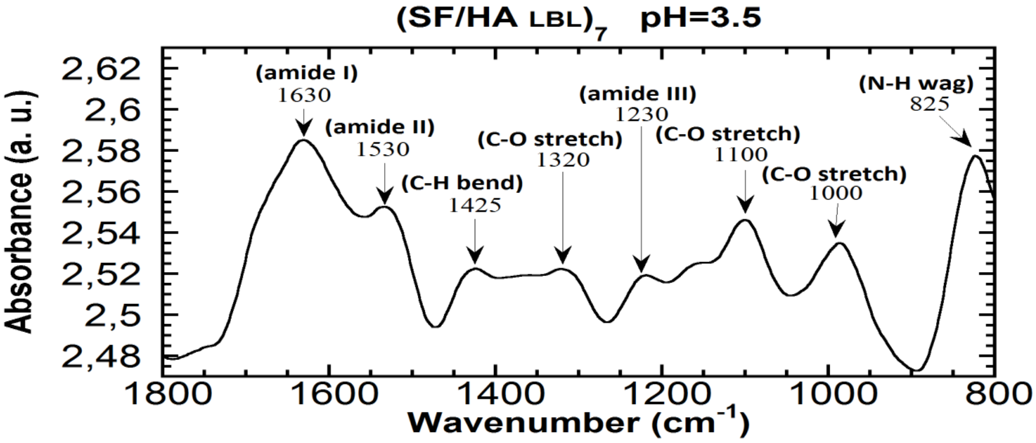

Figure 3.32 : ATR-FTIR spectra of (SF/HA LBL)$_7$ on CoCrMo alloy at pH 3.5.

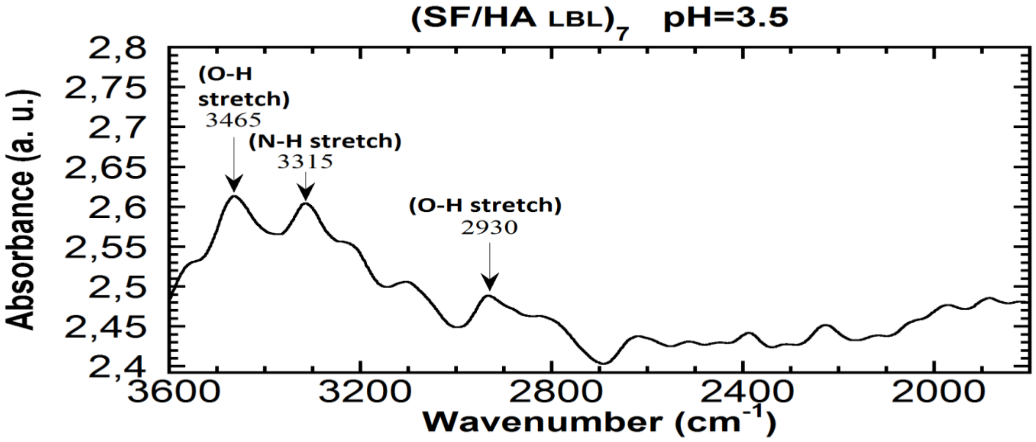

Figure 3.33 : Second ATR-FTIR spectra of (SF/HA LBL)$_7$ on CoCrMo alloy at pH 3.5.

3.1.4.3 ATR-FTIR results of (SF/HA LBL) films at pH 5.5

Six, ten and fourteen layers of (SF/HA LBL) films on CoCrMo alloys were characterized at pH 5.5 by ATR-FTIR spectroscopy in Figures of 3.34, 3.35, 3.36 and 3.37, respectively. SF and HA both were negatively charged at pH 5.5. All samples were treated with methanol.

Absorption values of amide I (-CO- and –CN- stretching) and amide III (-CN- stretching) were attributed to silk II conformation for (SF/HA LBL)$_3$ film on CoCrMo alloy in Figure 3.34. But absorption value of amide II (-NH- bending) was attributed to silk I conformation. In addition to, C=O stretch, C-H bend, N=O bend, C-O stretch, O-H bend and N-H wag were determined in Figure 3.34.

Absorption values of amide I and amide II were attributed to silk I structure for (SF/HA LBL)$_5$ film on CoCrMo alloy in Figure 3.35. However amide III region was not observed. Besides that, C=O stretch, N=O bend, C-O stretch and N-H wag were also observed for this multilayer film on CoCrMo alloy.

ATR-FTIR graph for (SF/HA LBL)$_7$ film on CoCrMo alloy was showed in Figure 3.36. It presented absorption bands at 1630 cm^{-1} (amide I) corresponding to the silk II conformation. Other absorption band was seen at 1230 cm^{-1} (amide III), which were characteristic of the silk I structure. But amide II region was not clear. N=O bend, C-O stretch and N-H wag were also seen in this multilayer film in Figure 3.36.

Second graph was drawn for (SF/HA LBL)$_7$ film on CoCrMo alloy in region of 3600 cm^{-1} to 1800 cm^{-1} in Figure 3.37. O-H stretch and N-H stretch were seen clearly.

These spectral varieties were generally attributed to intra- or intermolecular H-bonding.

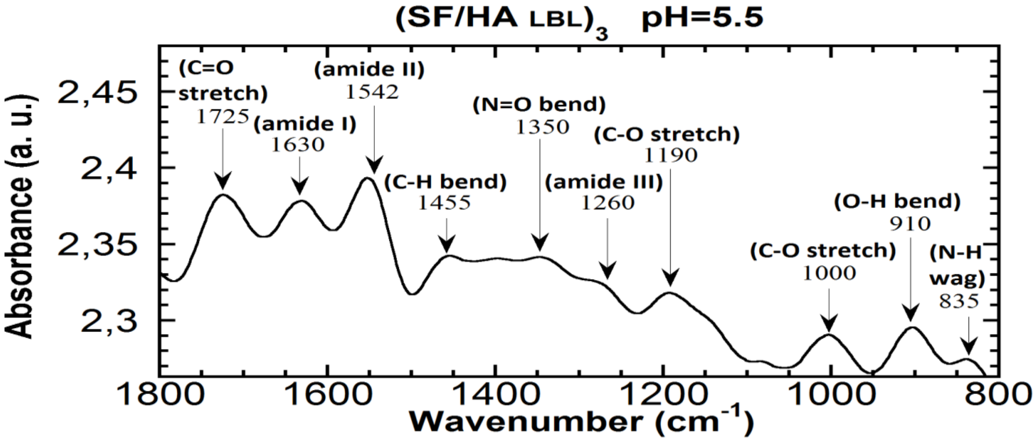

Figure 3.34 : ATR-FTIR spectra of (SF/HA LBL)$_3$ on CoCrMo alloy at pH 5.5.

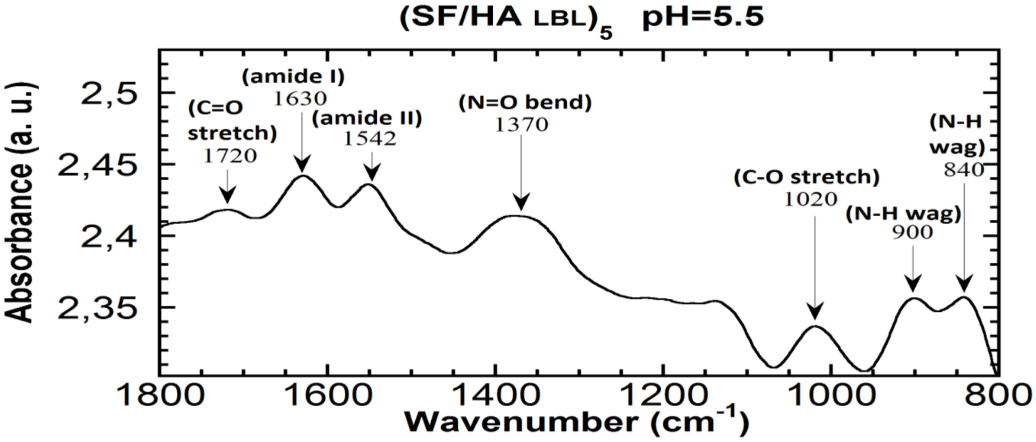

Figure 3.35 : ATR-FTIR spectra of (SF/HA LBL)$_5$ on CoCrMo alloy at pH 5.5.

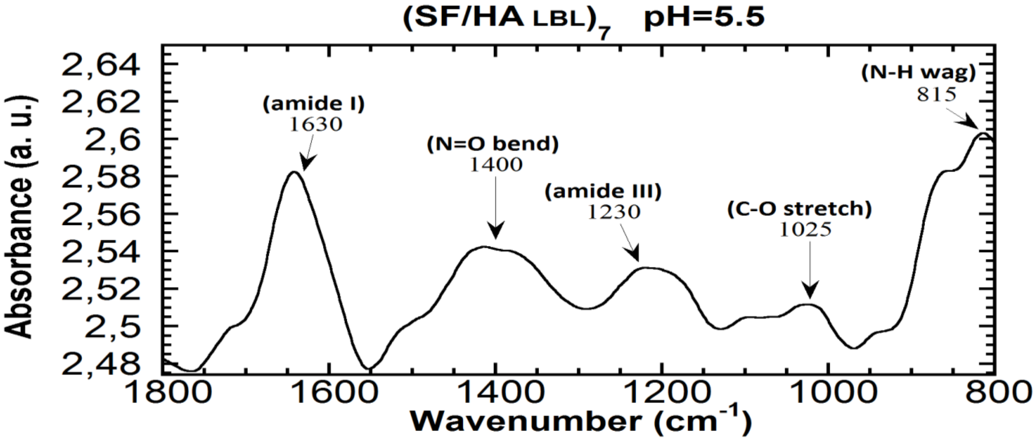

Figure 3.36 : ATR-FTIR spectra of (SF/HA LBL)$_7$ on CoCrMo alloy at pH 5.5.

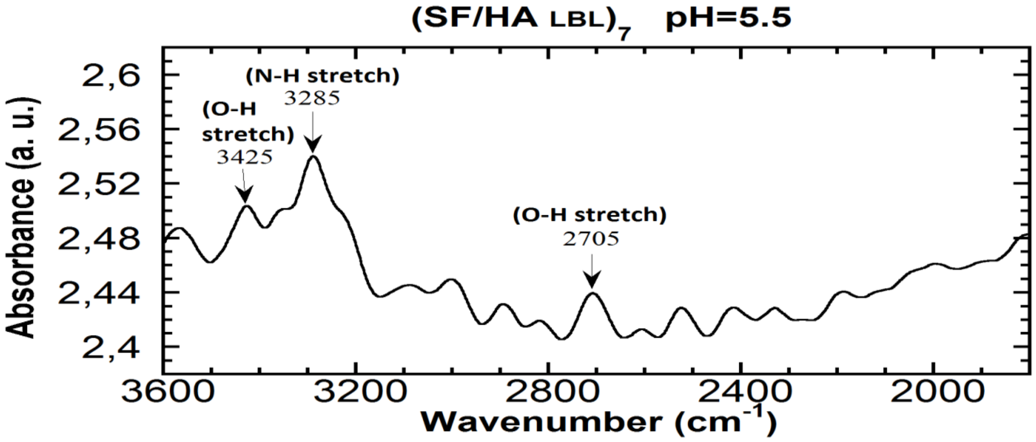

Figure 3.37 : Second ATR-FTIR spectra of (SF/HA LBL)$_7$ on CoCrMo alloy at pH 5.5.

3.1.5 ATR-FTIR results of levofloxacin loaded SF/HA complex and LBL films on CoCrMo alloys

(SF/HA complex + Levofloxacin)$_{14}$ and (SF/HA LBL + Levofloxacin)$_7$ on CoCrMo alloys at pH 3.5 were characterized by ATR-FTIR spectroscopy in Figures of 3.38 and 3.39, respectively. The band position for (SF/HA complex + Levofloxacin)$_{14}$ film at 1685 cm^{-1} was related to C=O stretch in Figure 3.38. This levofloxacin loaded complex film showed the absorption band at 1520 cm^{-1} (amide II) assigned to the silk II structure. Besides that, C-H bend, C-O stretch, =C-H bend, O-H bend were seen in Figure 3.38.

ATR-FTIR spectra of levofloxacin loaded LBL film on CoCrMo alloy at pH 3.5 was shown in Figure 3.39. The absorption peak at 1710 cm^{-1} was related to the C=O stretch. Absorption values of amide I and amide III were attributed to silk II conformation. In addition to, C-H rock, C-O stretch and =C-H bend were determined for (SF/HA LBL + Levofloxacin)$_7$ on CoCrMo alloy at pH 3.5.

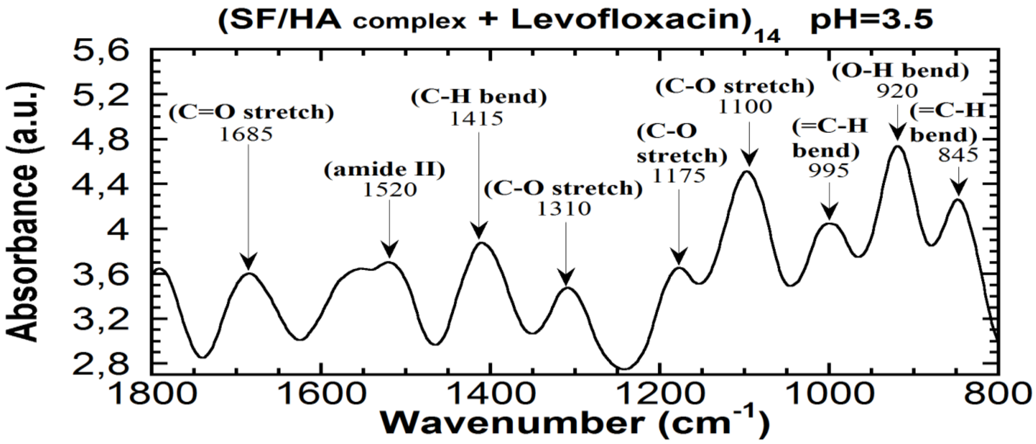

Figure 3.38 : ATR-FTIR spectra of (SF/HA complex + Levofloxacin)$_{14}$ on CoCrMo alloy at pH 3.5.

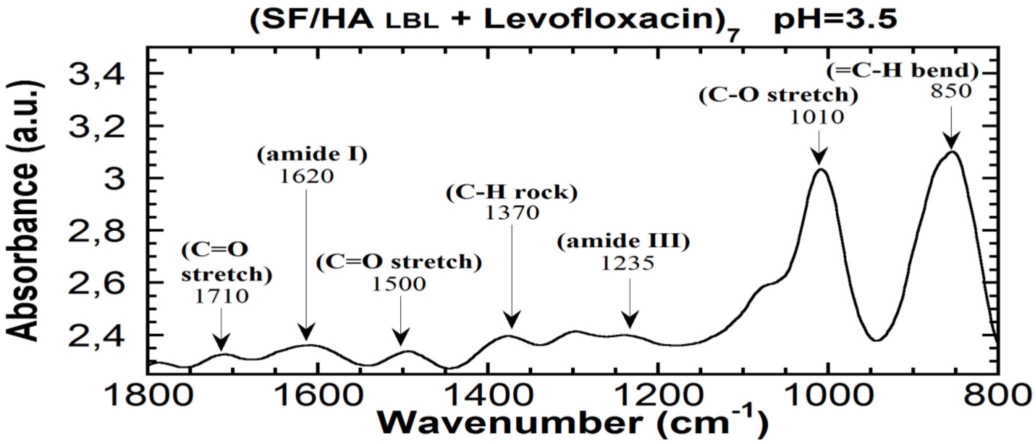

Figure 3.39 : ATR-FTIR spectra of (SF/HA LBL + Levofloxacin)$_7$ on CoCrMo alloy at pH 3.5.

3.2 XRD Results

X-Ray Diffraction (XRD) results of as received CoCrMo alloy, (SF/HA complex)$_{14}$ film on CoCrMo alloy at pH 3.5 and (SF/HA LBL)$_7$ film on CoCrMo alloys at pH 3.5 were shown in Figure 3.40. In Figure 3.40, the fcc and hcp substrate (CoCrMo alloy) peaks were labeled as "γ(hkl)" for the fcc γ-(Co, Cr, Mo) phase and "ε(hkl)" for the hcp ε-(Co, Cr, Mo) phase, respectively.

The as-polished material (the substrate) has polycrystal structure which is face centered cubic (fcc) and hexagonal close packed (hcp) structure. The calculated lattice parameter for the substrate γ-(CoCrMo) phase was 3.579 Å (Türkan 2004). The lattice parameters, a and c, for the substrate ε-(CoCrMo) phase was 1.32 Å and 2.70 Å, respectively (Türkan 2004). Based on the intensity of the XRD peaks in Figure 3.40, the volume percent of the substrate γ phase is estimated to be about 90

%, while the rest (10 %) is due to the substrate ε phase. The XRD spectra of induced films on CoCrMo alloys showed that the films are amorphous structure due to the inorganic phase. However, the reduced substrate peak intensities resulted from the film thickness. As the film thickness increase, the peak intensities decrease. This is related to the X-ray penetration depth to the films.

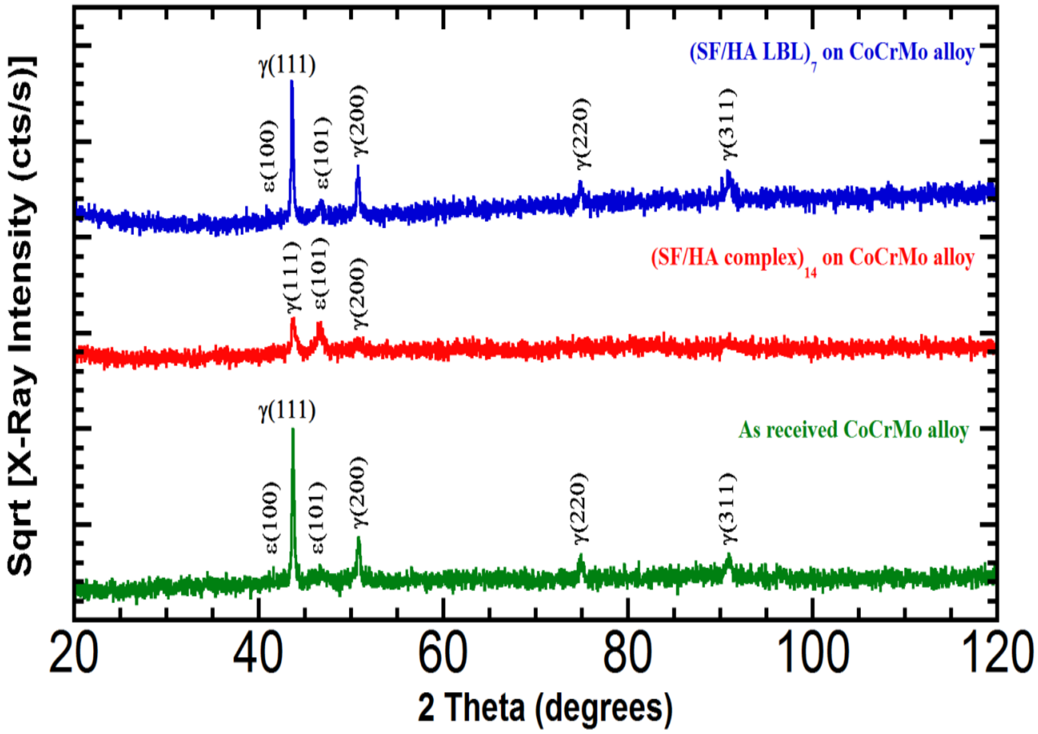

Figure 3.40 : XRD results of as received CoCrMo alloy, (SF/HA complex)$_{14}$ and (SF/HA LBL)$_7$ on CoCrMo alloys at pH 3.5.

3.3 SEM Results

This section is mainly divided into five parts. SEM results of 1) as received CoCrMo alloy, 2) silk fibroin films on CoCrMo alloys, 3) (SF/HA complex) films on CoCrMo alloys, 4) (SF/HA LBL) films on CoCrMo alloys and 5) levofloxacin loaded SF/HA complex and LBL films on CoCrMo alloys.

3.3.1 SEM results of as received CoCrMo alloy

SEM images of as received CoCrMo alloy were shown in Figure 3.41. The SEM images were taken at two different magnitudes 2500× and 5000×, respectively. As was shown in these images, there were some dissimilarities on the surfaces.

In Figure 3.41, bright areas demonstrated higher regions whereas dark areas demonstrated deeper regions on the surfaces. The grinding lines on the surface of the CoCrMo alloy were clearly seen and this was attributed to the carbide precipitations which were also shown in pictures as dark regions.

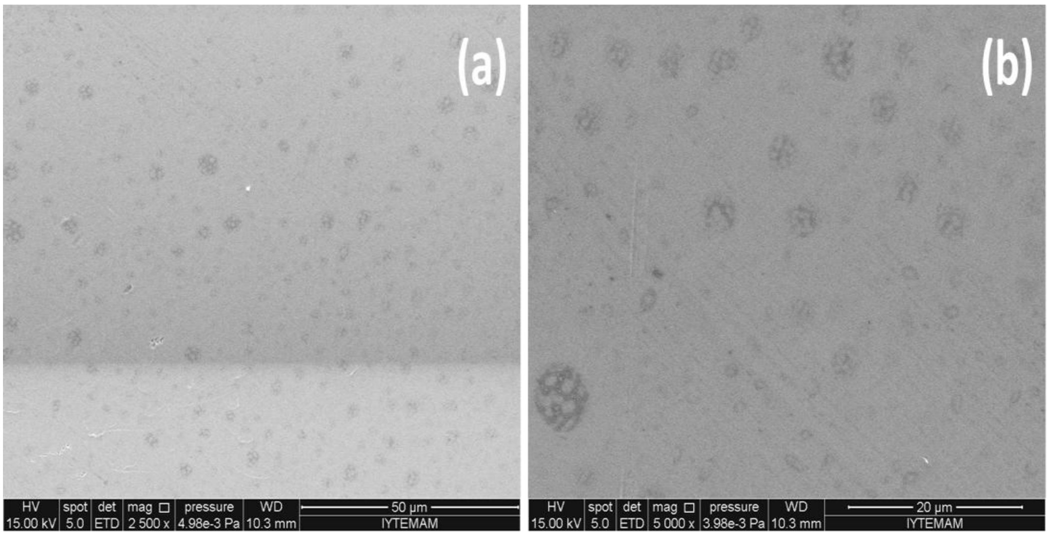

Figure 3.41 : SEM images of as received CoCrMo alloy (a) 2500× magnification and (b) 5000× magnification.

3.3.2 SEM results of silk fibroin films on CoCrMo alloys

Six, ten and fourteen layers of silk fibroin (SF_6, SF_{10}, SF_{14}) films on CoCrMo alloys at different pH values 3.0, 3.5 and 5.5, were investigated by SEM. In order to prove the existence of coatings on CoCrMo alloys, all samples were cut with a needle. Silk fibroin has high mechanical characteristics. All samples were cut with the needle because it was hard to cut with a bistoury. All images were taken at scratched side with the needle and SF coated side and only coated side at 2500× and 5000× magnitudes, respectively.

3.3.2.1 SEM results of SF films at pH 3.0

Figure 3.42 (a-d) shows sequentially the SEM images of $(SF)_6$ film on CoCrMo alloy at pH 3.0 (a) scratched side with needle and SF coated side with 2500× magnification, (b) scratched side with needle and SF coated side with 5000× magnification, (c) SF coated side with 2500× magnification and (d) SF coated side with 5000× magnification. As was shown in these figures, the surface of the CoCrMo alloy was uniformly coated with SF and some small particles were clearly shown in these figures which were resulted from the fibre coming from the silk. This was associated with the isoelectric point of silk fibroin. As the working pH was close the isoelectric point, the fibre formation was seen.

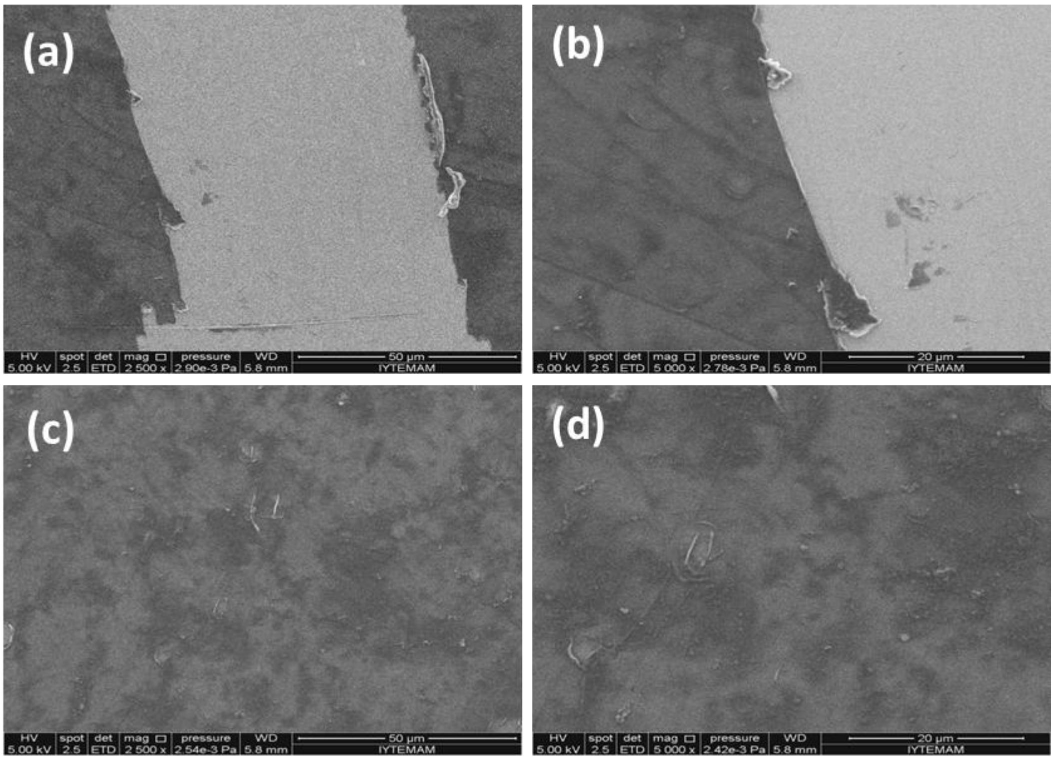

Figure 3.42 : SEM images of $(SF)_6$ on CoCrMo alloy at pH 3.0 (a) Scratched side with needle and silk fibroin coated side with 2500× magnification (b) Scratched side with the needle and silk fibroin coated side with 5000× magnification (c) Silk fibroin coated side with 2500× magnification and (d) Silk fibroin coated side with 5000× magnification.

Figure 3.43 shows sequentially SEM images of $(SF)_{10}$ film on CoCrMo alloy at pH 3.0 (a) scratched side with needle and SF coated side with 2500× magnification, (b) scratched side with needle and SF coated side with 5000× magnification, (c) SF coated side with 2500× magnification and (d) SF coated side with 5000× magnification. In Figure 3.43 (c), small cracks were seen on the surface of the CoCrMo alloy. This was an evidence of the film formation. Crack formation was also related to different thermal expansion coefficient of SF film and substrate material. The film was also peeled off due to the needle cut shown in Figure 3.43 (b).

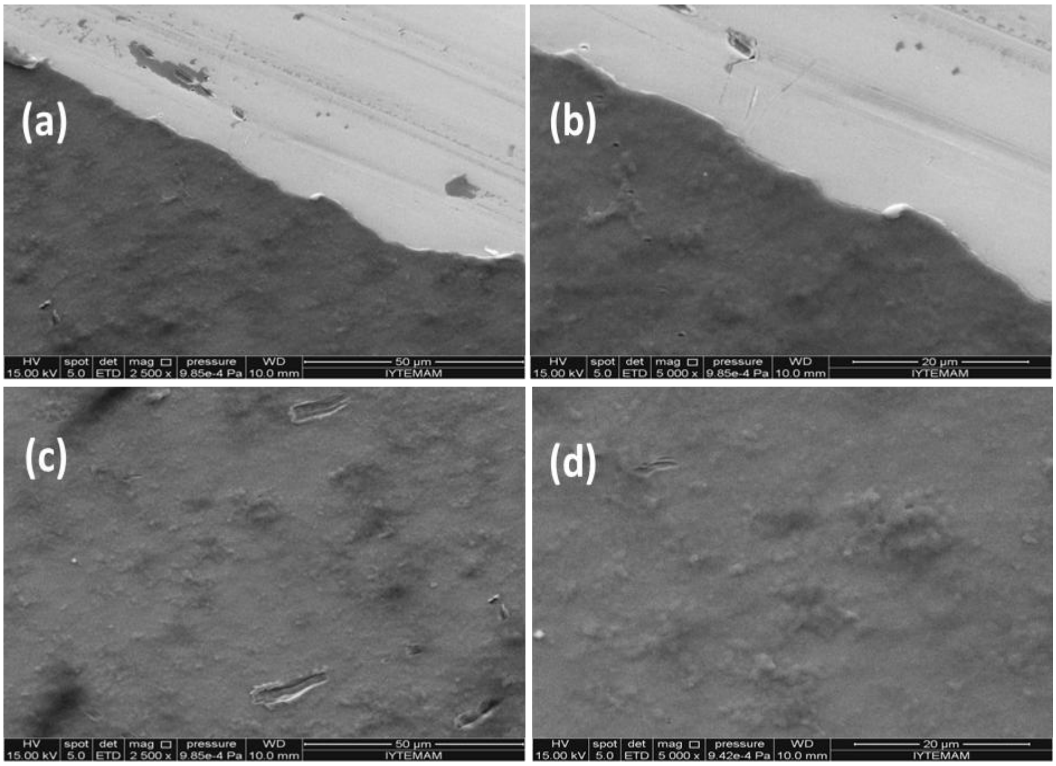

Figure 3.43 : SEM images of $(SF)_{10}$ on CoCrMo alloy at pH 3.0 (a) Scratched side with needle and silk fibroin coated side with 2500× magnification (b) Scratched side with the needle and silk fibroin coated side with 5000× magnification (c) Silk fibroin coated side with 2500× magnification and (d) Silk fibroin coated side with 5000× magnification.

Figure 3.44 shows sequentially SEM images of $(SF)_{14}$ film on CoCrMo alloy at pH 3.0 (a) scratched side with needle and SF coated side with 2500× magnification, (b) scratched side with needle and SF coated side with 5000× magnification, (c) SF coated side with 2500× magnification and (d) SF coated side with 5000× magnification. As was seen in these figures, the surface was fully coated with the silk fibroin and some peeled off films were clearly seen in cutting.

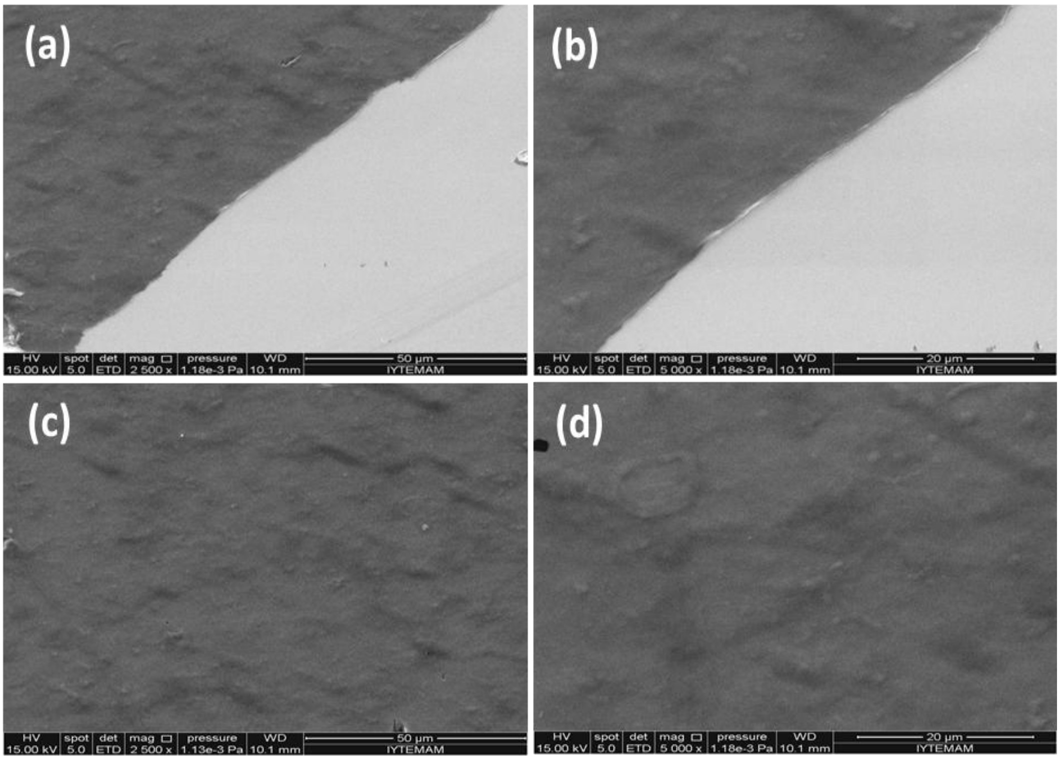

Figure 3.44 : SEM images of $(SF)_{14}$ on CoCrMo alloy at pH 3.0 (a) Scratched side with the needle and silk fibroin coated side with 2500× magnification (b) Scratched side with the needle and silk fibroin coated side with 5000× magnification (c) Silk fibroin coated side with 2500× magnification and (d) Silk fibroin coated side with 5000× magnification.

3.3.2.2 SEM results of SF films at pH 3.5

Figure 3.45 shows sequentially SEM images of $(SF)_6$ film on CoCrMo alloy at pH 3.5 (a) scratched side with the needle and SF coated side with 2500× magnification, (b) scratched side with the needle and SF coated side with 5000× magnification, (c) SF coated side with 2500× magnification and (d) SF coated side with 5000× magnification. The dark regions in scratched side showed in Fig.3.45 (a) quite correlate the hard SF films. Some agglomerations shown in Fig.3.45 (b) were related to the SF structure. The working pH was also close to the isoelectric point that corresponds to the good film formation. Small grinding lines were still visible. This confirmed that the film was very thin.

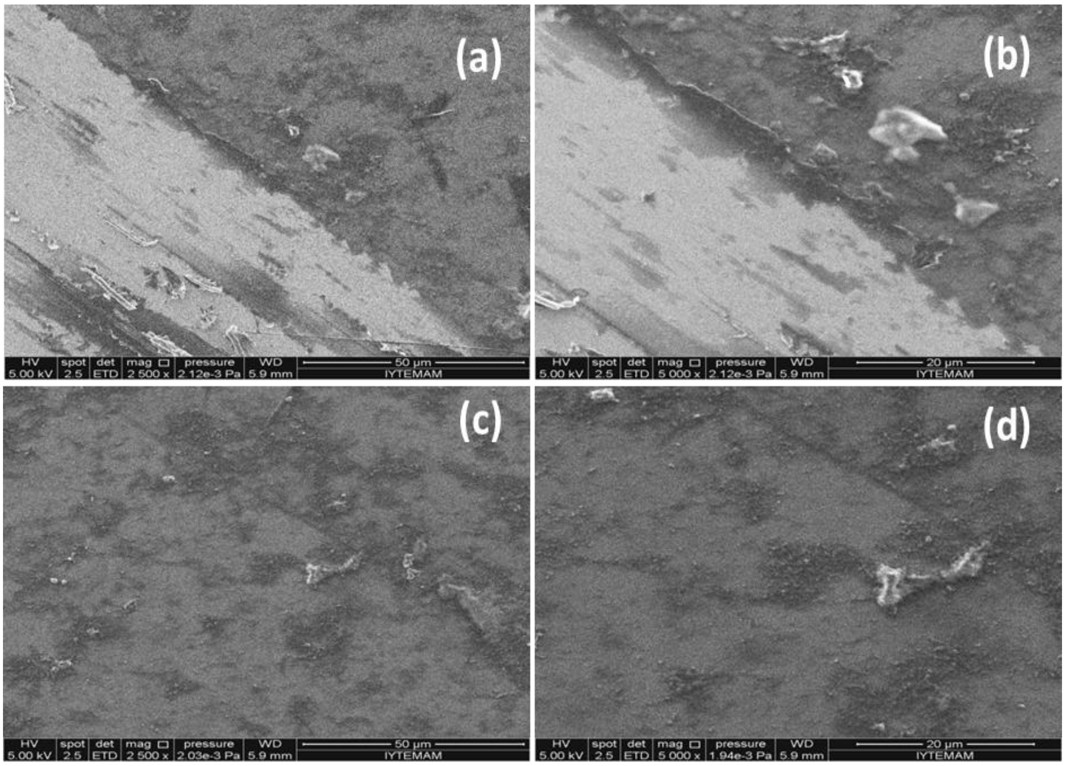

Figure 3.45 : SEM images of $(SF)_6$ on CoCrMo alloy at pH 3.5 (a) Scratched side with the needle and silk fibroin coated side with 2500× magnification (b) Scratched side with the needle and silk fibroin coated side with 5000× magnification (c) Silk fibroin coated side with 2500× magnification and (d) Silk fibroin coated side with 5000× magnification.

Figure 3.46 shows sequentially SEM images of $(SF)_{10}$ film on CoCrMo alloy at pH 3.5 (a) scratched side with the needle and SF coated side with 2500× magnification (b) scratched side with the needle and SF coated side with 5000× magnification (c) SF coated side with 2500× magnification and (d) SF coated side with 5000× magnification. Similar findings were also valid in this case. However, very fine scratches in Fig. 3.46 (a) were resulted from the needle scratching. Some small particle as well as big particles was agglomerated to the surface of the film. Grinding lines were still visible and they were fully coated with silk fibroin.

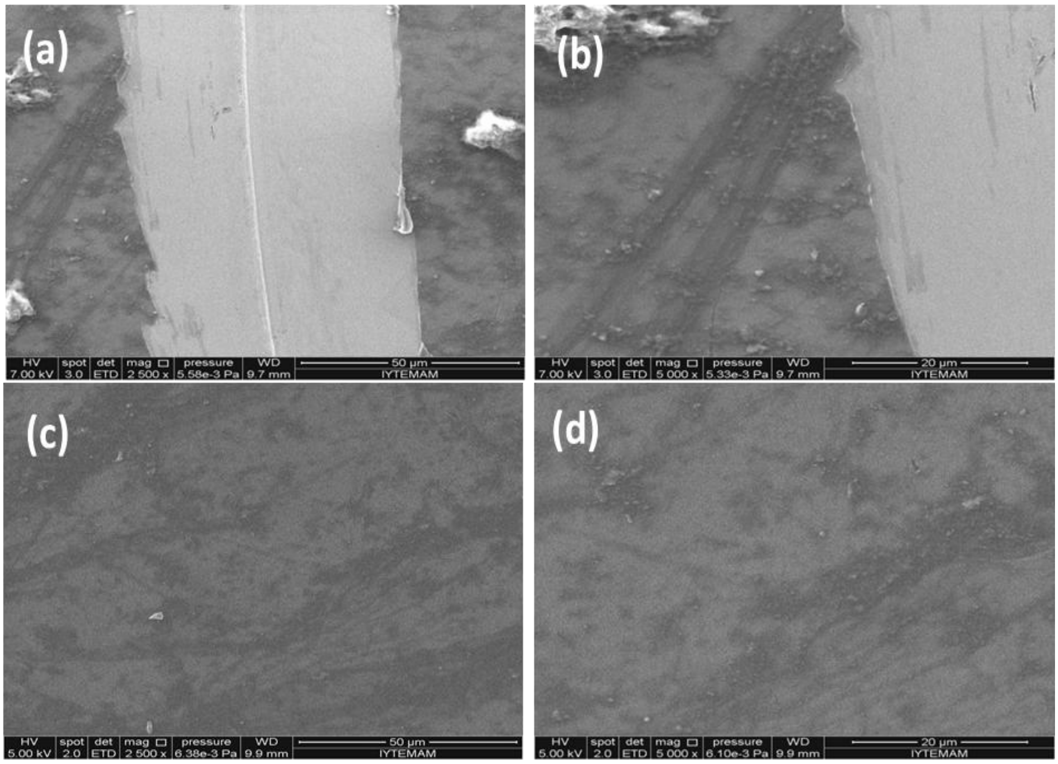

Figure 3.46 : SEM images of $(SF)_{10}$ on CoCrMo alloy at pH 3.5 (a) Scratched side with the needle and silk fibroin coated side with 2500× magnification (b) Scratched side with the needle and silk fibroin coated side with 5000× magnification (c) Silk fibroin coated side with 2500× magnification and (d) Silk fibroin coated side with 5000× magnification.

Figure 3.47 shows sequentially SEM images of $(SF)_{14}$ film on CoCrMo alloy at pH 3.5 (a) scratched side with the needle and SF coated side with 2500× magnification, (b) scratched side with the needle and SF coated side with 5000× magnification, (c) SF coated side with 2500× magnification and (d) SF coated side with 5000× magnification. Besides similar findings, some crack formations on the surface of the film were shown in Fig. 3.47 (c).

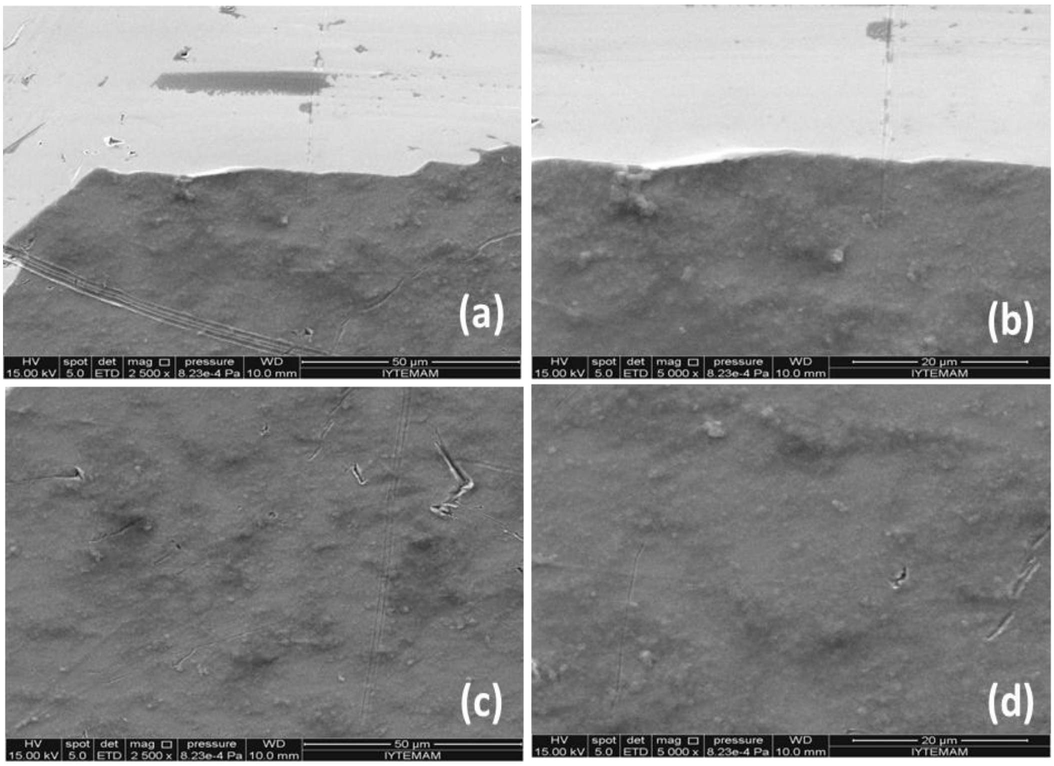

Figure 3.47 : SEM images of $(SF)_{14}$ on CoCrMo alloy at pH 3.5 (a) Scratched side with the needle and silk fibroin coated side with 2500× magnification (b) Scratched side with the needle and silk fibroin coated side with 5000× magnification (c) Silk fibroin coated side with 2500× magnification and (d) Silk fibroin coated side with 5000× magnification.

3.3.2.3 SEM results of SF films at pH 5.5

Figures 3.48, 3.49 and 3.50 show SEM images of $(SF)_6$, $(SF)_{10}$ and $(SF)_{14}$ films on CoCrMo alloys at pH 5.5 (a) scratched side with the needle and SF coated side with 2500× magnification, (b) scratched side with the needle and SF coated side with 5000× magnification, (c) SF coated side with 2500× magnification and (d) SF coated side with 5000× magnification, respectively. The induced SF films were uniform in all coating layers. This was due to the working pH which was far away to the isoelectric point of fibroin (IEP=3.9). In this pH, the fibres of SF were moved to the everywhere freely. As a result, the formed film was free of fibre.

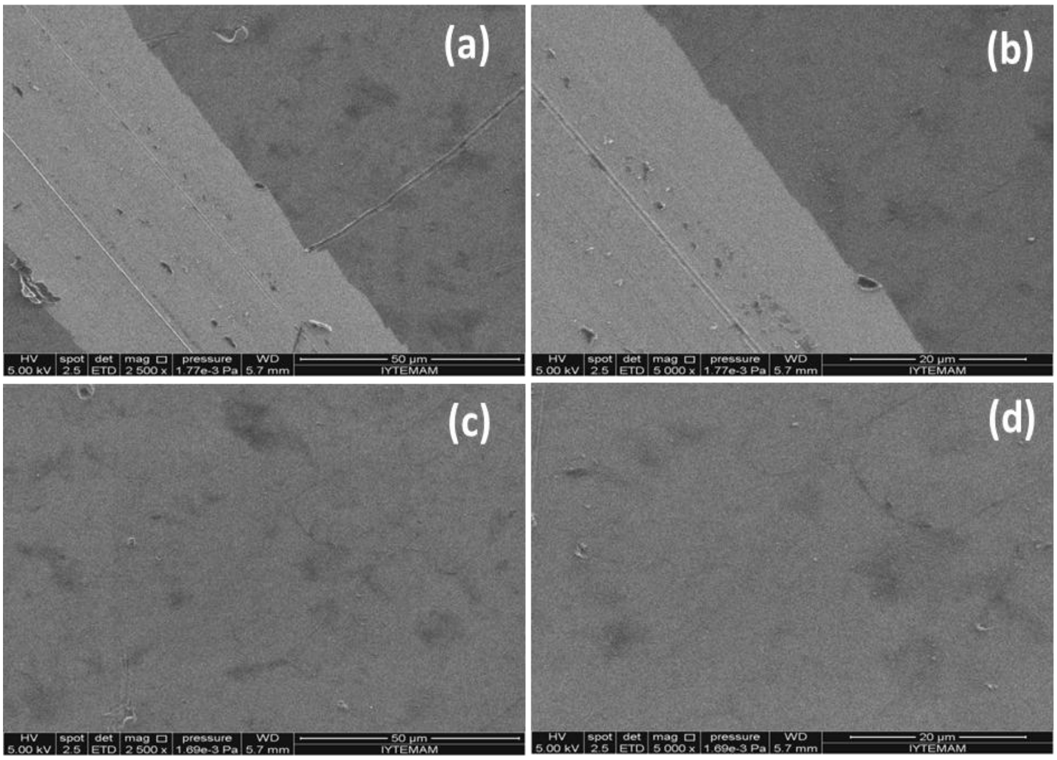

Figure 3.48 : SEM images of $(SF)_6$ on CoCrMo alloy at pH 5.5 (a) Scratched side with the needle and silk fibroin coated side with 2500× magnification (b) Scratched side with the needle and silk fibroin coated side with 5000× magnification (c) Silk fibroin coated side with 2500× magnification and (d) Silk fibroin coated side with 5000× magnification.

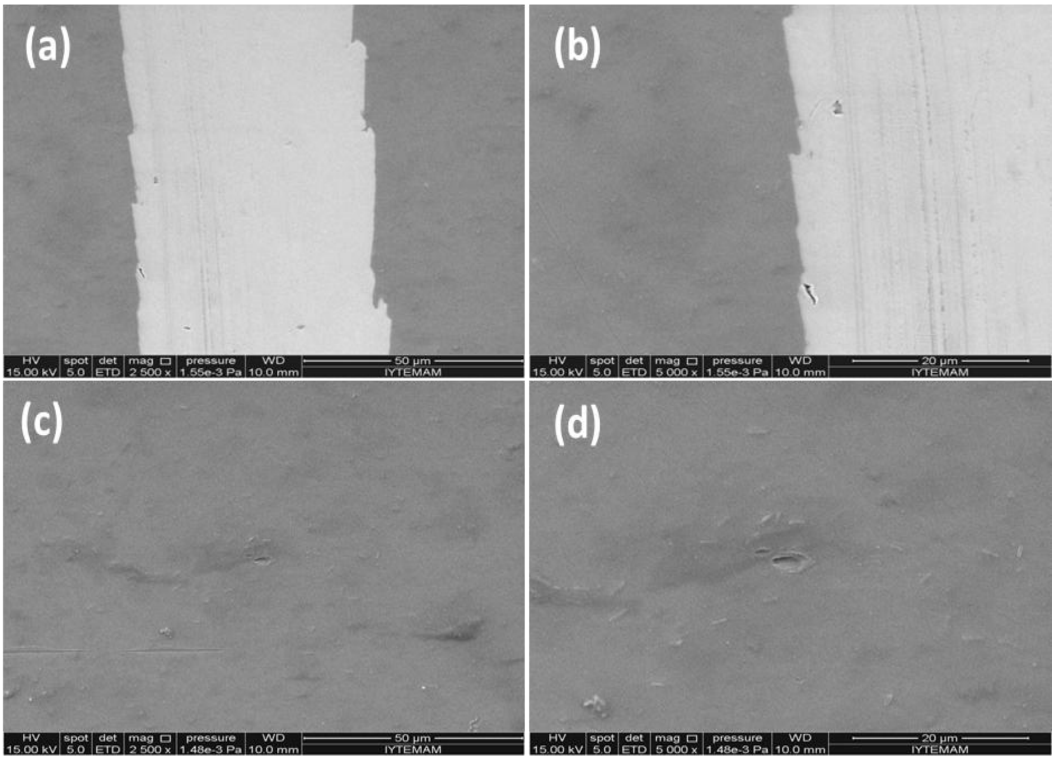

Figure 3.49 : SEM images of $(SF)_{10}$ on CoCrMo alloy at pH 5.5 (a) Scratched side with the needle and silk fibroin coated side with 2500× magnification (b) Scratched side with the needle and silk fibroin coated side with 5000× magnification (c) Silk fibroin coated side with 2500× magnification and (d) Silk fibroin coated side with 5000× magnification.

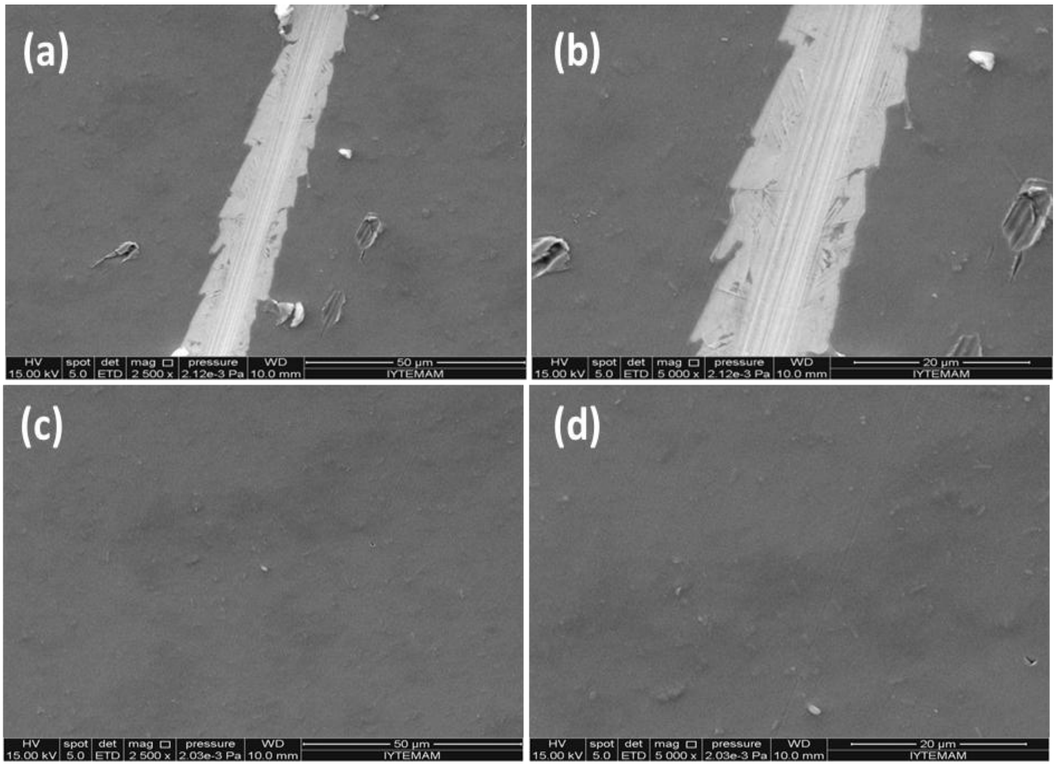

Figure 3.50 : SEM images of $(SF)_{14}$ on CoCrMo alloy at pH 5.5 (a) Scratched side with the needle and silk fibroin coated side with 2500× magnification (b) Scratched side with the needle and silk fibroin coated side with 5000× magnification (c) Silk fibroin coated side with 2500× magnification and (d) Silk fibroin coated side with 5000× magnification.

3.3.3 SEM results of (SF/HA complex) films on CoCrMo alloys

Six, ten and fourteen layers of silk fibroin/hyaluronic acid complex films ($(SF/HA\ complex)_6$, $(SF/HA\ complex)_{10}$, $(SF/HA\ complex)_{14}$) on CoCrMo alloys at pH 3.0, 3.5 and 5.5 were investigated by SEM. In order to prove the existence of coatings on CoCrMo alloys, all samples were cut with a bistoury. All images were taken at scratched side with the bistoury and complex coated side and only complex coated side at 2500× and 5000× magnitudes.

3.3.3.1 SEM results of (SF/HA complex) films at pH 3.0

Figures 3.51, 3.52 and 3.53 shows SEM images of $(SF/HA\ complex)_6$ $(SF/HA\ complex)_{10}$ and $(SF/HA\ complex)_{14}$ films on CoCrMo alloys at pH 3.0 (a) scratched side with the bistoury and complex coated side with 2500× magnification, (b) scratched side with the bistoury and complex coated side with 5000× magnification, (c) complex coated side with 2500× magnification and (d) complex coated side with 5000× magnification, respectively. Small particles were seen on the surface of all layered films that was resulted from the complex formation. Due to the bistoury cutting, the film was peeled off Fig. 3.51 (a-b), Fig. 3.52 (a-b) and Fig. 3.53 (a-b) and it was clearly shown in all sections. Some grinding lines and surface cracks accompanies to the all films. Surface crack formation was mainly associated with different thermal expansion coefficients. However, drying section at the end of the film preparation may influence the surface cracks.

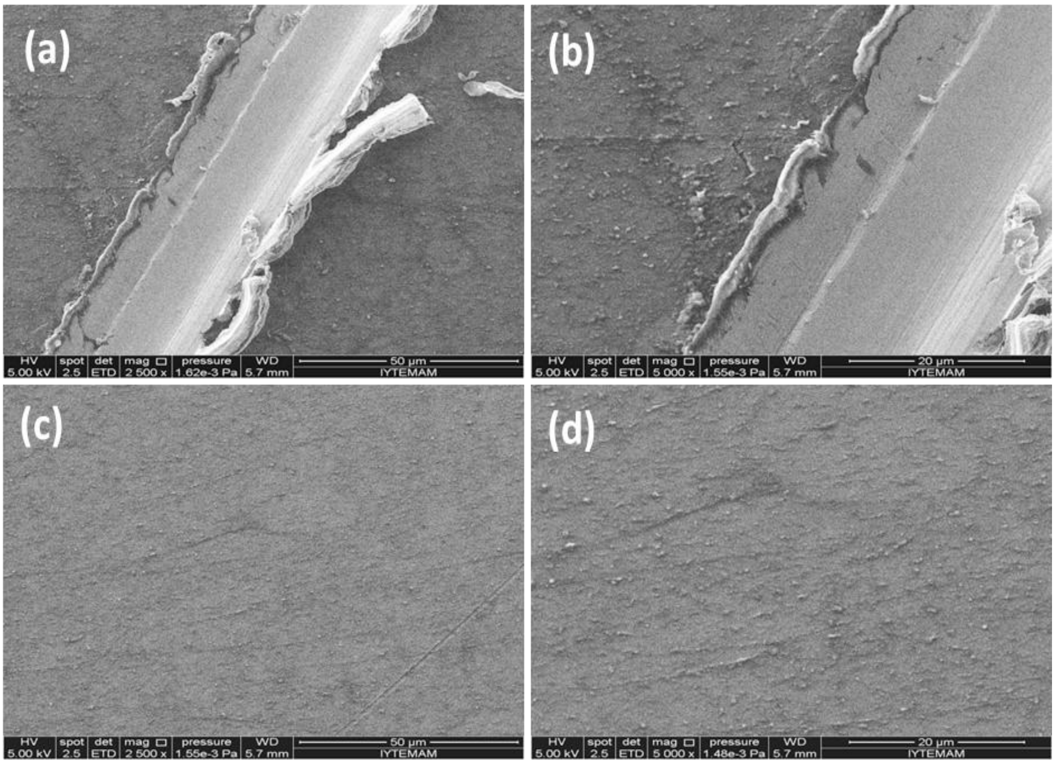

Figure 3.51 : SEM images of (SF/HA complex)$_6$ on CoCrMo alloy at pH 3.0 (a) Scratched side with the bistoury and complex coated side with 2500× magnification (b) Scratched side with the bistoury and complex coated side with 5000× magnification (c) Complex coated side with 2500× magnification and (d) Complex coated side with 5000× magnification.

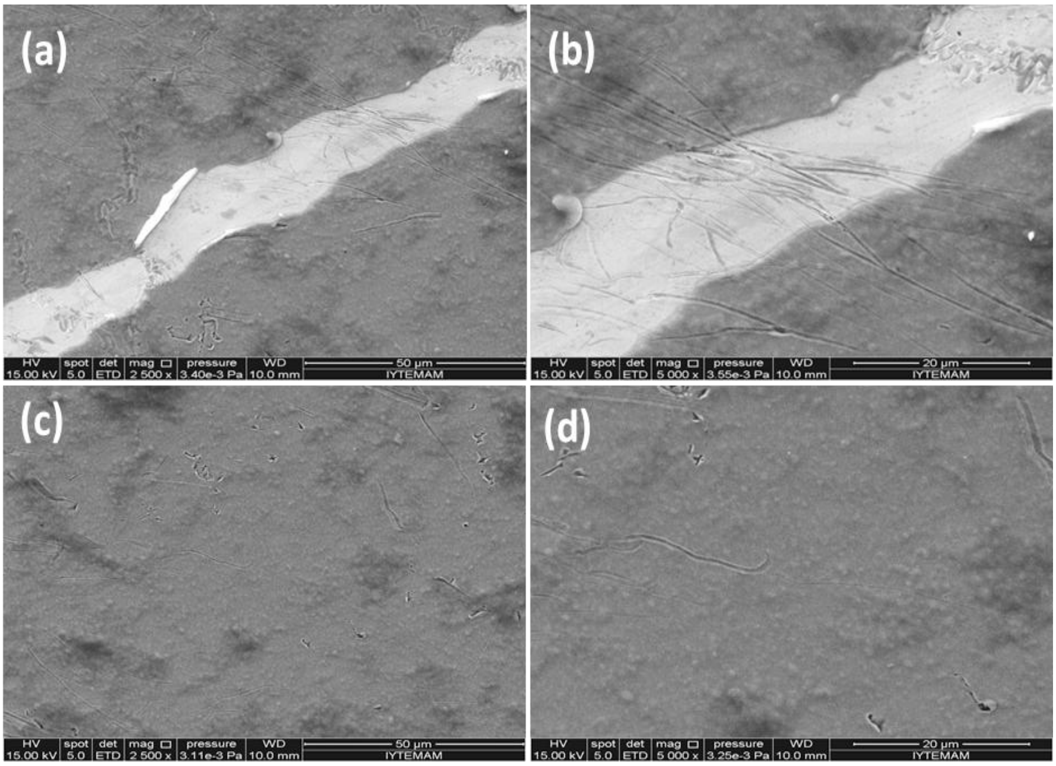

Figure 3.52 : SEM images of (SF/HA complex)$_{10}$ on CoCrMo alloy at pH 3.0 (a) Scratched side with the bistoury and complex coated side with 2500× magnification (b) Scratched side with the bistoury and complex coated side with 5000× magnification (c) Complex coated side with 2500× magnification and (d) Complex coated side with 5000× magnification.

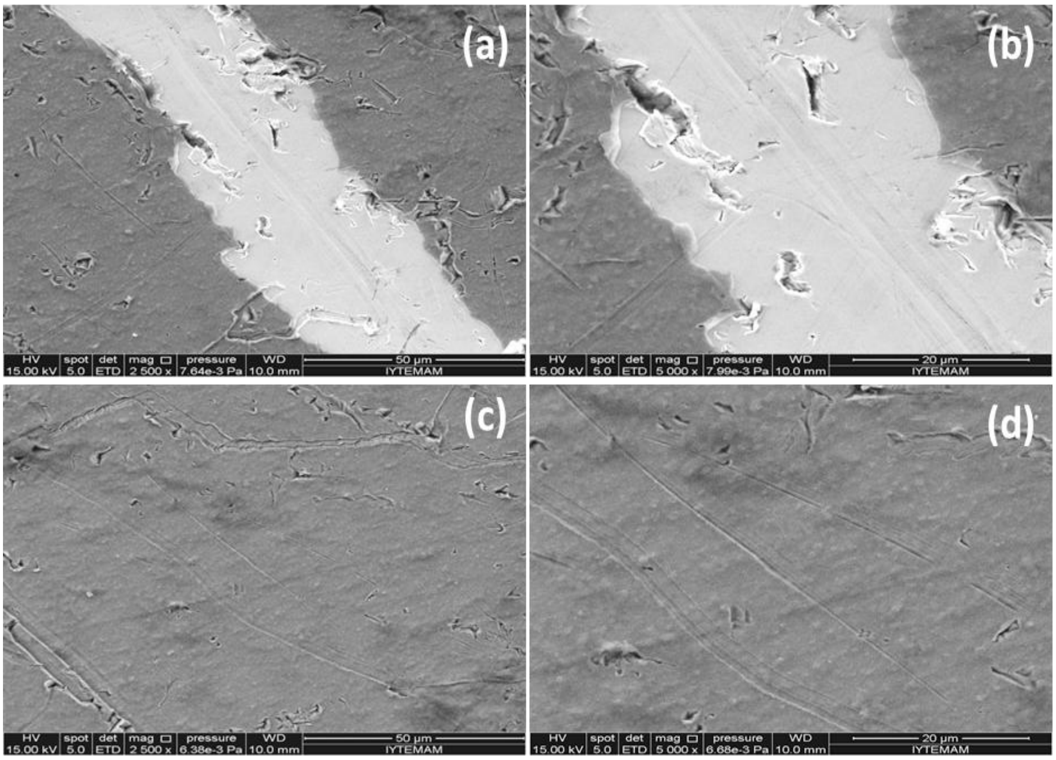

Figure 3.53 : SEM images of (SF/HA complex)$_{14}$ on CoCrMo alloy at pH 3.0 (a) Scratched side with the bistoury and complex coated side with 2500× magnification (b) Scratched side with the bistoury and complex coated side with 5000× magnification (c) Complex coated side with 2500× magnification and (d) Complex coated side with 5000× magnification.

3.3.3.2 SEM results of (SF/HA complex) films at pH 3.5

Figure 3.54, 3.55 and 3.56 shows SEM images of (SF/HA complex)$_6$ (SF/HA complex)$_{10}$ and (SF/HA complex)$_{14}$ films on CoCrMo alloys at pH 3.5 (a) scratched side with the bistoury and complex coated side with 2500× magnification, (b) scratched side with the bistoury and complex coated side with 5000× magnification, (c) complex coated side with 2500× magnification and (d) complex coated side with 5000× magnification, respectively. As was seen in Fig. 3.54 (d), 3.55 (c), (d) and 3.56 (c) and (d), some black regions were seen clearly. This was due to the degree of agglomeration in formation of the complex coacervation. In this case, at pH 3.5, the stock solution consists of silk fibroin and hyaluronic acid as a rate of 32:1. This means that polyelectrolyte solution has higher rate of positively charged ions. Therefore, this influences the fibre formation and complex coacervation. As a result, the black regions seen are the result of the fibrillation in stock solution. Similarly, small cracks are also present on the surface of the alloy.

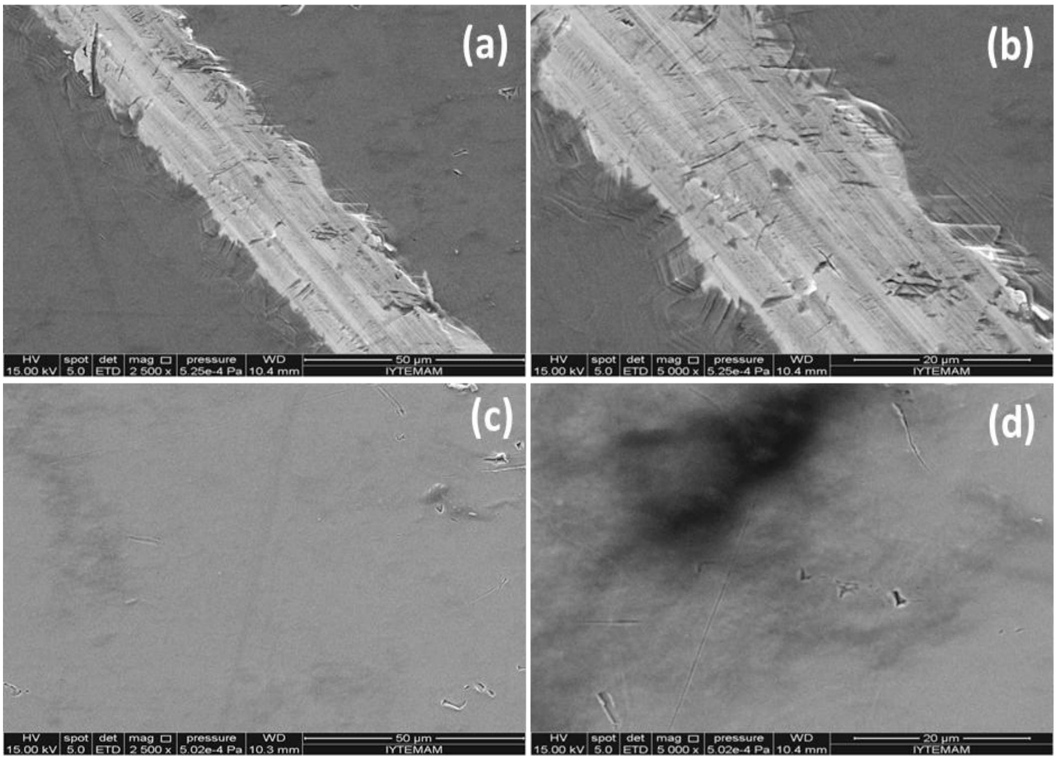

Figure 3.54 : SEM images of (SF/HA complex)$_6$ on CoCrMo alloy at pH 3.5 (a) Scratched side with the bistoury and complex coated side with 2500× magnification (b) Scratched side with the bistoury and complex coated side with 5000× magnification (c) Complex coated side with 2500× magnification and (d) Complex coated side with 5000× magnification.

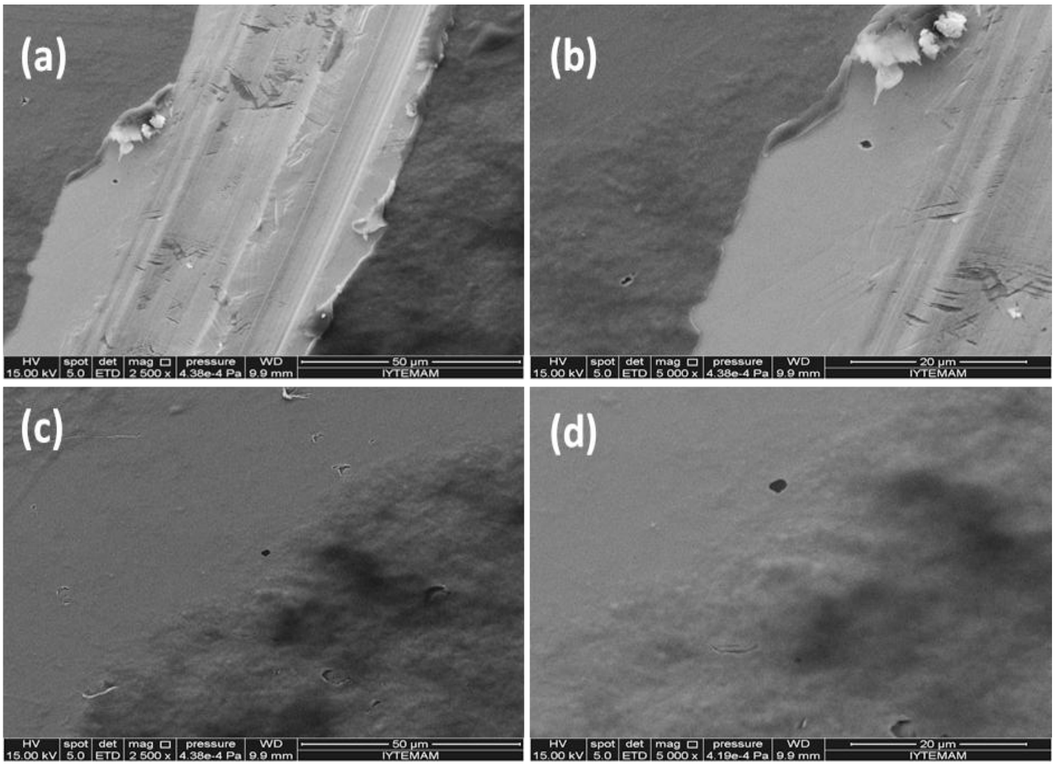

Figure 3.55 : SEM images of (SF/HA complex)$_{10}$ on CoCrMo alloy at pH 3.5 (a) Scratched side with the bistoury and complex coated side with 2500× magnification (b) Scratched side with the bistoury and complex coated side with 5000× magnification (c) Complex coated side with 2500× magnification and (d) Complex coated side with 5000× magnification.

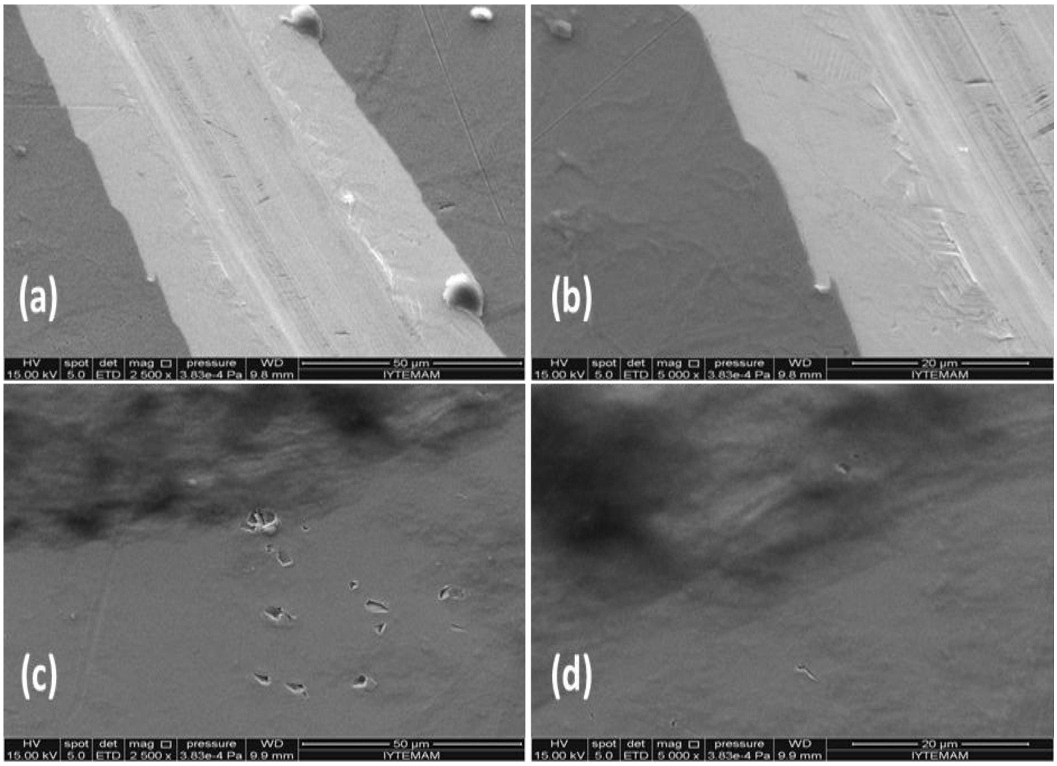

Figure 3.56 : SEM images of (SF/HA complex)$_{14}$ on CoCrMo alloy at pH 3.5 (a) Scratched side with the bistoury and complex coated side with 2500× magnification (b) Scratched side with the bistoury and complex coated side with 5000× magnification (c) Complex coated side with 2500× magnification and (d) Complex coated side with 5000× magnification.

3.3.3.3 SEM results of (SF/HA complex) films at pH 5.5

Figure 3.57, 3.58 and 3.59 shows SEM images of (SF/HA complex)$_6$ (SF/HA complex)$_{10}$ and (SF/HA complex)$_{14}$ films on CoCrMo alloys at pH 5.5 (a) scratched side with the bistoury and complex coated side with 2500× magnification, (b) scratched side with the bistoury and complex coated side with 5000× magnification, (c) complex coated side with 2500× magnification and (d) complex coated side with 5000× magnification, respectively. The induced (SF/HA complex) films were uniform in all coating layers. This was due to the working pH which was far away to the isoelectric point of SF. In this pH, SF and HA both were negatively charged and the fibres of SF were moved to the everywhere freely. As a result, the formed film was free of fibre.

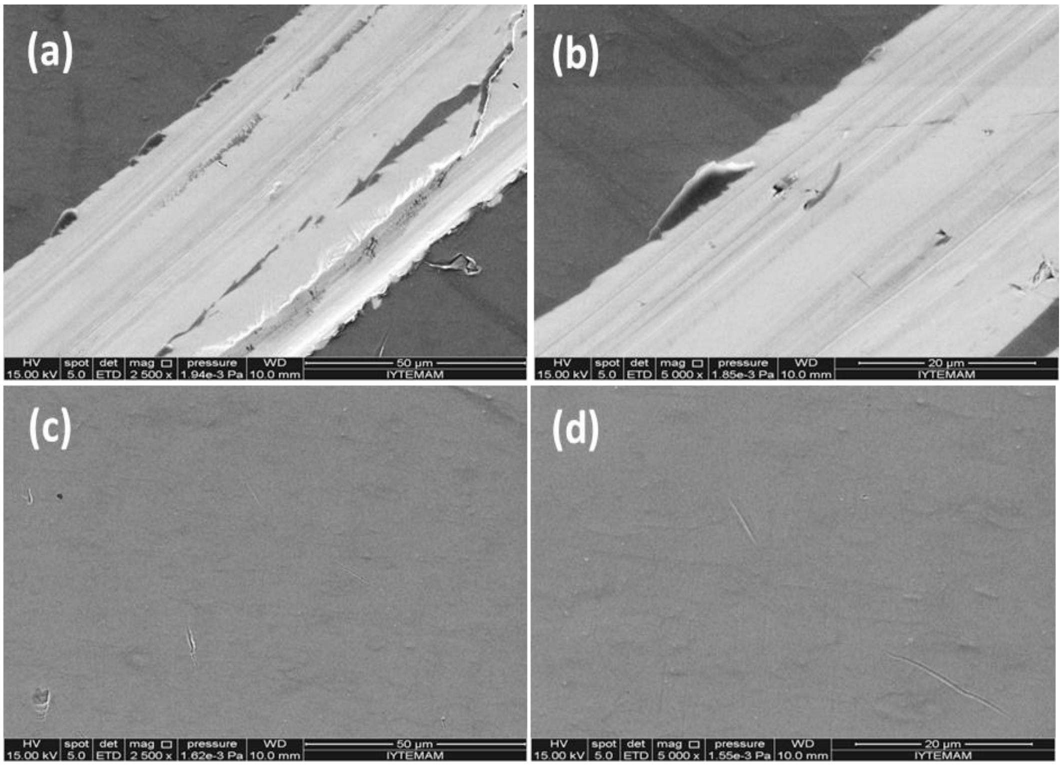

Figure 3.57 : SEM images of (SF/HA complex)$_6$ on CoCrMo alloy at pH 5.5 (a) Scratched side with the bistoury and complex coated side with 2500× magnification (b) Scratched side with the bistoury and complex coated side with 5000× magnification (c) Complex coated side with 2500× magnification and (d) Complex coated side with 5000× magnification.

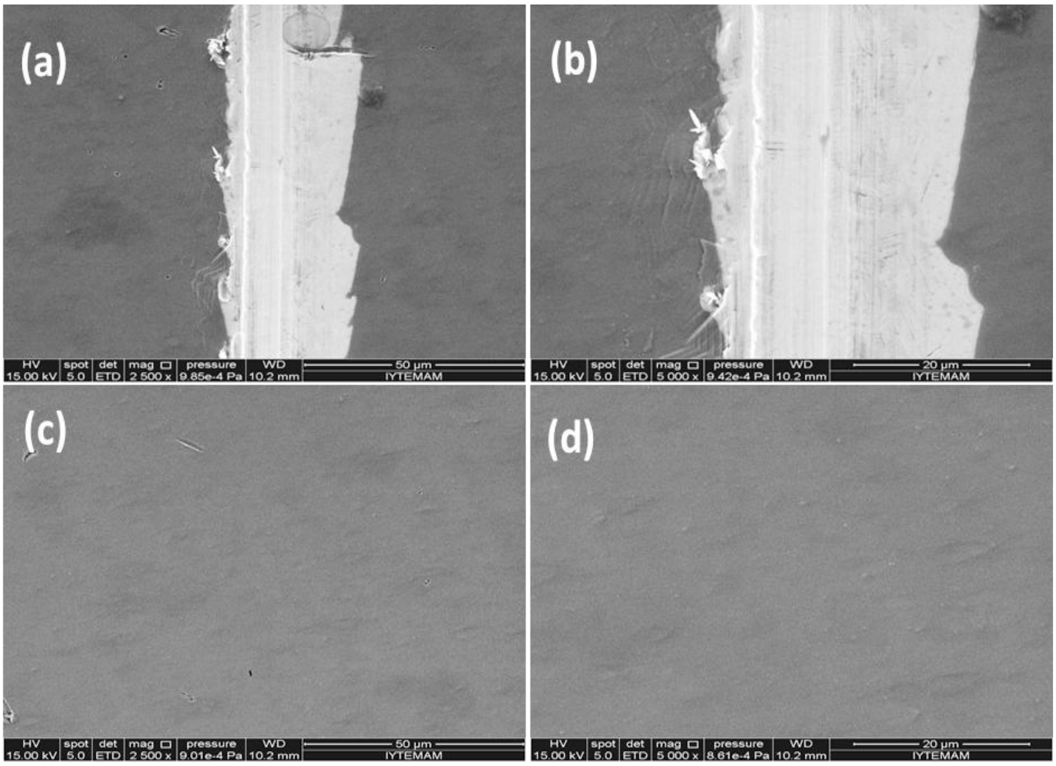

Figure 3.58 : SEM images of (SF/HA complex)$_{10}$ on CoCrMo alloy at pH 5.5 (a) Scratched side with the bistoury and complex coated side with 2500× magnification (b) Scratched side with the bistoury and complex coated side with 5000× magnification (c) Complex coated side with 2500× magnification and (d) Complex coated side with 5000× magnification**.**

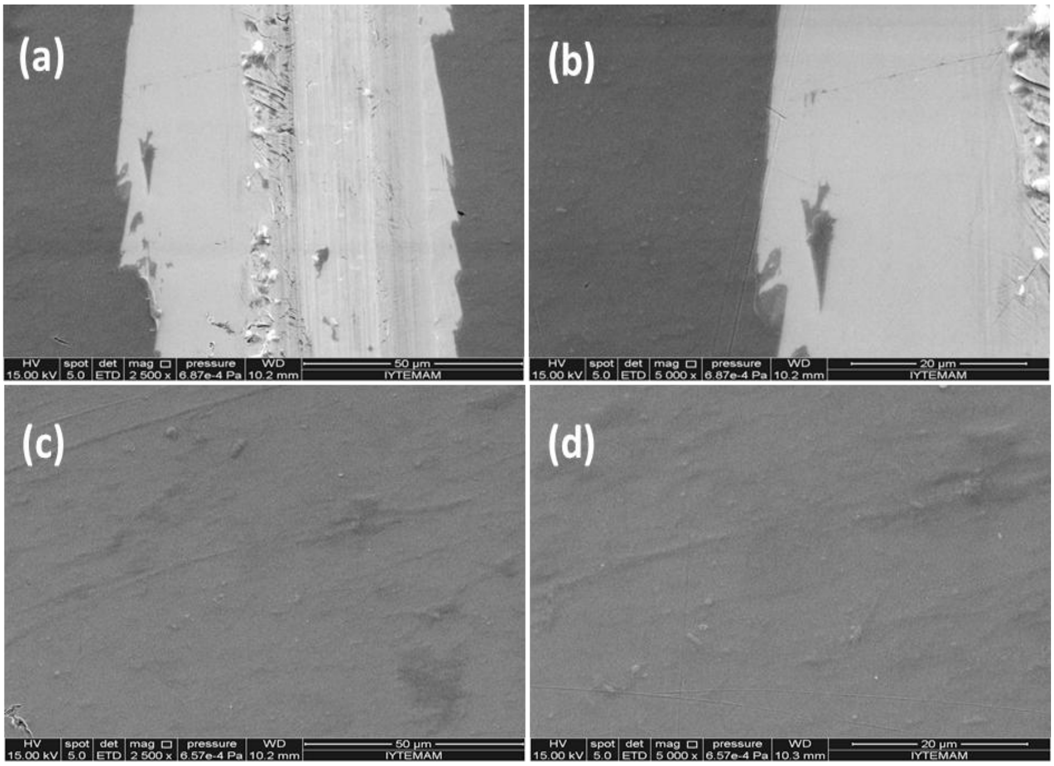

Figure 3.59 : SEM images of (SF/HA complex)$_{14}$ on CoCrMo alloy at pH 5.5 (a) Scratched side with the bistoury and complex coated side with 2500× magnification (b) Scratched side with the bistoury and complex coated side with 5000× magnification (c) Complex coated side with 2500× magnification and (d) Complex coated side with 5000× magnification.

3.3.4 SEM results of (SF/HA LBL) films on CoCrMo alloys

Six, ten and fourteen layers of silk fibroin/hyaluronic acid layer-by-layer ((SF/HA LBL)$_3$, (SF/HA LBL)$_5$, (SF/HA LBL)$_7$) films on CoCrMo alloys at pH 3.0, 3.5 and 5.5, were investigated by SEM. All samples were cut with the bistoury to identify the substrate. All images were taken at scratched side with a bistoury and LBL coated side and only LBL coated side at 2500× and 5000× magnitudes, respectively.

3.3.4.1 SEM results of (SF/HA LBL) films at pH 3.0

Figure 3.60, 3.61 and 3.62 shows SEM images of (SF/HA LBL)$_3$, (SF/HA LBL)$_5$ and (SF/HA LBL)$_7$ films on CoCrMo alloys at pH 3.0 (a) scratched side with the bistoury and LBL coated side with 2500× magnification, (b) scratched side with the bistoury and LBL coated side with 5000× magnification, (c) LBL coated side with 2500× magnification and (d) LBL coated side with 5000× magnification, respectively. In this process, the outermost layer is hyaluronic acid. The SEM investigation mainly comes from this top layer. The white regions seen on the surface of the films may be commonly hyaluronic acid/silk fibroin complex precipitates. Before the end stage the surface of the film is positively charged due to the silk fibroin. When it was placed into the hyaluronic acid, fully negatively charged, the silk fibroin and hyaluronic acid forms the complex coacervation. However, the complexation may be retarded due to the less density of negative charges. As the number of layer increases, the amount of fibre increases. This finding quite correlates our admission in the previous part. On the other hand, the number of silk fibroin layer influences the complex formation. The increase of the silk fibroin also results in the increase of positively charged ions in solution.

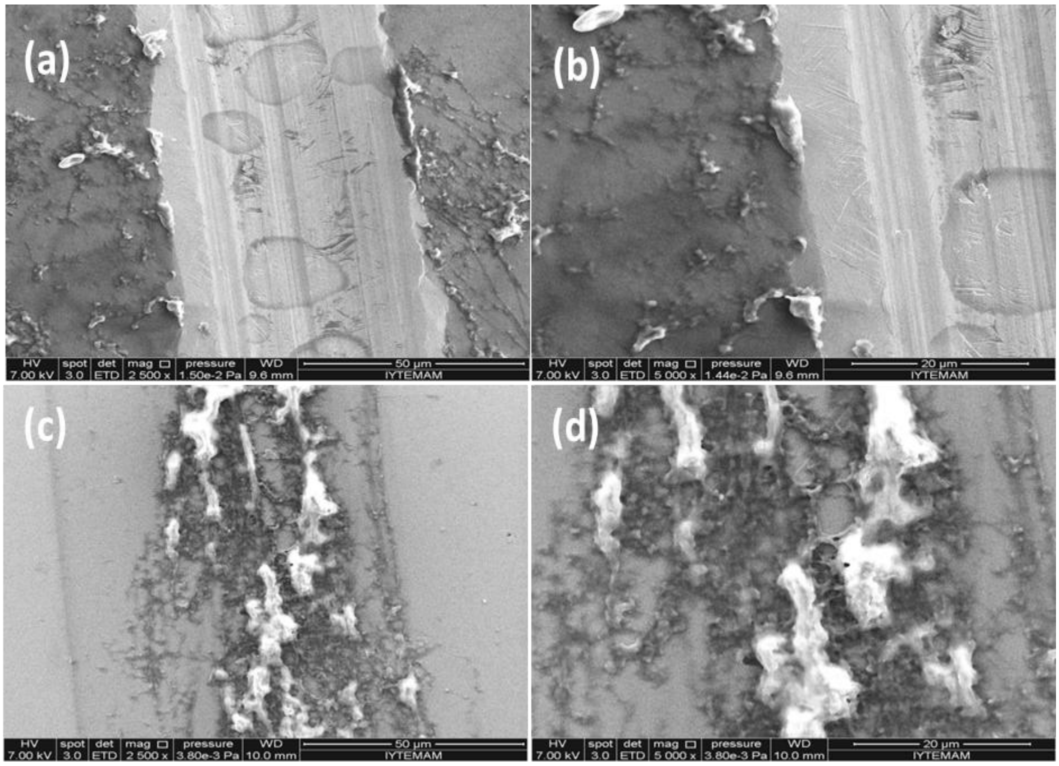

Figure 3.60 : SEM images of (SF/HA LBL)$_3$ on CoCrMo alloy at pH 3.0 (a) Scratched side with the bistoury and LBL coated side with 2500× magnification (b) Scratched side with the bistoury and LBL coated side with 5000× magnification (c) LBL coated side with 2500× magnification and (d) LBL coated side with 5000× magnification.

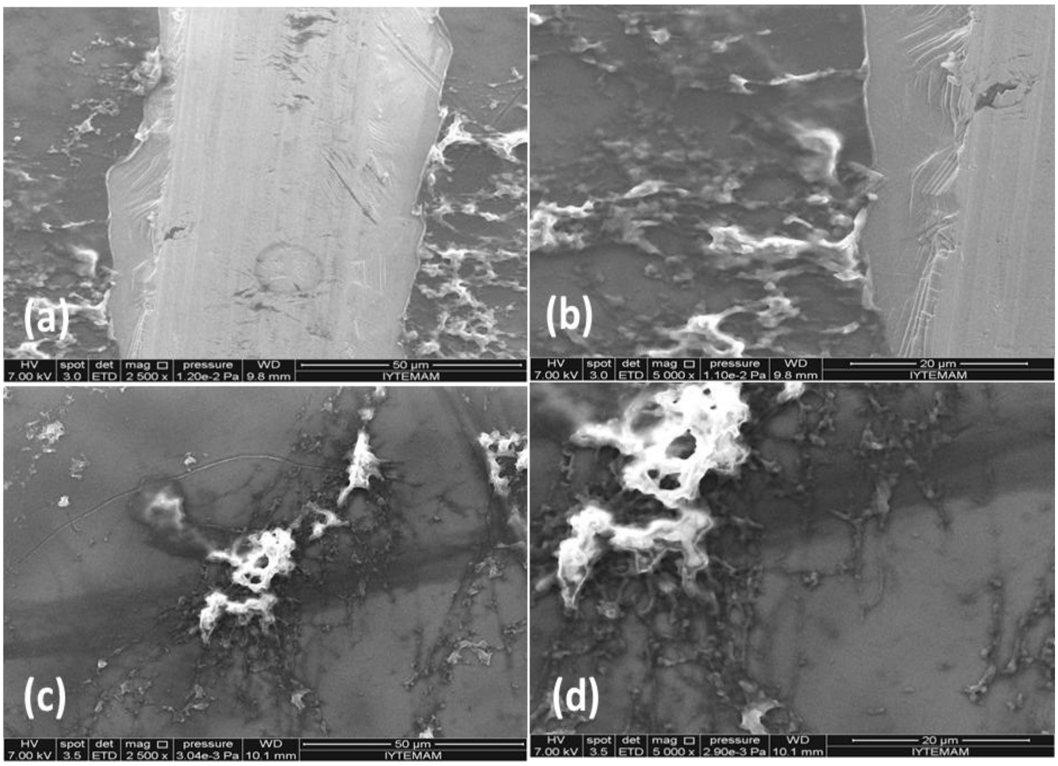

Figure 3.61 : SEM images of (SF/HA LBL)$_5$ on CoCrMo alloy at pH 3.0 (a) Scratched side with the bistoury and LBL coated side with 2500× magnification (b) Scratched side with the bistoury and LBL coated side with 5000× magnification (c) LBL coated side with 2500× magnification and (d) LBL coated side with 5000× magnification.

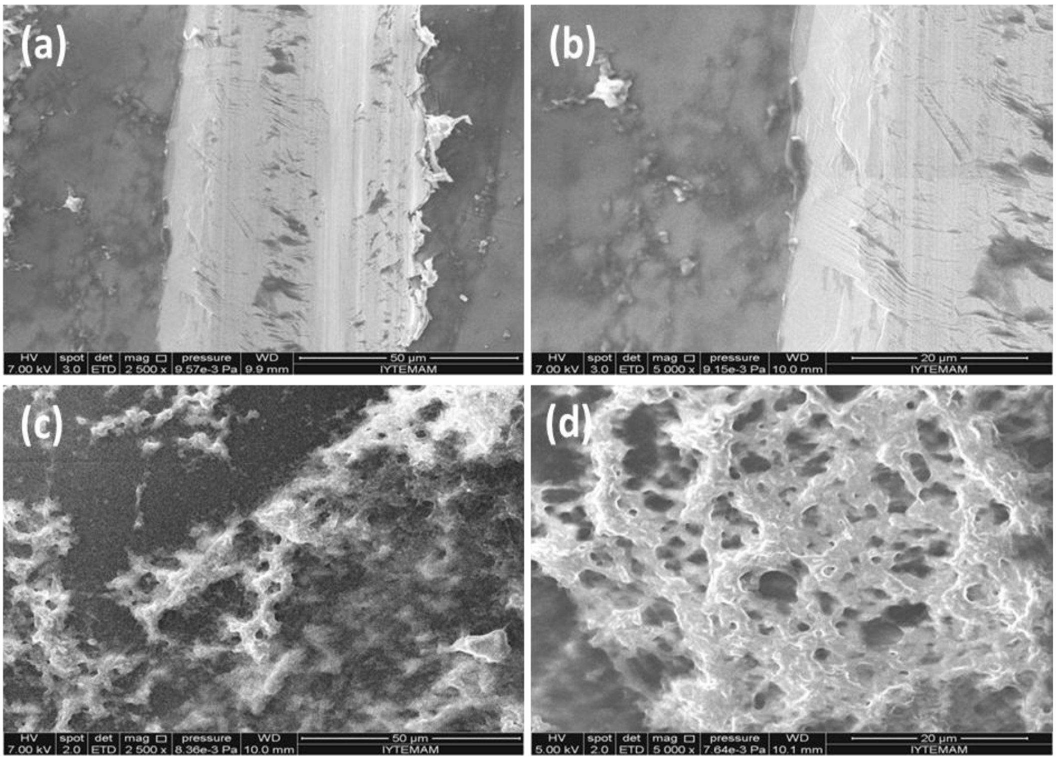

Figure 3.62 : SEM images of (SF/HA LBL)$_7$ on CoCrMo alloy at pH 3.0 (a) Scratched side with the bistoury and LBL coated side with 2500× magnification (b) Scratched side with the bistoury and LBL coated side with 5000× magnification (c) LBL coated side with 2500× magnification and (d) LBL coated side with 5000× magnification.

3.3.4.2 SEM results of (SF/HA LBL) films at pH 3.5

Figure 3.63, 3.64 and 3.65 shows SEM images of (SF/HA LBL)$_3$, (SF/HA LBL)$_5$ and (SF/HA LBL)$_7$ films on CoCrMo alloys at pH 3.5 (a) scratched side with the bistoury and LBL coated side with 2500× magnification, (b) scratched side with the bistoury and LBL coated side with 5000× magnification, (c) LBL coated side with 2500× magnification and (d) LBL coated side with 5000× magnification, respectively. Small particle precipitates are also seen on the surface of the all layered films. However, small surface cracks are visible on the surface of the five bilayer coated samples. In seven bilayer coated samples, small fibre formation is seen on the surface. The fibre concentration on the surface of the seven bilayer coated samples is less than that of seven bilayer coated samples at pH 3.5. This is much attributed to the isoelectric point of silk fibroin. In this case, negatively and positively charged ions behave as a multicharged pairs. As a result, this pairs lessens the fibre formation and the surface of the films becomes more uniform.

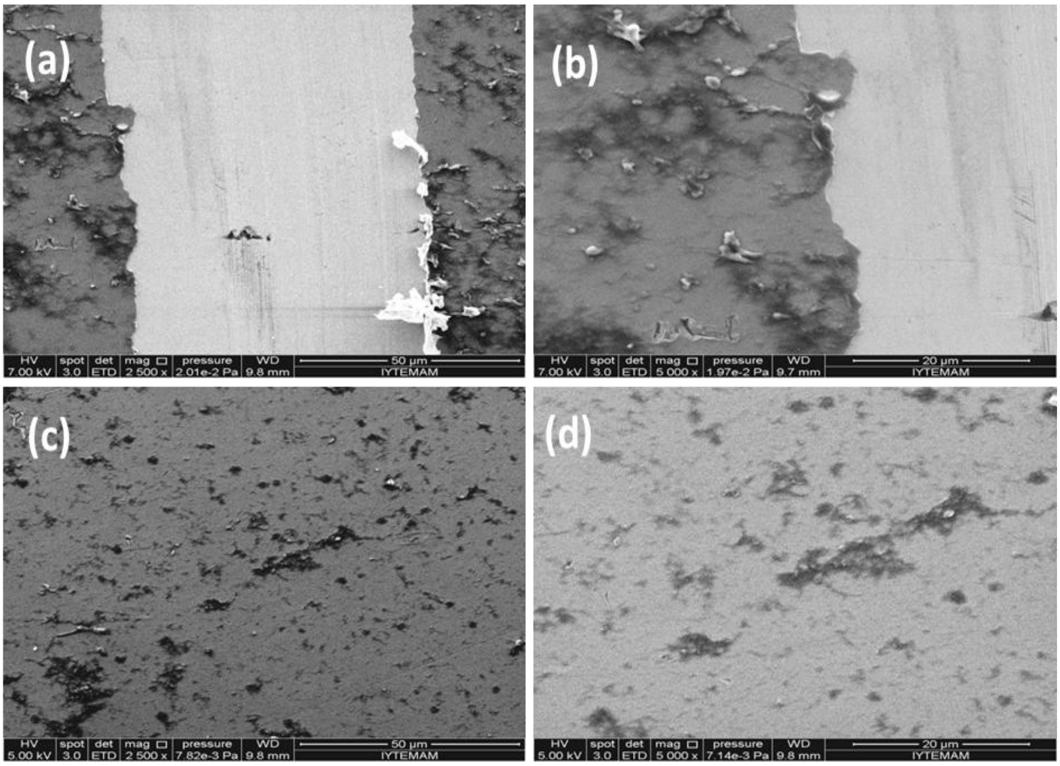

Figure 3.63 : SEM images of (SF/HA LBL)$_3$ on CoCrMo alloy at pH 3.5 (a) Scratched side with the bistoury and LBL coated side with 2500× magnification (b) Scratched side with the bistoury and LBL coated side with 5000× magnification (c) LBL coated side with 2500× magnification and (d) LBL coated side with 5000× magnification.

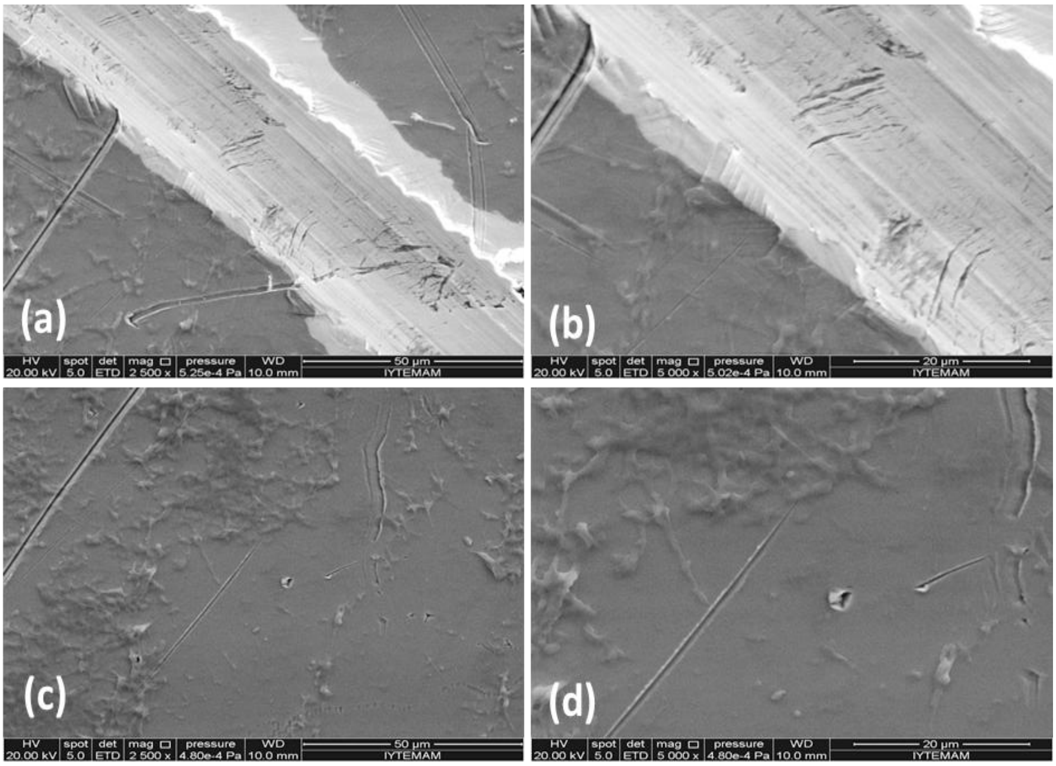

Figure 3.64 : SEM images of (SF/HA LBL)$_5$ on CoCrMo alloy at pH 3.5 (a) Scratched side with the bistoury and LBL coated side with 2500× magnification (b) Scratched side with the bistoury and LBL coated side with 5000× magnification (c) LBL coated side with 2500× magnification and (d) LBL coated side with 5000× magnification.

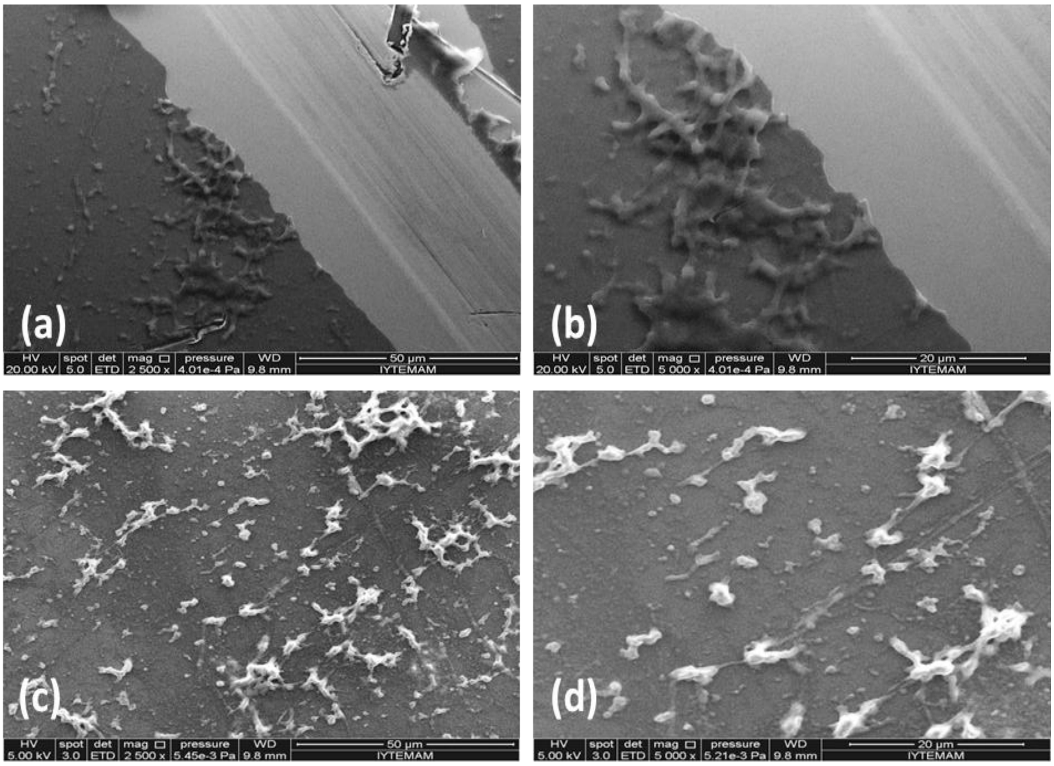

Figure 3.65 : SEM images of (SF/HA LBL)$_7$ on CoCrMo alloy at pH 3.5 (a) Scratched side with the bistoury and LBL coated side with 2500× magnification (b) Scratched side with the bistoury and LBL coated side with 5000× magnification (c) LBL coated side with 2500× magnification and (d) LBL coated side with 5000× magnification.

3.3.4.3 SEM results of (SF/HA LBL) films at pH 5.5

Figure 3.66, 3.67 and 3.68 shows SEM images of (SF/HA LBL)$_3$, (SF/HA LBL)$_5$ and (SF/HA LBL)$_7$ films on CoCrMo alloys at pH 5.5 (a) scratched side with the bistoury and LBL coated side with 2500× magnification, (b) scratched side with the bistoury and LBL coated side with 5000× magnification, (c) LBL coated side with 2500× magnification and (d) LBL coated side with 5000× magnification, respectively. The induced (SF/HA LBL) films were uniform in all coating layers. This was due to the working pH which was far away to the isoelectric point of SF. In this pH, SF and HA both were negatively charged and the fibres of SF were moved to the everywhere freely. As a result, the formed film was free of fibre.

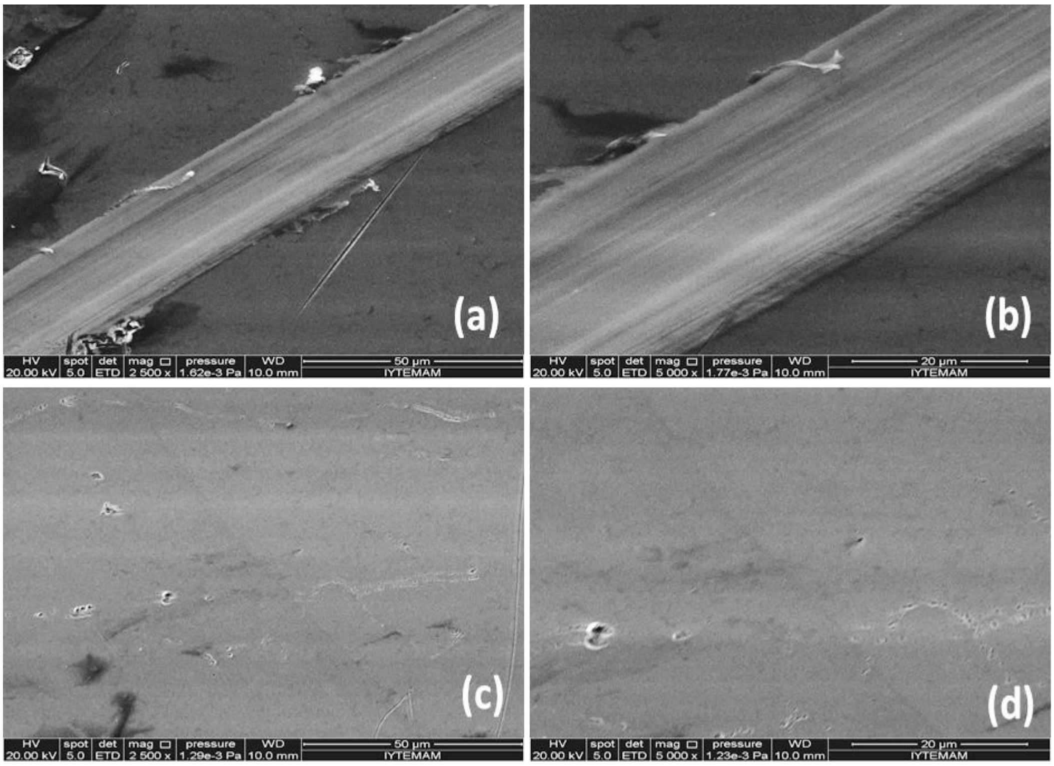

Figure 3.66 : SEM images of (SF/HA LBL)$_3$ on CoCrMo alloy at pH 5.5 (a) Scratched side with the bistoury and LBL coated side with 2500× magnification (b) Scratched side with the bistoury and LBL coated side with 5000× magnification (c) LBL coated side with 2500× magnification and (d) LBL coated side with 5000× magnification.

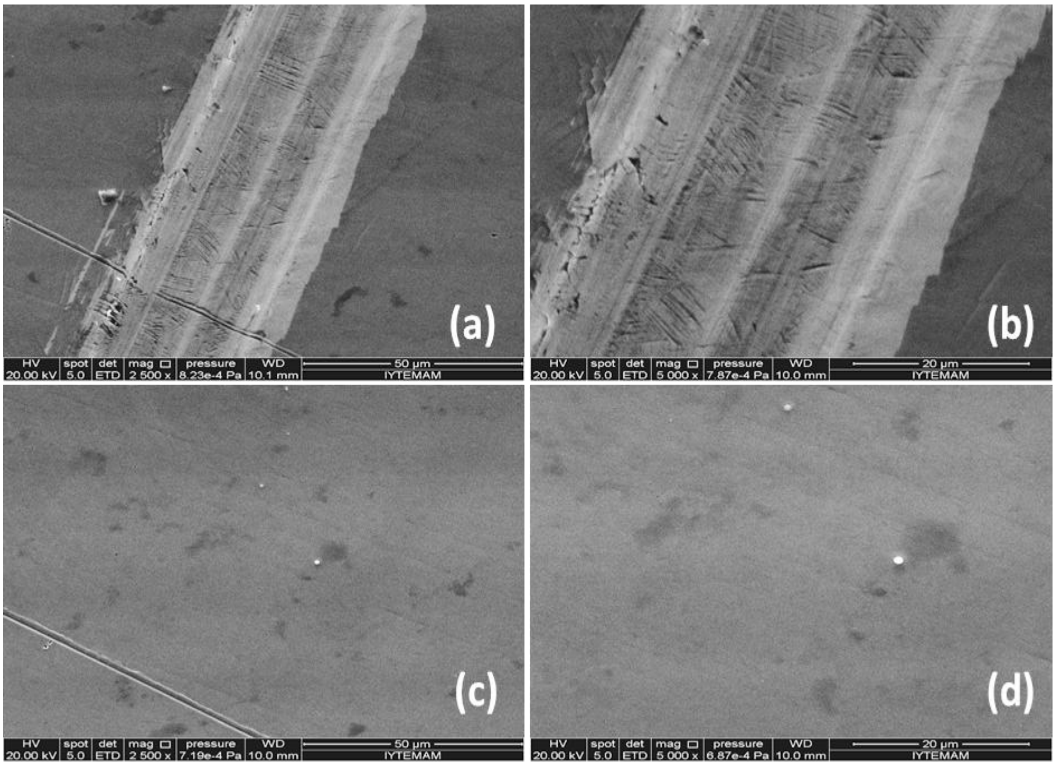

Figure 3.67 : SEM images of (SF/HA LBL)$_5$ on CoCrMo alloy at pH 5.5 (a) Scratched side with the bistoury and LBL coated side with 2500× magnification (b) Scratched side with the bistoury and LBL coated side with 5000× magnification (c) LBL coated side with 2500× magnification and (d) LBL coated side with 5000× magnification.

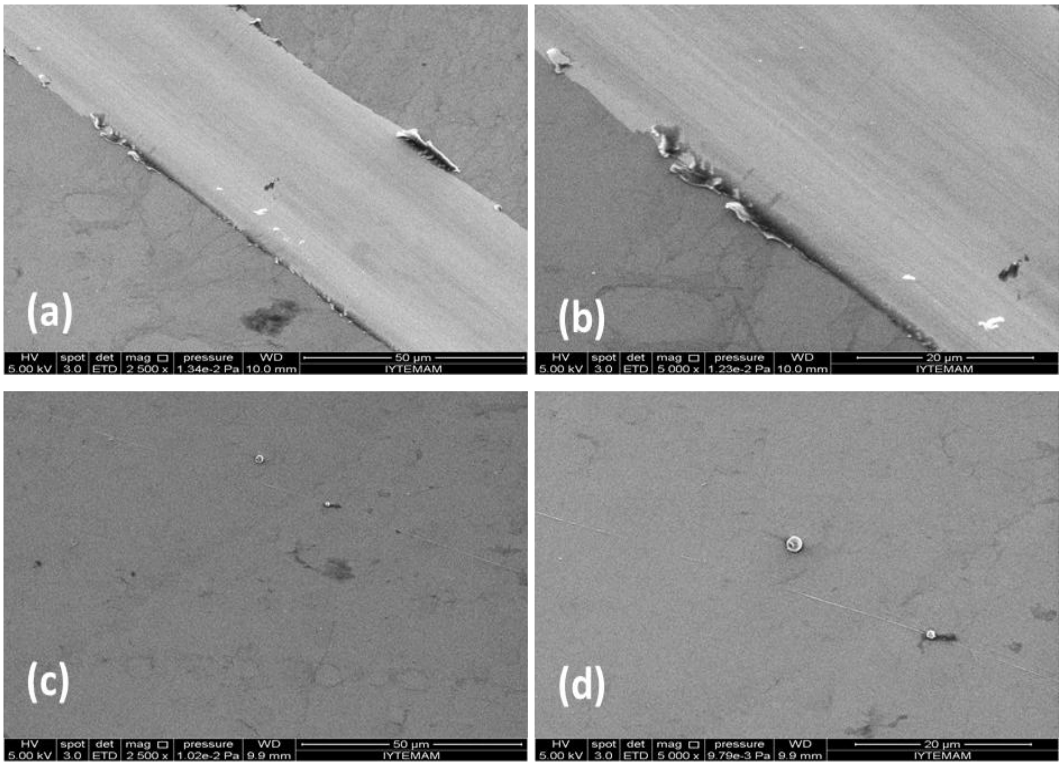

Figure 3.68 : SEM images of (SF/HA LBL)$_7$ on CoCrMo alloy at pH 5.5 (a) Scratched side with the bistoury and LBL coated side with 2500× magnification (b) Scratched side with the bistoury and LBL coated side with 5000× magnification (c) LBL coated side with 2500× magnification and (d) LBL coated side with 5000× magnification.

3.3.5 SEM results of levofloxacin loaded SF/HA complex and LBL films on CoCrMo alloys

Figure 3.69 shows SEM images of (SF/HA complex + Levofloxacin)$_{14}$ film on CoCrMo alloy at pH 3.5 (a) 2500× magnification, (b) 5000× magnification and Figure 3.70 shows SEM images of (SF/HA LBL + Levofloxacin)$_7$ film on CoCrMo alloy at pH 3.5 (a) 2500× magnification, (b) 5000× magnification.

As is seen in these images, surfaces of the fourteen layer of levofloxacin loaded complex and LBL samples became smoother and more uniform texture compared to the surfaces of the without levofloxacin loaded fourteen layer of complex and LBL coatings. SEM images clearly indicated that levofloxacin spreaded to almost all part of the surfaces on CoCrMo alloys at pH 3.5 for both coatings. Colloidal particles were still observed due to the working pH was close to the isoelectric point of fibroin (IEP=3.9). However, the number of the colloidal particles on CoCrMo alloys for both antibiotic loaded samples was less in comparison to the without levofloxacin loaded samples at pH 3.5.

However, the number of agglomerated particles of (SF/HA complex + Levofloxacin)$_{14}$ film was observed lower than the (SF/HA LBL + Levofloxacin)$_7$ film in SEM images. This may be caused the series of the antibiotic loading to the films on CoCrMo alloys. For the (SF/HA complex + Levofloxacin)$_{14}$ film, levofloxacin was loaded to each layer of the film. On the other hand, levofloxacin was loaded to SF only at 1., 7. and 13. layers into the (SF/HA LBL + Levofloxacin)$_7$ film on CoCrMo alloy. This may be effect the number of the colloidal particles on the surface.

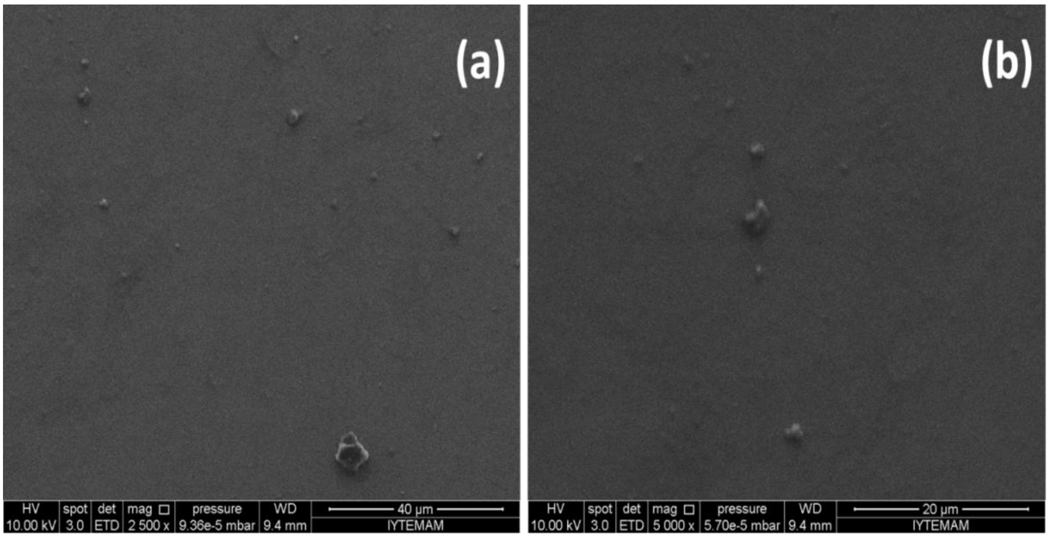

Figure 3.69 : SEM images of (SF/HA complex + Levofloxacin)$_{14}$ on CoCrMo alloy at pH 3.5 (a) 2500× magnification (b) 5000× magnification.

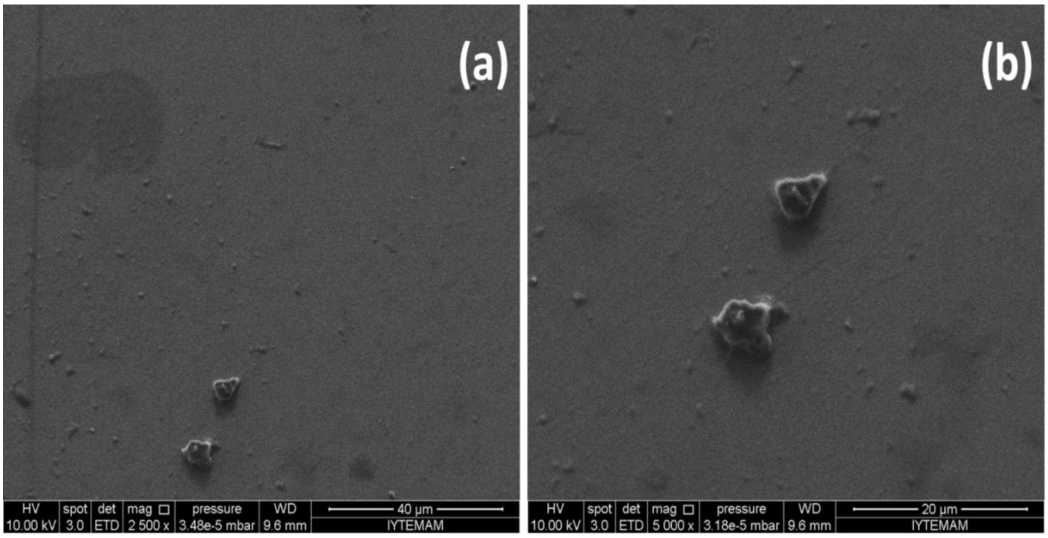

Figure 3.70 : SEM images of (SF/HA LBL + Levofloxacin)$_7$ on CoCrMo alloy at pH 3.5 (a) 2500× magnification (b) 5000× magnification.

3.4 AFM Results

Atomic Force Microscopy (AFM) average surface roughness (Ra) values of as received CoCrMo alloy, (SF/HA complex) and (SF/HA LBL) films on CoCrMo alloys at pH 3.5 tabulated in Table 3.3. Included in the same table is the result of induced film thickness and root mean square (Rq) values. The AFM scanning was conducted in 10x10 μm and 5x5 μm areas. Working pH was 3.50 for all (SF/HA complex) films on CoCrMo alloys and (SF/HA LBL) films on CoCrMo alloys. The surface scratches were avoided in scanning to remove the higher roughness values.

Ra and Rq values were measured for as received CoCrMo alloy in both areas and found to be 0.95 nm and 1.3 nm, respectively. The Ra and Rq parameters are measures with an average deviation from a reference line or plane. As is tabulated in Table 3.3, the AFM surface roughness values of (SF/HA complex) film coated specimens are higher than those of as received specimens. Complex film coatings increase the surface roughness values at least 5 times. Similarly, the surface roughness values of (SF/HA LBL) film coatings are in the range of 10.9 to 73.8 nm. As the number of coating layer increase, the surface roughness values increase. As is tabulated in Table 3.3, the AFM surface roughness values of (SF/HA LBL) film coated specimens are higher than those of as received specimens. Complex film coatings increase the surface roughness values at least 10 times. In addition, the increase of surface roughness values of complex films is higher than those of layer by layer coated films.

Table 3.3 : Rq, Ra and film thickness values of as received CoCrMo alloy and SF/HA complex and LBL films on CoCrMo alloys.

Sample	**Root Mean Square (Rq) (nm)**	**Average Roughness (Ra) (nm)**	**Film Thickness (nm)**
As received CoCrMo alloy	1,30	0.95	-
(SF/HA complex)$_6$ on CoCrMo alloy	8.70	5.80	90
(SF/HA complex)$_{10}$ on CoCrMo alloy	9.80	7.70	500
(SF/HA complex)$_{14}$ on CoCrMo alloy	36.5	28.9	600
(SF/HA LBL)$_3$ on CoCrMo alloy	15.1	10.9	140
(SF/HA LBL)$_5$ on CoCrMo alloy	42.4	32.4	450
(SF/HA LBL)$_7$ on CoCrMo alloy	102.3	73.8	640

Figure 3.71 (a-d) contains the 2D and 3D surface profiles of as received CoCrMo alloys. In Figure 3.71, small mountains and valleys are clearly seen and the sample surfaces contain some asperities which characterize the surface structures. Also, polishing scratches are visible.

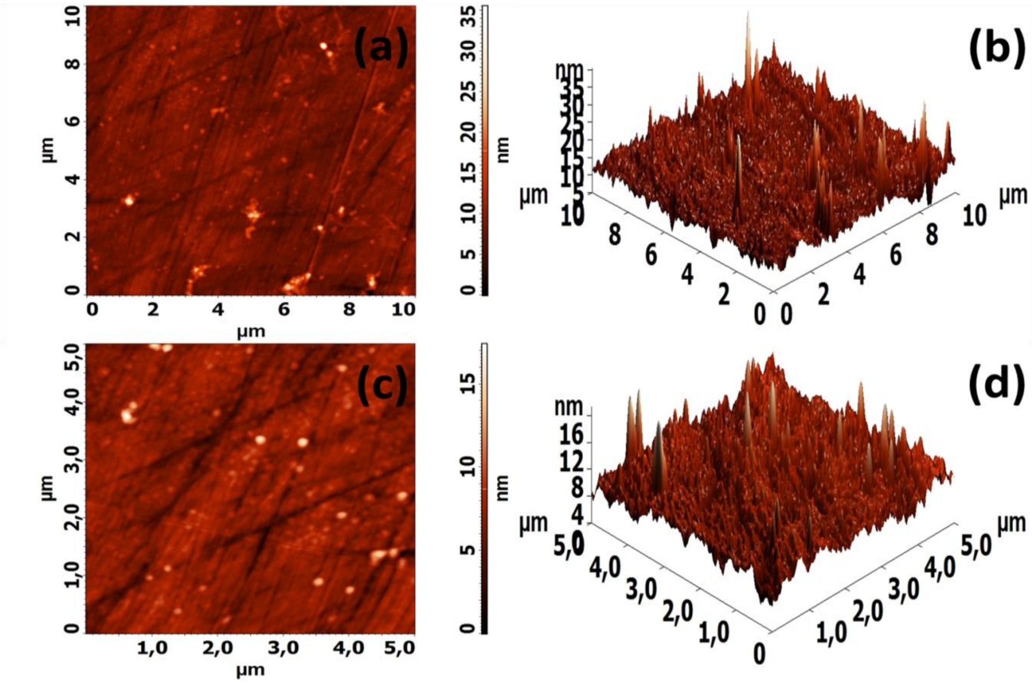

Figure 3.71 : AFM images of as received CoCrMo alloy (a) The 2D surface profile at 10x10 μm area (b) The 3D surface profile at 10x10 μm area (c) The 2D surface profile at 5x5 μm area (d) The 3D surface profile at 5x5 μm area.

The AFM images of surface flat sections taken from (SF/HA complex)$_6$ films on CoCrMo alloys are shown sequentially in Fig. 3.72 (a-d). Similarly, the scanned region was in 10x10 μm (Fig.3.72 (a-b)) and 5x5 (Fig. 3.72 (c-d)) μm. Some small hills and valleys are seen in Fig. 3.72 (b) and (d).

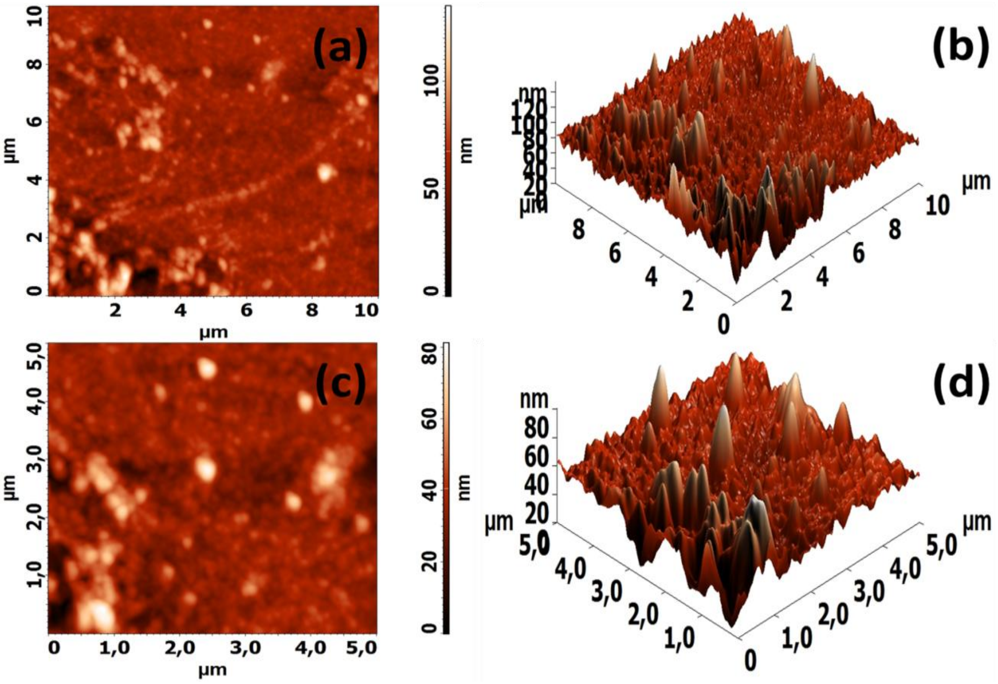

Figure 3.72 : AFM images of (SF/HA complex)$_6$ on CoCrMo alloy at pH 3.5 (a) The 2D surface profile at 10x10 µm area (b) The 3D surface profile at 10x10 µm area (c) The 2D surface profile at 5x5 µm area (d) The 3D surface profile at 5x5 µm area.

Figure 3.73 (a-d) shows the AFM images of (SF/HA complex)$_{10}$ films on CoCrMo alloys. These images clearly indicates that the surface is rougher than those of as received and six layered complex SF/HA coatings. This is associated with colloidal complex film structures which are close to the isoelectric point (IEP=3.9).

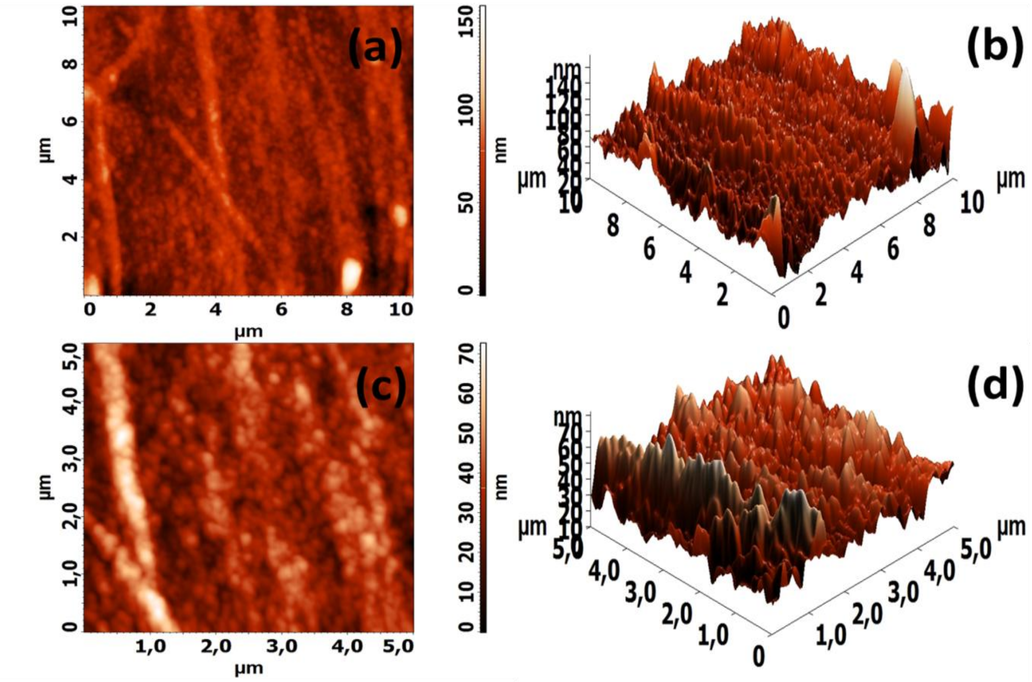

Figure 3.73 : AFM images of (SF/HA complex)$_{10}$ on CoCrMo alloy at pH 3.5 (a) The 2D surface profile at 10x10 µm area (b) The 3D surface profile at 10x10 µm area (c) The 2D surface profile at 5x5 µm area (d) The 3D surface profile at 5x5 µm area.

Figure 3.74 (a-d) shows the AFM images of fourteen layer (SF/HA complex)$_{14}$ films on CoCrMo alloys. As is seen in Fig. 3.74 (b) and (d), complex film structures are more clear than the other coatings. A rougher surface is seen and quite correlates the surface roughness values.

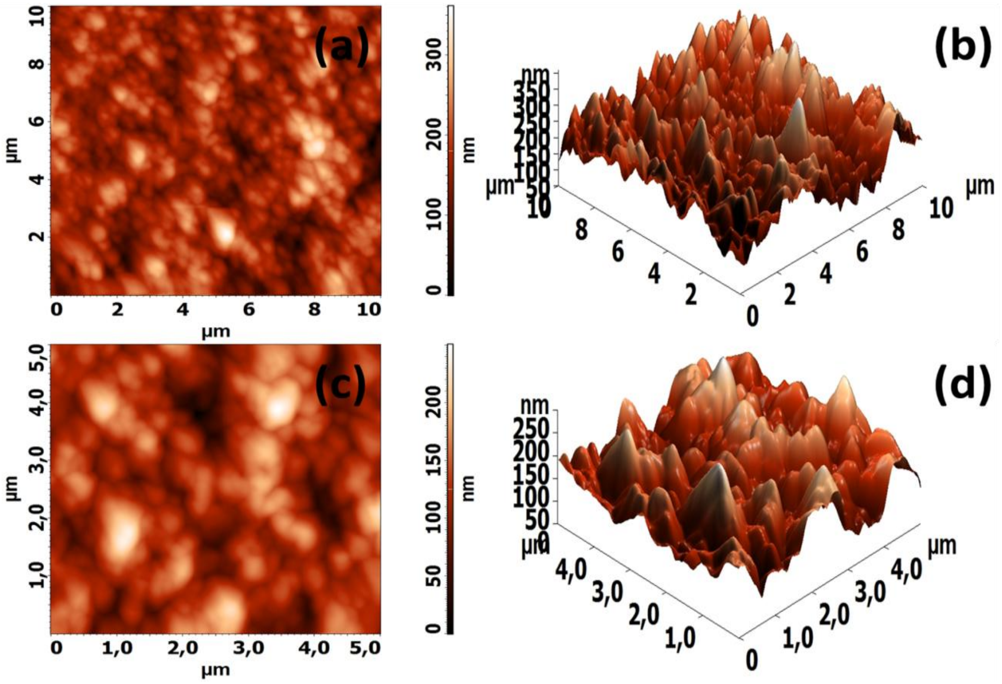

Figure 3.74 : AFM images of (SF/HA complex)$_{14}$ on CoCrMo alloy at pH 3.5 (a) The 2D surface profile at 10x10 µm area (b) The 3D surface profile at 10x10 µm area (c) The 2D surface profile at 5x5 µm area (d) The 3D surface profile at 5x5 µm area.

Figure 3.75 (a-d), 3.76 (a-d) and 3.77 (a-d) show the layer-by-layer SF/HA film coating of three, five and seven bilayer, respectively. As is seen for (SF/HA complex) films, colloidal particles are observed for all multilayer films on CoCrMo alloys due to working solution pH close to isoelectric point of SF (IEP=3.9). (SF/HA LBL)$_7$ film on CoCrMo alloy (Fig. 3.77 (b) and (d)) shows the highest hills as compared to the five and three bilayer film coatings.

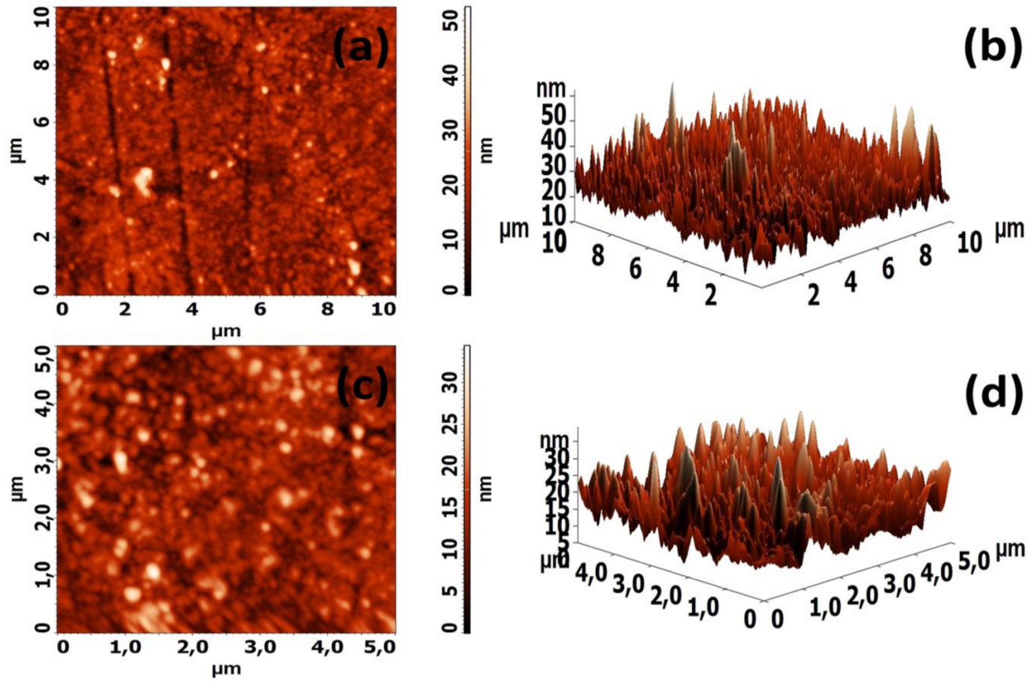

Figure 3.75 : AFM images of (SF/HA LBL)$_3$ on CoCrMo alloy at pH 3.5 (a) The 2D surface profile at 10x10 µm area (b) The 3D surface profile at 10x10 µm area (c) The 2D surface profile at 5x5 µm area (d) The 3D surface profile at 5x5 µm area.

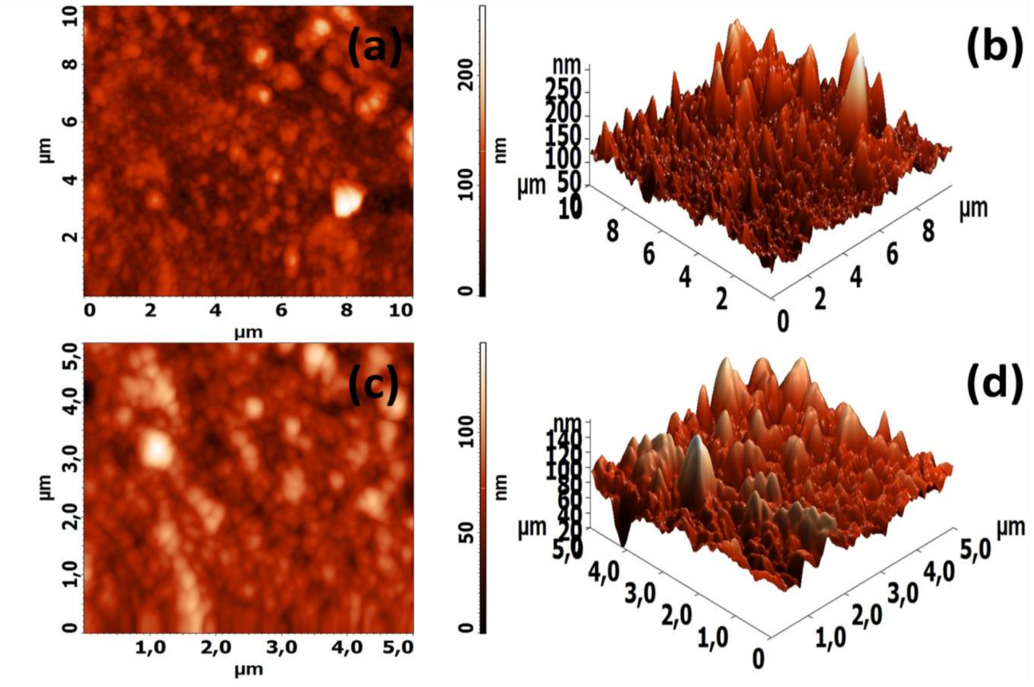

Figure 3.76 : AFM images of (SF/HA LBL)$_5$ on CoCrMo alloy at pH 3.5 (a) The 2D surface profile at 10x10 µm area (b) The 3D surface profile at 10x10 µm area (c) The 2D surface profile at 5x5 µm area (d) The 3D surface profile at 5x5 µm area.

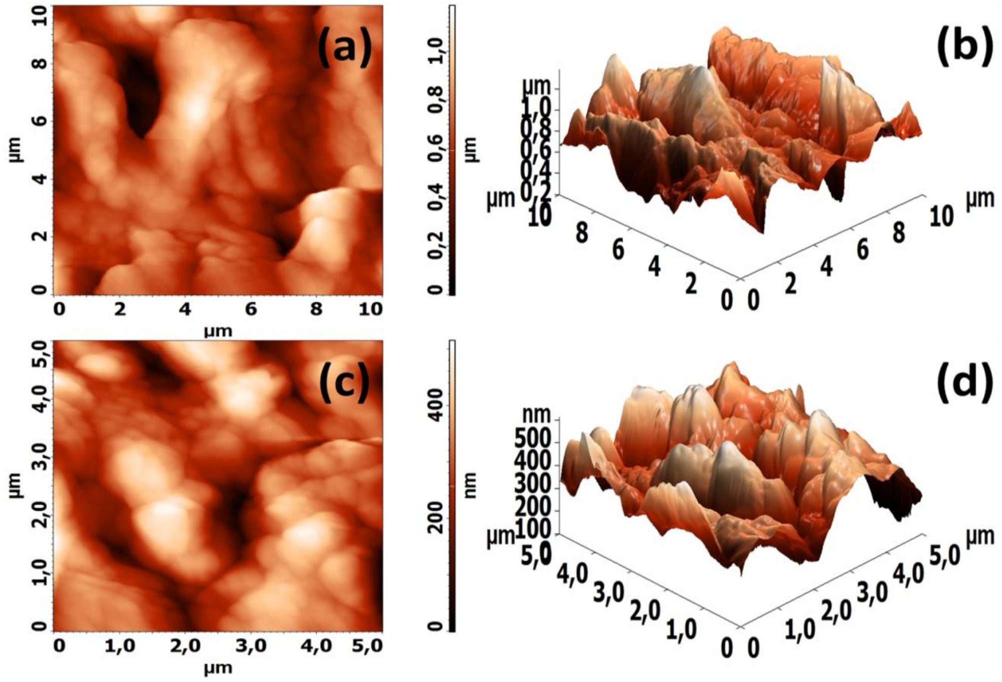

Figure 3.77 : AFM images of (SF/HA LBL)$_7$ on CoCrMo alloy at pH 3.5 (a) The 2D surface profile at 10x10 µm area (b) The 3D surface profile at 10x10 µm area (c) The 2D surface profile at 5x5 µm area (d) The 3D surface profile at 5x5 µm area.

In order to analyze the effect of number of layers on induced film roughness, film roughness of the investigated specimens are drawn as function of number of layers and shown in Figure 3.78. As seen in Figure 3.78, the film roughness values in both complex and layer-by-layer coated specimens increase with increasing number of layers. However, the surface roughness values of layer-by-layer induced films are higher than those of complex coated films. This also clearly indicates that the layer-by-layer coating produces rougher surfaces as compared to the complex coatings. This may be resulted in the formation of the fibre on the surface of layer-by-layer coated films. As already stated earlier, the SEM micrographs are clearly indicated the fibre formation on the surface of layer-by-layer coated specimens. This already quite correlates the SEM and AFM findings. The increase of the film thickness on both complex and layer-by-layer coated specimens is clearly seen in Figure 3.79. As is seen in Fig. 3.79, the film thickness of layer-by-layer coated specimens is higher than those of complex coated films on the investigated specimens. However, the film thickness of ten layered complex coating is higher than that of ten layered coated layer by layer films. The film thickness of layer-by-layer coated specimens increase as the number of layer increase. The increase of this film nearly linear as compared to the complex coatings. However, in complex coatings, the film thickness has a rapid rise followed by a slow increase and then it becomes nearly constant as is seen in Fig.3.79.

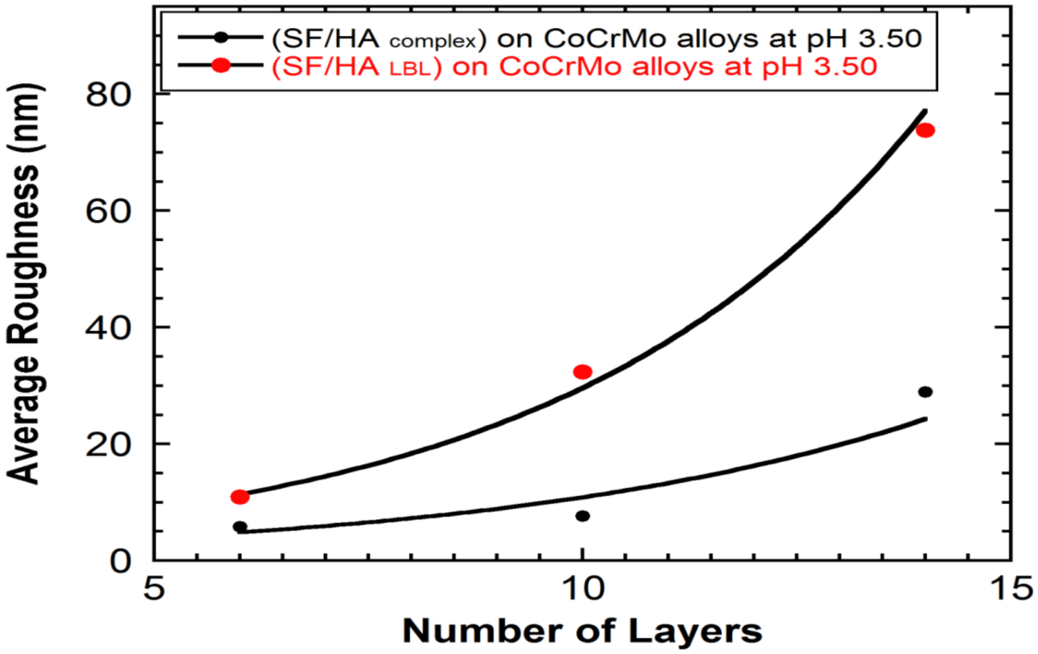

Figure 3.78 : AFM average roughness values as a function of the number of layers.

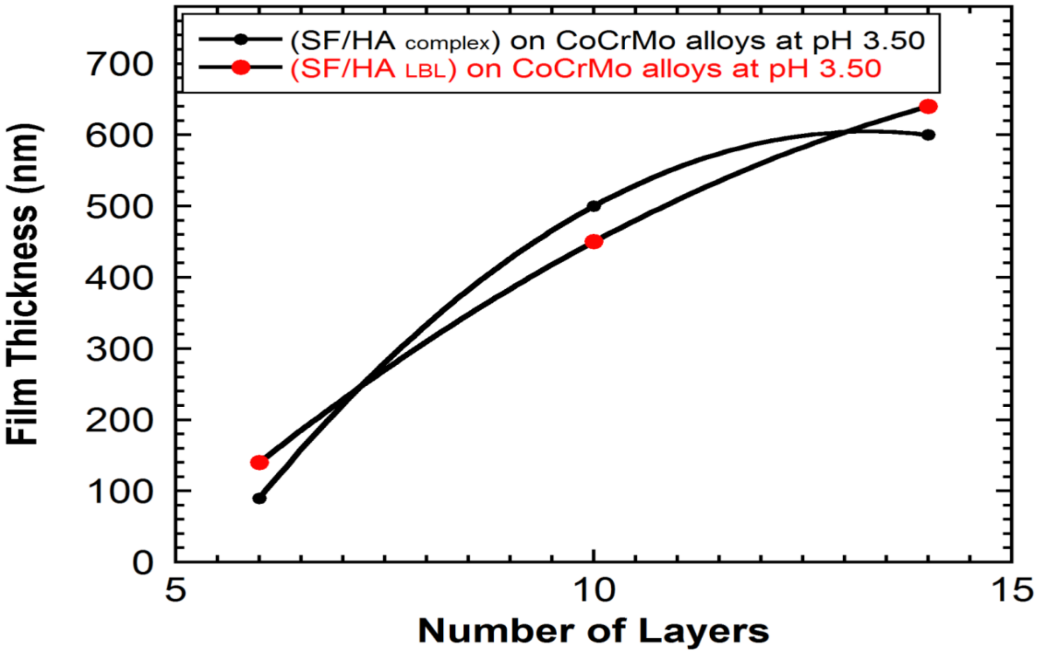

Figure 3.79 : AFM film thickness values as a function of the number of layers.

3.5 Antimicrobial Study Results

Antimicrobial properties of the films were investigated by colony counting method. Methicillin susceptible *Staphylococcus aureus* was used as the gram-positive bacteria, and levofloxacin was used as an antibiotic in this study. Figure 3.80 shows the graph of numbers of attached bacteria × 10^6 versus different sample types called control group, as received CoCrMo alloy, (SF/HA complex)$_{14}$ on CoCrMo alloy at pH 3.5, (SF/HA complex + Levofloxacin)$_{14}$ on CoCrMo alloy at pH 3.5, (SF/HA LBL)$_7$ on CoCrMo alloy at pH 3.5 and (SF/HA LBL + Levofloxacin)$_7$ on CoCrMo alloy at pH 3.5. In addition, these different sample types are enumerated as sample 1, 2, 3, 4, 5 and 6, respectively. After the antimicrobial study, the numbers of attached bacteria × 10^6 for sample 1, 2, 3, 4, 5 and 6 were 132.7, 100,7 82.7, 48, 92.7 and 66. The highest numbers of the bacteria were seen in the control group because control group was consisted of the only methicillin susceptible *S. aureus* bacteria. Number of the attached bacteria for the as received CoCrMo alloy was higher than complex coating, LBL coating and levofloxacin loaded complex and LBL coatings. Figure 3.80 shows that (SF/HA complex)$_{14}$ film on CoCrMo alloy at pH 3.5 decreased the bacterial attachment. (SF/HA LBL)$_7$ film at pH 3.5 also decreased the bacterial attachment. Levofloxacin loaded samples showed lower bacterial attachment as compared to the other samples. Figure 3.80 also demonstrated that the number of the attached bacteria of the levofloxacin loaded complex film was less than levofloxacin loaded LBL film on CoCrMo alloys at pH 3.5. This may be caused the series of the antibiotic loading into the films on CoCrMo alloys. For the (SF/HA complex + Levofloxacin)$_{14}$ film, levofloxacin was loaded to each layer of the film. On the other hand, levofloxacin was loaded to SF only at 1., 7. and 13. layers into the (SF/HA LBL + Levofloxacin)$_7$ film on CoCrMo alloy. This may be effect the numbers of the attached bacteria on the surfaces.

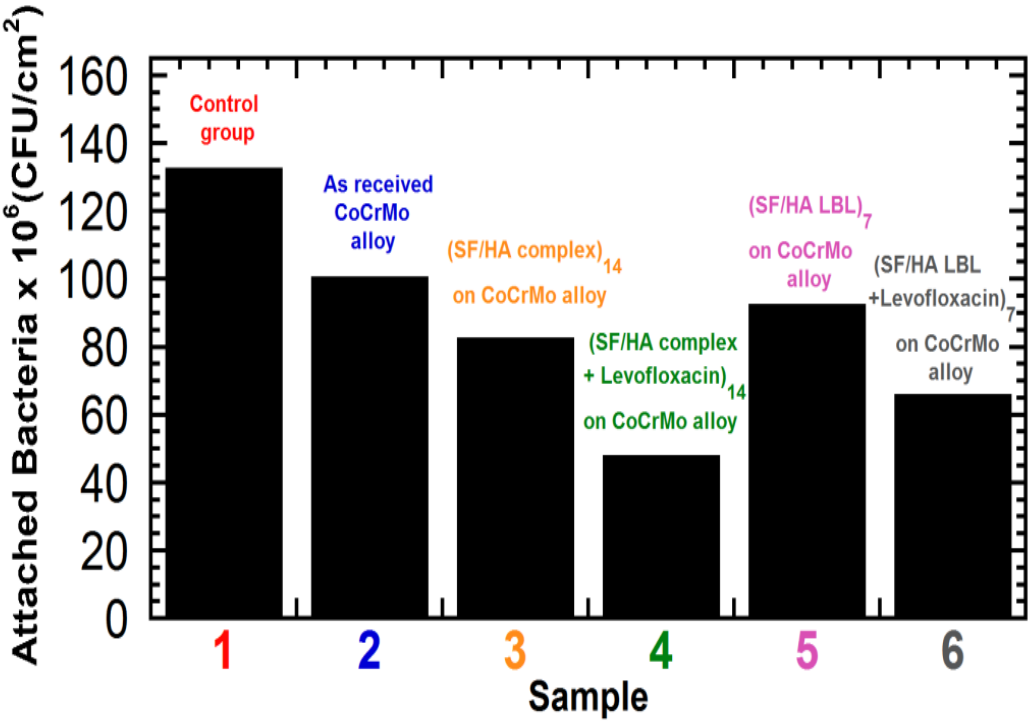

Figure 3.80 : The graph of numbers of attached bacteria versus different sample.

4. CONCLUSIONS

In this research, multiple layer SF, (SF/HA complex) and (SF/HA LBL) films were succesfully coated on CoCrMo alloys at three different pH values, 3.0, 3.5 and 5.5. SF and HA can be utilized to fabricate the complex films. SF is positively charged molecule under the isoelectric point of fibroin (IEP=3.9), whereas over the pH 2.5, HA is negatively charged. It was known that SF and HA complexes range is pH 2.5-3.5. The main reason to work with different pH values was to examine the influence of pH on the film characteristics.

Samples were characterized by ATR-FTIR, XRD, SEM and AFM. Fibroin conformations of consisted of six, ten and fourteen layers of SF, (SF/HA complex) and (SF/HA LBL) films at pH 3.0, 3.5 and 5.5 were confirmed by ATR-FTIR spectroscopy. All samples were washed with methanol:water mixture (volume ratio 70:30) to stimulate the conformation transition from silk I to silk II. The principal cause to create this transition, to make the films insoluble, to increase the mechanical characteristics and to improve the deposition rates on CoCrMo alloys. ATR-FTIR spectroscopy showed the characteristics IR absorption peaks for silk I and silk II conformations of the films on CoCrMo alloys. Surface structures of as received CoCrMo alloy, $(SF/HA\ complex)_{14}$ on CoCrMo alloy at pH 3.5, $(SF/HA\ LBL)_{7}$ on CoCrMo alloy at pH 3.5 were determined by XRD. The XRD spectra of induced films on CoCrMo showed that the films are amorphous structure due to the inorganic phase. SEM was utilized to show the surfaces of as received CoCrMo alloy and consisted of six, ten and fourteen multilayer structures of SF, (SF/HA complex) and (SF/HA LBL) films on CoCrMo alloys at pH 3.0, 3.5 and 5.5. SEM analysis indicated that the fibre formation occurs at near isoelectric point of SF and it is easy to induce a precipitates at that pH value. At pH 5.5 which is far away to the isoelectric point of SF, the induced films are at more uniform. Surface morphology of the as received CoCrMo alloy and consisted of six, ten and fourteen layer of (SF/HA complex) and (SF/HA LBL) films on CoCrMo alloys at pH 3.5 were shown by AFM. Colloidal particles were seen for all multilayer coatings because of the working solution pH close to IEP of fibroin. AFM measurements also showed that the surface roughness increased at 5 times as compared to the as received samples. The measured film thicknesses were in the range of 90 to 640 nm.

In the present study, a specific antibiotic called levofloxacin was loaded to the (SF/HA complex)$_{14}$ and (SF/HA LBL)$_7$ films on CoCrMo alloys at pH 3.5 to reduce the inflammation risk due to bacteria/microbe. The main motivation of us to start this research was to develop a new coating methodology for metal biomaterials to protect the infections and for this reason we wanted to solve the problem of infection of the bone (osteomyelitis). To enhance the film properties on CoCrMo alloys, levofloxacin was loaded to (SF/HA complex) at each layers. For (SF/HA LBL) coatings, levofloxacin was loaded to SF only at 1., 7. and 13. layers into the film on CoCrMo alloy. Antibiotic loading concentration was 3xMIC for complex and layer-by-layer coatings. Levofloxacin is known to effect gram positive bacteria so methicillin susceptible *Staphylococcus aureus* is an ideal bacteria for this study. ATR-FTIR spectroscopy showed the characteristic IR absorption bands for fourteen layer of SF/HA complex and SF/HA layer-by-layer films on CoCrMo alloys at pH 3.5. SEM images obviously demonstrated that the surfaces of the levofloxacin loaded complex and LBL films were smoother and more uniform texture in comparison to without levofloxacin loaded films on CoCrMo alloys at pH 3.5.

Antimicrobial properties of the films were investigated by colony counting method. In comparison with the control group, as received CoCrMo alloys, (SF/HA complex)$_{14}$ and (SF/HA LBL)$_7$ films on CoCrMo alloys at pH 3.5, levofloxacin loaded the fourteen layer of SF/HA complex and SF/HA layer-by-layer films on CoCrMo alloys at pH 3.5 showed lower bacterial attachment. The results clearly indicated that levofloxacin loading into the films is a powerful process to minimize the *S. aureus* attachment and at last, one step antibiotic loaded film coatings to reduce the infection risks are developed using complex coating methodology.

REFERENCES

Altman, G. H., F. Diaz, C. Jakuba, T. Calabro, R. L. Horan, J. S. Chen, H. Lu, J. Richmond and D. L. Kaplan (2003). "Silk-based biomaterials." Biomaterials 24(3): 401-416.

Altman, G. H., R. L. Horan, H. H. Lu, J. Moreau, M. I, J. C. Richmond and D. L. Kaplan (2002). "Silk matrix for tissue engineered anterior cruciate ligaments." Biomaterials 23(20): 4131-4141.

Asakura, T., A. Kuzuhara, R. Tabeta and H. Saito (1985). "Conformation Characterization of Bombyx-Mori Silk Fibroin in the Solid-State by High-Frequency C-13 Cross Polarization Magic Angle Spinning Nmr, X-Ray-Diffraction, and Infrared-Spectroscopy." Macromolecules 18(10): 1841-1845.

Aviva Shiedlin, R. B., William Christopher, Saman Arbabi, Laura Yang, Ronald V. Maier, Norman Wainwright, Alice Childs, Robert J. Miller (2004). "Evaluation of Hyaluronan from Different Sources: Streptococcus zooepidemicus, Rooster Comb, Bovine Vitreous, and Human Umbilical Cord." Biomacromolecules 5: 2122-2127.

Ayutsede, J., M. Gandhi, S. Sukigara, M. Micklus, H. E. Chen and F. Ko (2005). "Regeneration of Bombyx mori silk by electrospinning. Part 3: characterization of electrospun nonwoven mat." Polymer 46(5): 1625-1634.

Bailey, K. (2013). Potential Applications of Silk Fibroin as a Biomaterial. Master of Applied Science, University of Waterloo.

Bini, E., D. P. Knight and D. L. Kaplan (2004). "Mapping domain structures in silks from insects and spiders related to protein assembly." Journal of Molecular Biology 335(1): 27-40.

Boulder, U. o. C. from http://orgchem.colorado.edu/Spectroscopy/specttutor/irchart.pdf.

Bunning, T. J., H. Jiang, W. W. Adams, R. L. Crane, B. Farmer and D. Kaplan (1993). Applications of Silk. Silk Polymers

Materials Science and Biotechnology. **D. Kaplan, W. W. Adams, B. Farmer and C. Viney**. Charlottesville, VA, Oxford University Press. 544: 351-358.

Burgess, D. J. and S. Ponsart (1998). "beta-Glucuronidase activity following complex coacervation and spray drying microencapsulation." Journal of Microencapsulation 15(5): 569-579.

Cai, K., Y. Hu and K. D. Jandt (2007). "Surface engineering of titanium thin films with silk fibroin via layer-by-layer technique and its effects on osteoblast growth behavior." Journal of Biomedical Materials Research Part A 82A(4): 927-935.

Carole E. Schanté, G. Z., Corinne Herlin, Thierry F. Vandamme (2011). "Chemical Modifications of Hyaluronic Acid for the Synthesis of Derivatives for a Broad Range of Biomedical Applications." Carbohydrate Polymers 85(3): 469-489.

Cebeci, F. C., Z. Z. Wu, L. Zhai, R. E. Cohen and M. F. Rubner (2006). "Nanoporosity-driven superhydrophilicity: A means to create multifunctional antifogging coatings." Langmuir 22(6): 2856-2862.

Chen, X., D. P. Knight and Z. Z. Shao (2009). "beta-turn formation during the conformation transition in silk fibroin." Soft Matter 5(14): 2777-2781.

Chen, X., Z. Z. Shao, D. P. Knight and F. Vollrath (2007). "Conformation transition kinetics of Bombyx mori silk protein." Proteins-Structure Function and Bioinformatics 68(1): 223-231.

Chen, X., Z. Z. Shao, N. S. Marinkovic, L. M. Miller, P. Zhou and M. R. Chance (2001). "Conformation transition kinetics of regenerated Bombyx mori silk fibroin membrane monitored by time-resolved FTIR spectroscopy." Biophysical Chemistry 89(1): 25-34.

Chua, P. H., K. G. Neoh, E. T. Kang and W. Wang (2008). "Surface functionalization of titanium with hyaluronic acid/chitosan polyelectrolyte multilayers and RGD for promoting osteoblast functions and inhibiting bacterial adhesion." Biomaterials 29(10): 1412-1421.

Cilurzo, F., C. G. M. Gennari, F. Selmin, L. A. Marotta, P. Minghetti and L. Montanari (2011). "An investigation into silk fibroin conformation in composite materials intended for drug delivery." International Journal of Pharmaceutics 414(1-2): 218-224.

Çağlar, Ö. (2007). Structural Investigation and Wettability of PVD TiN Coated CoCrMo Orthopedic Alloy MASTER OF SCIENCE, İzmir Institute of Technology.

Dai, L. X., J. Li and E. Yamada (2002). "Effect of glycerin on structure transition of PVA/SF blends." Journal of Applied Polymer Science 86(9): 2342-2347.

Dal Pra, I., G. Freddi, J. Minic, A. Chiarini and U. Armato (2005). "De novo engineering of reticular connective tissue in vivo by silk fibroin nonwoven materials." Biomaterials 26(14): 1987-1999.

de Kruif, C. G., F. Weinbreck and R. de Vries (2004). "Complex coacervation of proteins and anionic polysaccharides." Current Opinion in Colloid & Interface Science 9(5): 340-349.

Decher, G. (1997). "Fuzzy nanoassemblies: Toward layered polymeric multicomposites." Science 277(5330): 1232-1237.

Decher, G. (2003). Multilayer Thin Films: Sequential Assembly of Nanocomposite Materials, Wiley-VCH.

Decher, G., J. D. Hong and J. Schmitt (1992). "Buildup of Ultrathin Multilayer Films by a Self-Assembly Process .3. Consecutively Alternating Adsorption of Anionic and Cationic Polyelectrolytes on Charged Surfaces." Thin Solid Films 210(1-2): 831-835.

Dicko, C., J. M. Kenney, D. Knight and F. Vollrath (2004). "Transition to a beta-sheet-rich structure in spidroin in vitro: The effects of pH and cations." Biochemistry 43(44): 14080-14087.

DoITPoMS. Retrieved October, 2013, from http://www.doitpoms.ac.uk/tlplib/bones/printall.php.

Duisabeau, L., P. Combrade and B. Forest (2004). "Environmental effect on fretting of metallic materials for orthopaedic implants." Wear 256(7-8): 805-816.

Freddi, G., M. Tsukada and S. Beretta (1999). "Structure and physical properties of silk fibroin polyacrylamide blend films." Journal of Applied Polymer Science 71(10): 1563-1571.

Garcia-Fuentes, M., E. Giger, L. Meinel and H. P. Merkle (2008). "The effect of hyaluronic acid on silk fibroin conformation." Biomaterials 29(6): 633-642.

Ghosh, S., I. Kobal, D. Zanette and W. F. Reed (1993). "Conformational Contraction and Hydrolysis of Hyaluronate in Sodium-Hydroxide Solutions." Macromolecules 26(17): 4685-4693.

Gibbs, D. A., E. W. Merrille, K. A. Smith and E. A. Balazs (1968). "Rheology of Hyaluronic Acid." Biopolymers 6: 777-791.

Grigorij Kogan, L. S., Robert Stern, Peter Gemeiner (2007). "Hyaluronic Acid: A Natural Biopolymer with a Broad Range of Biomedical and Industrial Applications." Biotechnol Lett 29: 17-25.

Hanawa, T., K. Nakazawa, K. Kano, S. Hiromoto, Y. Suzuki and A. Chiba (2005). "Friction-wear properties of nitrogen-ion-implanted nickel-free Co-Cr-Mo alloy." Materials Transactions 46(7): 1593-1596.

Hardingham, T. (2004). Solution Properties of Hyaluronan. Chemistry and Biology of Hyaluronan. H. G. Garg and C. A. Hales, Elsevier Science: 1-19.

Hofmann, S., C. T. W. P. Foo, F. Rossetti, M. Textor, G. Vunjak-Novakovic, D. L. Kaplan, H. P. Merkle and L. Meinel (2006). "Silk fibroin as an organic polymer for controlled drug delivery." Journal of Controlled Release 111(1-2): 219-227.

Holmes, T. C. (2002). "Novel peptide-based biomaterial scaffolds for tissue engineering." Trends in Biotechnology 20(1): 16-21.

Hu, K., Q. Lv, F. Z. Cui, Q. L. Feng, X. D. Kong, H. L. Wang, L. Y. Huang and T. Li (2006). "Biocompatible fibroin blended films with recombinant human-like collagen for hepatic tissue engineering." Journal of Bioactive and Compatible Polymers 21(1): 23-37.

Iler, R. K. (1966). "Multilayers of colloidal particles." J. Colloid Interface Sci. 21: 569-594.

Ishida, M., T. Asakura, M. Yokoi and H. Saito (1990). "Solvent-Induced and Mechanical-Treatment-Induced Conformational Transition of Silk Fibroins Studied by High-Resolution Solid-State C-13 Nmr-Spectroscopy." Macromolecules 23(1): 88-94.

Jiang, Y. and Q. R. Huang (2004). "Microencapsulation and controlled-release of food enzyme using protein-polysaccharide coacervates." Abstracts of Papers of the American Chemical Society 228: U396-U397.

Jin, H. J. and D. L. Kaplan (2003). "Mechanism of silk processing in insects and spiders." Nature 424(6952): 1057-1061.

Jin, H. J., J. Park, V. Karageorgiou, U. J. Kim, R. Valluzzi and D. L. Kaplan (2005). "Water-stable silk films with reduced beta-sheet content." Advanced Functional Materials 15(8): 1241-1247.

Johnston, A. P. R., C. Cortez, A. S. Angelatos and F. Caruso (2006). "Layer-by-layer engineered capsules and their applications." Current Opinion in Colloid & Interface Science 11(4): 203-209.

Jones, O. G., U. Lesmes, P. Dubin and D. J. McClements (2010). "Effect of polysaccharide charge on formation and properties of biopolymer nanoparticles created by heat treatment of beta-lactoglobulin-pectin complexes." Food Hydrocolloids 24(4): 374-383.

Juhlin, L. (1997). "Hyaluronan in skin." Journal of Internal Medicine 242(1): 61-66.

Kaplan, D. L., C. M. Mello, S. Arcidiacono, S. Fossey, K. Senecal and W. Muller (1997). Silk Protein-Based Materials. Birkhauser. Boston, MA.

Katti, K. S. (2004). "Biomaterials in total joint replacement." Colloids and Surfaces B-Biointerfaces 39(3): 133-142.

Khademhosseini, A., K. Y. Suh, J. M. Yang, G. Eng, J. Yeh, S. Levenberg and R. Langer (2004). "Layer-by-layer deposition of hyaluronic acid and poly-L-lysine for patterned cell co-cultures." Biomaterials 25(17): 3583-3592.

Kim, U. J., J. Y. Park, C. M. Li, H. J. Jin, R. Valluzzi and D. L. Kaplan (2004). "Structure and properties of silk hydrogels." Biomacromolecules 5(3): 786-792.

Kino, R., T. Ikorna, S. Yunoki, N. Nagai, J. Tanaka, T. Asakura and M. Munekata (2007). "Preparation and characterization of multilayered hydroxyapatite/silk fibroin film." Journal of Bioscience and Bioengineering 103(6): 514-520.

Kotov, N. A. (1999). "Layer-by-layer self-assembly: The contribution of hydrophobic interactions." Nanostructured Materials 12(5-8): 789-796.

Kozlovskaya, V., J. Baggett, B. Godin, X. W. Liu and E. Kharlampieva (2012). "Hydrogen-Bonded Multilayers of Silk Fibroin: From Coatings to Cell-Mimicking Shaped Microcontainers." Acs Macro Letters 1(3): 384-387.

Lapcik, L., L. Lapcik, S. De Smedt, J. Demeester and P. Chabrecek (1998). "Hyaluronan: Preparation, structure, properties, and applications." Chemical Reviews 98(8): 2663-2684.

Laurent, T. C. (1998). The Chemistry, Biology and Medical Applications of Hyaluronan and Its Derivatives, Portland Press.

Laurent, T. C. and J. Gergely (1955). "Light Scattering Studies on Hyaluronic Acid." Journal of Biological Chemistry 212(1): 325-329.

Lee, D., R. E. Cohen and M. F. Rubner (2005). "Antibacterial properties of Ag nanoparticle loaded multilayers and formation of magnetically directed antibacterial microparticles." Langmuir 21(21): 9651-9659.

Leguen, E., A. Chassepot, G. Decher, P. Schaaf, J. C. Voegel and N. Jessel (2007). "Bioactive coatings based on polyelectrolyte multilayer architectures functionalized by embedded proteins, peptides or drugs." Biomolecular Engineering 24(1): 33-41.

Li, H., C. Chen, S. R. Zhang, J. Jiang, H. Y. Tao, J. L. Xu, J. G. Sun, W. Zhong and S. Y. Chen (2012). "The use of layer by layer self-assembled coatings of hyaluronic acid and cationized gelatin to improve the biocompatibility of poly(ethylene terephthalate) artificial ligaments for reconstruction of the anterior cruciate ligament." Acta Biomaterialia 8(11): 4007-4019.

Li, M. Z., S. Z. Lu, Z. Y. Wu, H. J. Yan, J. Y. Mo and L. H. Wang (2001). "Study on porous silk fibroin materials. I. Fine structure of freeze dried silk fibroin." Journal of Applied Polymer Science 79(12): 2185-2191.

Li, S. Q., Y. B. Tang, J. Q. Jia, M. Z. Jiang and H. Yan (2013). "Preparation and Properties of Multiple Layer Silk Fibroin Film Incorporating Sulfadiazine Sodium." Biotechnology, Chemical and Materials Engineering Ii, Pts 1 and 2 641-642: 910-914.

Li, X. J., Q. J. Luo, Y. Huang, X. D. Li, F. Zhang and S. F. Zhao (2012). "The responses of preosteoblasts to collagen/hyaluronic acid polyelectrolyte multilayer coating on titanium." Polymers for Advanced Technologies 23(4): 756-764.

Ling, S. J., Z. M. Qi, D. P. Knight, Z. Z. Shao and X. Chen (2011). "Synchrotron FTIR Microspectroscopy of Single Natural Silk Fibers." Biomacromolecules 12(9): 3344-3349.

Lojou, T. and P. Bianco (2004). "Buildup of polyelectrolyte-protein multilayer assemblies on gold electrodes. Role of the hydrophobic effect." Langmuir 20(3): 748-755.

Long Liu, Y. L., Jianghua Li, Guocheng Du, Jian Chen (2011). "Microbial Production of Hyaluronic Acid: Current State, Challenges, and Perspectives." Microbial Cell Factories 10(99).

Long, M. and H. J. Rack (1998). "Titanium alloys in total joint replacement - a materials science perspective." Biomaterials 19(18): 1621-1639.

Magnin, D., S. Dumitriu and E. Chornet (2003). "Immobilization of enzymes into a polyionic hydrogel: ChitoXan." Journal of Bioactive and Compatible Polymers 18(5): 355-373.

Magoshi, J., Y. Magoshi, B. M. A. and S. Nakamura (1996). Polymeric Materials Encyclopedia. CRC Press, New York.

Malay, O. (2005). Formation and Characterization of Silk Fibroin / Hyaluronic Acid Complexes and Their Use in Iontophoretic Drug Delivery MASTER OF SCIENCE, İzmir Institute of Technology.

Malay, O., O. Bayraktar and A. Batigun (2007). "Complex coacervation of silk fibroin and hyaluronic acid." International Journal of Biological Macromolecules 40(4): 387-393.

Mandal, B. B., J. K. Mann and S. C. Kundu (2009). "Silk fibroin/gelatin multilayered films as a model system for controlled drug release." European Journal of Pharmaceutical Sciences 37(2): 160-171.

Marsh, R. E., R. B. Corey and L. Pauling (1955). "An investigation of the structure of silk fibroin." Biochim Biophys Acta 16(1): 1-34.

Meyer, K. and J. W. Palmer (1934). "The Polysaccharide of the Vitreous Humor." J. Biol. Chem. 107: 629-634.

Milosev, I. and H. H. Strehblow (2003). "The composition of the surface passive film formed on CoCrMo alloy in simulated physiological solution." Electrochimica Acta 48(19): 2767-2774.

Min, B. M., L. Jeong, K. Y. Lee and W. H. Park (2006). "Regenerated silk fibroin nanofibers: Water vapor-induced structural changes and their effects on the behavior of normal human cells." Macromolecular Bioscience 6(4): 285-292.

Mondal, M., K. Trivedy and S. N. Kumar (2007). "The silk proteins, sericin and fibroin in silkworm, Bombyx mori Linn—a review." Caspian Journal of Environmental Sciences 5: 63-76.

Monti, P., G. Freddi, A. Bertoluzza, N. Kasai and M. Tsukada (1998). "Raman spectroscopic studies of silk fibroin from Bombyx mori." Journal of Raman Spectroscopy 29(4): 297-304.

Motta, A., L. Fambri and C. Migliaresi (2002). "Regenerated silk fibroin films: Thermal and dynamic mechanical analysis." Macromolecular Chemistry and Physics 203(10-11): 1658-1665.

Nam, J. and Y. H. Park (2001). "Morphology of regenerated silk fibroin: Effects of freezing temperature, alcohol addition, and molecular weight." Journal of Applied Polymer Science 81(12): 3008-3021.

Necas, J., L. Bartosikova, P. Brauner and J. Kolar (2008). "Hyaluronic acid (hyaluronan): a review." Veterinarni Medicina 53(8): 397-411.

Nevelos, J., J. C. Shelton and J. Fisher (2004). "Metallurgical considerations in the wear of metal-on-metal hip bearings." HIP Int 14(1): 1-10.

Nogueira, G. M., A. J. Swiston, M. M. Beppu and M. F. Rubner (2010). "Layer-by-Layer Deposited Chitosan/Silk Fibroin Thin Films with Anisotropic Nanofiber Alignment." Langmuir 26(11): 8953-8958.

Okazaki, Y. (2008). "Effects of heat treatment and hot forging on microstructure and mechanical properties of Co-Cr-Mo alloy for surgical implants." Materials Transactions 49(4): 817-823.

Park, S. J., K. Y. Lee, W. S. Ha and S. Y. Park (1999). "Structural changes and their effect on mechanical properties of silk fibroin/chitosan blends." Journal of Applied Polymer Science 74(11): 2571-2575.

Park, W. H., W. S. Ha, H. Ito, T. Miyamoto, H. Inagaki and Y. Noishiki (2001). "Relationships between antithrombogenicity and surface free energy of regenerated silk fibroin films." Fibers Polym. 2: 58-63.

Prehm, P. (2000). Hyaluronan. Polysaccharides I: Polysaccharides from Prokaryotes. E. J. Vandamme, S. De Baets and A. Steinbüchel, Wiley-VCH. 5: 379-404.

Sakabe, H., H. Ito, T. Miyamoto, Y. Noishiki and W. S. Ha (1989). "In vivo blood compatibility of regenerated silk fibroin." Sen-I Gakkaishi 45: 487-490.

Santin, M., A. Motta, G. Freddi and M. Cannas (1999). "In vitro evaluation of the inflammatory potential of the silk fibroin." Journal of Biomedical Materials Research 46(3): 382-389.

Sato, M. and T. J. Webster (2004). "Nanobiotechnology: implications for the future of nanotechnology in orthopedic applications." Expert Review of Medical Devices 1(1): 105-114.

Schmalzried, T. P. (2004). "How I choose a bearing surface for my patients." Journal of Arthroplasty 19(8): 50-53.

Schmalzried, T. P. (2005). "Metal-on-metal resurfacing arthroplasty - No way under the sun! In opposition." Journal of Arthroplasty 20(4): 70-71.

Schneider, A., C. Picart, B. Senger, P. Schaaf, J. C. Voegel and B. Frisch (2007). "Layer-by-layer films from hyaluronan and amine-modified hyaluronan." Langmuir 23(5): 2655-2662.

Schweizer, A., M. Luem, U. Riede, P. Lindenlaub and P. E. Ochsner (2005). "Five-year results of two cemented hip stem models each made of two different alloys." Archives of Orthopaedic and Trauma Surgery 125(2): 80-86.

Schweizer, A., U. Riede, T. B. Maurer and P. E. Ochsner (2003). "Ten-year follow-up of primary straight-stem prosthesis (MEM) made of titanium or cobalt chromium alloy." Archives of Orthopaedic and Trauma Surgery 123(7): 353-356.

Serianni, A. S. Retrieved September, 2013, from http://www.nd.edu/~aseriann/silk.gif.

Shchepelina, O., I. Drachuk, M. K. Gupta, J. Lin and V. V. Tsukruk (2011). "Silk-on-Silk Layer-by-Layer Microcapsules." Advanced Materials 23(40): 4655-+.

Silva, S. S., A. Motta, M. T. Rodrigues, A. F. M. Pinheiro, M. E. Gomes, J. F. Mano, R. L. Reis and C. Migliaresi (2008). "Novel Genipin-Cross-Linked Chitosan/Silk Fibroin Sponges for Cartilage Engineering Strategies." Biomacromolecules 9(10): 2764-2774.

Smith, R. P., A. L. Baltch, M. A. Franke, P. B. Michelsen and L. H. Bopp (2000). "Levofloxacin penetrates human monocytes and enhances intracellular killing of Staphylococcus aureus and Pseudomonas aeruginosa." Journal of Antimicrobial Chemotherapy 45(4): 483-488.

Sofia, S., M. B. McCarthy, G. Gronowicz and D. L. Kaplan (2001). "Functionalized silk-based biomaterials for bone formation." Journal of Biomedical Materials Research 54(1): 139-148.

Soltes, L. and R. Mendichi (2003). "Molecular characterization of two host-guest associating hyaluronan derivatives." Biomedical Chromatography 17(6): 376-384.

Soltes, L., R. Mendichi, G. Kogan, J. Schiller, M. Stankovska and J. Arnhold (2006). "Degradative action of reactive oxygen species on hyaluronan." Biomacromolecules 7(3): 659-668.

Su, B., M. Li, Z. Y. Shi and Q. H. Lu (2009). "From Superhydrophilic to Superhydrophobic: Controlling Wettability of Hydroxide Zinc Carbonate Film on Zinc Plates." Langmuir 25(6): 3640-3645.

Swiston, A. J., C. Cheng, S. H. Um, D. J. Irvine, R. E. Cohen and M. F. Rubner (2008). "Surface Functionalization of Living Cells with Multilayer Patches." Nano Letters 8(12): 4446-4453.

Thierry, B., F. M. Winnik, Y. Merhi and M. Tabrizian (2003). "Nanocoatings onto arteries via layer-by-layer deposition: Toward the in vivo repair of damaged blood vessels." Journal of the American Chemical Society 125(25): 7494-7495.

Tolstoguzov, V. (2003). "Some thermodynamic considerations in food formulation." Food Hydrocolloids 17(1): 1-23.

Turgeon, S. L., M. Beaulieu, C. Schmitt and C. Sanchez (2003). "Protein-polysaccharide interactions: phase-ordering kinetics, thermodynamic and structural aspects." Current Opinion in Colloid & Interface Science 8(4-5): 401-414.

Türkan, U. (2004). Biocompatibility and Microstructural Characterization of PVD Coated and Nitrogen Implanted Co-Cr Alloy. MASTER OF SCIENCE, İzmir Institute of Technology.

Valluzzi, R., S. P. Gido, W. Muller and D. L. Kaplan (1999). "Orientation of silk III at the air-water interface." International Journal of Biological Macromolecules 24(2-3): 237-242.

Vidal, G., T. Blanchi, A. J. Mieszawska, R. Calabrese, C. Rossi, P. Vigneron, J. L. Duval, D. L. Kaplan and C. Egles (2013). "Enhanced cellular adhesion on titanium by silk functionalized with titanium binding and RGD peptides." Acta Biomaterialia 9(1): 4935-4943.

Wang, H. F., W. J. Li, Y. H. Lu and Z. L. Wang (1998). "Studies on chitosan and poly(acrylic acid) interpolymer complex. I. Preparation, structure, pH-sensitivity, and salt sensitivity of complex-forming poly(acrylic acid): Chitosan semi-interpenetrating polymer network (vol 65, pg 1445, 1997)." Journal of Applied Polymer Science 69(8): 1679-1679.

Wang, X. Q., E. Wenk, A. Matsumoto, L. Meinel, C. M. Li and D. L. Kaplan (2007). "Silk microspheres for encapsulation and controlled release." Journal of Controlled Release 117(3): 360-370.

Wang, X. Y., X. Hu, A. Daley, O. Rabotyagova, P. Cebe and D. L. Kaplan (2007). "Nanolayer biomaterial coatings of silk fibroin for controlled release." Journal of Controlled Release 121(3): 190-199.

Wang, X. Y., H. J. Kim, P. Xu, A. Matsumoto and D. L. Kaplan (2005). "Biomaterial coatings by stepwise deposition of silk fibroin." Langmuir 21(24): 11335-11341.

Wang, Y. F., J. Y. Gao and P. L. Dubin (1996). "Protein separation via polyelectrolyte coacervation: Selectivity and efficiency." Biotechnology Progress 12(3): 356-362.

Wenk, E., H. P. Merkle and L. Meinel (2011). "Silk fibroin as a vehicle for drug delivery applications." Journal of Controlled Release 150(2): 128-141.

Wenk, E., A. J. Wandrey, H. P. Merkle and L. Meinel (2008). "Silk fibroin spheres as a platform for controlled drug delivery." Journal of Controlled Release 132(1): 26-34.

Wu, Z., D. Lee, M. F. Rubner and R. E. Cohen (2007). "Structural color in porous, superhydrophilic, and self-cleaning SiO2/TiO2 Bragg stacks." Small 3(8): 1445-1451.

Xiang, Y., S. F. Lu and S. P. Jiang (2012). "Layer-by-layer self-assembly in the development of electrochemical energy conversion and storage devices from fuel cells to supercapacitors." Chemical Society Reviews 41(21): 7291-7321.

Xie, F., H. H. Zhang, H. L. Shao and X. C. Hu (2006). "Effect of shearing on formation of silk fibers from regenerated Bombyx mori silk fibroin aqueous solution." International Journal of Biological Macromolecules 38(3-5): 284-288.

Yamada, H., Y. Tsuboi and A. Itaya (2003). "AFM Observations of Silk Fibroin on Mica Substrates: Morphologies Reflecting the Secondary Structures." Thin Solid Films 440: 208-216.

Yan, Y., A. Neville and D. Blowson (2007). "Biotribocorrosion of CoCrMo orthopaedic implant materials - Assessing the formation and effectof the biofilm." Tribology International 40(10-12): 1492-1499.

Zhai, L., M. C. Berg, F. C. Cebeci, Y. Kim, J. M. Milwid, M. F. Rubner and R. E. Cohen (2006). "Patterned superhydrophobic surfaces: Toward a synthetic mimic of the Namib Desert beetle." Nano Letters 6(6): 1213-1217.

Zhang, Q., S. Q. Yan and M. Z. Li (2009). "Silk Fibroin Based Porous Materials." Materials 2(4): 2276-2295.

Zong, X. H., P. Zhou, Z. Z. Shao, S. M. Chen, X. Chen, B. W. Hu, F. Deng and W. H. Yao (2004). "Effect of pH and copper(II) on the conformation transitions of silk fibroin based on EPR, NMR, and Raman spectroscopy." Biochemistry 43(38): 11932-11941.